



S U S H A N T   B H A L C H A N D R A   P A T E

---

**NUMERICAL-  
EXPERIMENTAL APPROACH  
TO CHARACTERIZING  
KINEMATIC AND ISOTROPIC  
HARDENING IN AISI 316  
AUSTENITIC STAINLESS  
STEEL UNDER LOW-CYCLE  
FATIGUE**

---

D O C T O R A L   D I S S E R T A T I O N

K a u n a s  
2 0 2 6

KAUNAS UNIVERSITY OF TECHNOLOGY

SUSHANT BHALCHANDRA PATE

NUMERICAL–EXPERIMENTAL APPROACH  
TO CHARACTERIZING KINEMATIC AND  
ISOTROPIC HARDENING IN AISI 316  
AUSTENITIC STAINLESS STEEL UNDER  
LOW-CYCLE FATIGUE

Doctoral dissertation  
Technological Sciences, Mechanical Engineering (T 009)

2026, Kaunas

This dissertation has been prepared at the Department of Mechanical Engineering of the Faculty of Mechanical Engineering and Design of Kaunas University of Technology in 2021-2025.

The doctoral right has been granted to Kaunas University of Technology together with Vytautas Magnus University.

**Research Supervisor:**

Prof. Dr. Gintautas DUNDULIS (Kaunas University of Technology, Technological Sciences, Mechanical Engineering, T 009).

**Edited by:** English language editor Dr. Brigita Pantelejeva (KTU Centre of Foreign Languages), Lithuanian language editor Virginija Stankevičienė (KTU Centre of Foreign Languages).

**Dissertation Defence Board of Mechanical Engineering Science Field:**

Prof. Dr. Giedrius JANUŠAS (Kaunas University of Technology, Technological Sciences, Mechanical Engineering, T 009) – **chairperson**;

Prof. Dr. Regita BENDIKIENĖ (Kaunas University of Technology, Technological Sciences, Mechanical Engineering, T 009);

Prof. Dr. Valdas EIDUKYNAS (Kaunas University of Technology, Technological Sciences, Mechanical Engineering, T 009);

Prof. Dr. Hab. Rimantas KAČIANAUSKAS (Vilnius Gediminas Technical University, Technological Sciences, Mechanical Engineering, T 009);

Senior Researcher Dr. Andrejs KOVALOVS (Riga Technical University, Latvia, Technological Sciences, Mechanical Engineering, T 009).

The dissertation defence will be held on 7 April 2026, at 10 a.m. at the Rectorate Hall of Kaunas University of Technology in the meeting of the Dissertation Defence Board of the Mechanical Engineering Science Field.

Address: K. Donelaičio 73-402, LT-44249 Kaunas, Lithuania.

Phone: +370 608 28 527; email [doktorantura@ktu.lt](mailto:doktorantura@ktu.lt).

The dissertation was sent out on 6 March 2026.

The dissertation is available on the website <http://ktu.edu>, at the Library of Kaunas University of Technology (Gedimino 50, Kaunas) and at the Library of Vytautas Magnus University (K. Donelaičio 52, Kaunas).

© S. B. Pate, 2026

KAUNO TECHNOLOGIJOS UNIVERSITETAS

SUSHANT BHALCHANDRA PATE

SKAITINĖ-EKSPERIMENTINĖ METODIKA  
AISI 316 AUSTENITINIO NERŪDIJANČIOJO  
PLIENO KINEMATINIO IR IZOTROPINIO  
KIETĖJIMO CHARAKTERIZAVIMUI

Daktaro disertacija  
Technologijos mokslai, mechanikos inžinerija (T 009)

Kaunas, 2026

Disertacija rengta 2021–2025 metais Kauno technologijos universiteto Mechanikos inžinerijos ir dizaino fakultete, Mechanikos inžinerijos katedroje.

Doktorantūros teisė Kauno technologijos universitetui suteikta kartu su Vytauto Didžiojo universitetu.

**Mokslinis vadovas:**

prof. dr. Gintautas DUNDULIS (Kauno technologijos universitetas, technologijos mokslai, mechanikos inžinerija, T009).

**Redagavo:** anglų kalbos redaktorė dr. Brigita Pantelejeva (KTU Užsienio kalbų centras), lietuvių kalbos redaktorė Virginija Stankevičienė (KTU Užsienio kalbų centras).

**Mechanikos inžinerijos mokslo krypties disertacijos gynimo taryba:**

prof. dr. Giedrius JANUŠAS (Kauno technologijos universitetas, technologijos mokslai, mechanikos inžinerija, T 009) – **pirmininkas**;

prof. dr. Regita BENDIKIENĖ (Kauno technologijos universitetas, technologijos mokslai, mechanikos inžinerija, T 009);

prof. dr. Valdas EIDUKYNAS (Kauno technologijos universitetas, technologijos mokslai, mechanikos inžinerija, T 009);

prof. habil. dr. Rimantas KAČIANAUSKAS (Vilniaus Gedimino technikos universitetas, technologijos mokslai, mechanikos inžinerija, T 009);

vyresn. m. d. dr. Andrejs KOVALOVŠ (Rygos technikos universitetas, Latvija, technologijos mokslai, mechanikos inžinerija, T 009).

Disertacija bus ginama viešame Mechanikos inžinerijos mokslo krypties disertacijos gynimo tarybos posėdyje 2026 m. balandžio 7 d. 10 val. Kauno technologijos universiteto Rektorato salėje.

Adresas: K. Donelaičio g. 73-402, LT-44249 Kaunas, Lietuva.

Tel. +370 608 28 527; el. paštas [doktorantura@ktu.lt](mailto:doktorantura@ktu.lt)

Disertacija išsiųsta 2026 m. kovo 06 d.

Su disertacija galima susipažinti interneto svetainėje <http://ktu.edu>, Kauno technologijos universiteto bibliotekoje (Gedimino g. 50, Kaunas) ir Vytauto Didžiojo universiteto bibliotekoje (K. Donelaičio g. 52, Kaunas).

© S. B. Pate, 2026

# CONTENT

<b>LIST OF TABLES</b> .....	7
<b>LIST OF FIGURES</b> .....	8
<b>LIST OF ABBREVIATIONS AND TERMS</b> .....	14
<b>INTRODUCTION</b> .....	15
<b>1.LITERATURE REVIEW</b> .....	20
1.1. High-Cycle Fatigue Failure .....	20
1.2. Low-Cycle Fatigue Failure.....	21
1.3. Austenitic Stainless Steel.....	21
1.4. Fatigue Loading.....	25
1.5. Fatigue Life .....	26
1.6. Fatigue Analysis .....	28
1.6.2. Experimental Method .....	29
a. Component Testing.....	29
b. Polished Bar Specimen Testing.....	29
1.6.3. Analytical Method .....	30
1.6.4. Numerical Method.....	31
1.7. Fatigue Failure.....	32
1.8. Previously Recorded Work on LCF .....	33
1.9. Chapter Conclusion .....	36
<b>2.EXPERIMENTAL METHODOLOGY</b> .....	38
2.1. Standards for Experimental Analysis .....	39
2.2. Austenitic Steel.....	39
2.3. Specimen Design.....	40
2.4. Experimental Setup .....	42
2.5. Chapter Conclusion .....	45
<b>3.NUMERICAL SIMULATION METHODOLOGY</b> .....	46
3.1. Finite Element Modelling.....	46
3.2. Specimen Loading .....	48
3.3. Material Model .....	50
3.4. Kinematic Hardening.....	52
3.5. Isotropic Hardening.....	57
3.6. Chapter Conclusion .....	63
<b>4.EXPERIMENTAL RESEARCH RESULTS</b> .....	64
4.1. Chapter Conclusion .....	72
<b>5. NUMERICAL SIMULATION RESEARCH RESULTS AND VALIDATION</b> .....	73
5.1. Chapter Conclusion .....	87
<b>CONCLUSIONS</b> .....	89
<b>PROPOSAL FOR FUTURE</b> .....	90

<b>SANTRAUKA.....</b>	<b>91</b>
<b>LIST OF REFERENCES.....</b>	<b>133</b>
<b>CURRICULUM VITAE AND DESCRIPTION OF CREATIVE ACTIVITIES (CV).....</b>	<b>144</b>
<b>LIST OF SCIENTIFIC PAPERS AND SCIENTIFIC CONFERENCES .....</b>	<b>146</b>
<b>ACKNOWLEDGEMENT .....</b>	<b>148</b>

## LIST OF TABLES

Table 1. Overview of stainless-steel types and their key characteristics [17] .....	22
Table 2. Comparison of AISI 304L and AISI 316L stainless steels and their relevance in power plant applications [17].....	23
Table 3. Chemical composition of AISI 304L and AISI 316L stainless steel (wt%) [103] .....	40
Table 4. Experiment matrix for non-notch specimens.....	43
Table 5. Experiment matrix for the notch specimen.....	44
Table 6. Mechanical properties of stainless steel [111-117] .....	50
Table 7. Initial yield stress estimated using the first experimental result cycle .....	51
Table 8. Parameters for the Chaboche model estimated for the Ansys model .....	53
Table 9. Parameters for the Armstrong-Frederick kinematic hardening model estimated for numerical simulation .....	55
Table 11. Non-notched specimen failure cycle for experimental test on AISI316L stainless steel .....	70
Table 12. Notched specimen failure cycle for experimental test on AISI316L stainless steel .....	71
Table 13. Time required for the computation for the first cycle.....	73
Table 14. Maximum deviation between simulation and experimental results for LCF tests .....	86

## LENTELIŲ SĄRAŠAS

15 lentelė. AISI 304L ir AISI 316L nerūdijančio plieno cheminė sudėtis ( wt %) [103] .....	100
16 lentelė . Eksperimentinio tyrimo matrica bandiniams be įpjovų .....	102
17 lentelė. Įpjovos bandinio eksperimento matrica .....	103
18 lentelė. Austenitinio nerūdijančio plieno mechaninės savybės .....	107
19 lentelė. Austenitinio nerūdijančio plieno takumo riba, nustatyta pagal eksperimentinių tyrimų pirmąjį ciklą .....	107
20 lentelė. AISI 304L nerūdijančio plieno <i>Chaboche</i> modelio parametrai ( <i>Ansys</i> modeliui).....	109
21 lentelė. AISI316L nerūdijančio plieno <i>Armstrongo-Fredericko</i> kinematinio kietėjimo modelio parametrai.....	110
22 lentelė. Kinematinio kietėjimo parametrai įvertinti naudojant 45–50 lygtis .....	111
23 lentelė. AISI316L nerūdijančio plieno neįpjautų bandinių ciklų skaičius, kuriems esant bandinys suiro .....	118
24 lentelė. AISI316L nerūdijančio plieno bandinių su įpjovomis ciklų skaičius, kuriems esant bandinys suiro.....	119
25 lentelė. Pirmojo ciklo skaičiavimams reikalingas laikas .....	121
26 lentelė. Mažo ciklo degradacijos modeliavimo rezultatų nuokrypis nuo eksperimentinių tyrimų rezultatų.....	128

## LIST OF FIGURES

Fig. 1. Typical design and materials in a) PWR, b) BWR [15].....	25
Fig. 2. Loading waveform for different loading ratio.....	26
Fig. 3. Representation of bilinear SN curve [21].....	28
Fig. 4. Solid specimen of AISI 304L tested under 0.3 and 0.6% strain amplitude...	41
Fig. 5. Solid specimen of AISI316L tested at 20 °C and 300 °C for 0.18 and 0.6% strain amplitude .....	41
Fig. 6. Solid specimen of AISI 316L for the LCF test in air at 20 °C and 300 °C for 0.5 and 1 % strain amplitude (specimen used in EDF laboratory test).....	41
Fig. 7. Hollow specimen of AISI 316L for 0.3% strain amplitude LCF test in a PWR environment at 300°C (specimen used in EDF laboratory test) .....	42
Fig. 8. Notched specimen of AISI 316L, notch radius 0.5 and 2 mm at 300°C for stress-controlled LCF test.....	42
Fig. 9. INSTRON ElectroPuls™ E10000.....	44
Fig. 10. Full specimen FE model with applied boundary conditions .....	46
Fig. 11. Applied boundary conditions to reduced FE model .....	47
Fig. 12. Meshed FE model for a hollow specimen .....	47
Fig. 13. Meshed FE model with applied boundary conditions for the notched specimen .....	48
Fig. 14. Relative strain applied for the FE model in the case of strain-controlled scheme .....	48
Fig. 15. Loading applied for the FE model for the notch specimen with $r=0.5\text{mm}$ .	49
Fig. 16. Loading applied for the FE model for the notch specimen with $r=2\text{mm}$ ....	49
Fig. 17. Determination of yield stress by parallel line to the elastic region of curve with 0.2% strain offset [118] .....	51
Fig. 18. Isotropic hardening curve estimated for 0.3% strain amplitude at 300 ° C of the AISI304L stainless steel model .....	58
Fig. 19. Isotropic hardening curve estimated for 0.6% strain amplitude at 300 ° C of the AISI 304L stainless steel model .....	58
Fig. 20. Isotropic hardening curve used in LS-Dyna, AISI 316L for 0.18% strain amplitude at 20°C model .....	59
Fig. 21. Isotropic hardening curve used in LS-Dyna, AISI 316L for 0.6% strain amplitude at 300°C model .....	60
Fig. 22. Isotropic hardening curve employed for the numerical simulation of the 0.5% strain amplitude at 20 ° C in a solid specimen .....	60
Fig. 23. Isotropic hardening curve used for the 0.5% strain amplitude of 0.5% at 300 ° C on a solid specimen .....	60
Fig. 24. Isotropic hardening curve used for the numerical simulation of the 1% strain amplitude at 20 ° C on solid specimen .....	61
Fig. 25. Isotropic hardening curve employed for the numerical simulation of the 1% strain amplitude at 300 ° C in a solid specimen.....	61

Fig. 26. Isotropic hardening curve used for the numerical simulation of 0.3% strain amplitude at 300 ° C in a hollow specimen.....	62
Fig. 27. Isotropic hardening curve employed for the notched specimen numerical simulation of the r = 0.5 mm .....	62
Fig. 28. Isotropic hardening curve employed for the numerical simulation of the notched specimen, r = 2 mm.....	62
Fig. 29. Experimental results: stress curve versus number of cycles for AISI304L stainless steel for 0.3% strain amplitude at 300 ° C .....	65
Fig. 30. Experimental results: stress curve versus number of cycles for AISI304L stainless steel for 0.6% strain amplitude at 300 ° C .....	65
Fig. 31. Experimental results: stress curve versus number of cycles for AISI316L stainless steel for 0.18% strain amplitude at 20 ° C .....	66
Fig. 32. Experimental results: stress versus number of cycles curve for AISI316L stainless steel for 0.6% strain amplitude at 300 ° C .....	66
Fig. 33. Experimental results of solid specimen for 0.5% strain amplitude, stress versus number of cycles at 20 ° C (EDF laboratory test results).....	67
Fig. 34. Experimental results of solid specimen for 0.5% strain amplitude, stress versus number of Cycles at 300 ° C (EDF laboratory test results).....	67
Fig. 35. Experimental results of a solid specimen for 1% strain amplitude, stress versus Number of Cycles at 20 ° C (EDF laboratory test results) .....	68
Fig. 36. Experimental resultsss of a solid specimen for 1% strain amplitude, stress versus Number of Cycles at 300 ° C (EDF laboratory test results).....	68
Fig. 37. Experimental results of a hollow specimen for 0.3% strain amplitude, Stress versus Number of Cycles at 300 ° C (EDF laboratory test results).....	69
Fig. 38. Experimental results for r= 0.5mm notched sample, strain versus number of Cycles at 300 ° C .....	71
Fig. 39. Experimental results for r=2mm notched sample, strain versus number of Cycles at 300 ° C .....	71
Fig. 40. Comparison of simulation results of full specimen and reduced specimen	73
Fig. 41. Mesh sensitivity check .....	74
Fig. 42. First cycle for AISI304L stainless steel at 300 ° C .....	75
Fig. 43. 2000 <sup>th</sup> cycle for AISI304L stainless steel at 300 ° C.....	75
Fig. 44. Stress curve versus number of cycles for AISI304L stainless steel at 300 ° C .....	75
Fig. 45. First cycle for AISI316L stainless steel for 0.18% strain amplitude at 20 ° C .....	76
Fig. 46. 2000 <sup>th</sup> cycle for AISI316L stainless steel for 0.18% strain amplitude at 20 ° C .....	77
Fig. 47. Stress curve versus number of cycles for AISI316L stainless steel for 0.18% strain amplitude at 20 ° C .....	77
Fig. 48. First cycle for AISI316L stainless steel for 0.6% strain amplitude at 300 ° C .....	78
Fig. 49. 500 <sup>th</sup> cycle for AISI316L stainless steel for 0.6% strain amplitude at 300 ° C .....	78

Fig. 50. Stress curve versus number of cycles curve for AISI316L stainless steel for 0.6% strain amplitude at 300 ° C.....	79
Fig. 51. Stress versus strain curve of the solid specimen for 0.5% strain amplitude at 20 ° C.....	79
Fig. 52. Stress versus strain curve of the solid specimen for 0.5% strain amplitude at 300 ° C.....	80
Fig. 53. Stress versus strain curve of solid specimen for 1% strain amplitude at 20 ° C.....	80
Fig. 54. Stress versus strain curve of the solid specimen for 1% strain amplitude at 300 ° C.....	81
Fig. 55. Stress versus strain curve of the hollow specimen for 0.3% strain amplitude at 300 ° C.....	81
Fig. 56. Maximum stress v/s number of cycles for solid experimental and simulation specimen with strain amplitude 0.5% at 20 ° C.....	82
Fig. 57. Maximum stress v/s number of cycles for solid experimental and simulation specimens with strain amplitude 0.5% at 300 ° C.....	82
Fig. 58. Maximum stress v/s number of cycles for the solid specimen experimental and simulation with strain amplitude 1% at 20 ° C.....	82
Fig. 59. Maximum stress v/s number of cycles for solid experimental and simulation specimen with strain amplitude 1% at 300 ° C.....	83
Fig. 60. Maximum stress v/s number of cycles for experimental and simulation hollow specimen at 0.3% strain amplitude at 300 ° C.....	83
Fig. 61. Stress versus strain curve for r=0.5 mm notched specimen at 300°C.....	84
Fig. 62. Maximum stress v/s number of cycles for experimental and simulation r=0.5 mm notched specimen at 300°C.....	84
Fig. 63. Stress versus strain curve for r=2 mm notched specimen at 300°C.....	85
Fig. 64. Maximum stress v/s number of cycles for experimental and simulation r=2 mm notched specimen at 300°C.....	85

## PAVEIKSLŲ SĄRAŠAS

65 pav. Tipinė konstrukcija ir medžiagos: a) PWR ; b) BWR [14].....	96
66 pav. AISI 304L plieno pilnaviduris bandinys, naudotas 0,3 ir 0,6 % deformacijos amplitudei.....	100
67 pav. AISI316L plieno pilnaviduris bandinys, naudotas 0,18 % ir 0,6 % deformacijos amplitudei.....	100
68 pav. AISI 316L plieno bandinys, pilnaviduris bandinys, naudotas 0,5 ir 1 % deformacijos amplitudei.....	100
69 pav. AISI 316L plieno tuščiaviduris bandinys, naudotas 0,3 % deformacijos amplitudės bandymui PWR aplinkoje 300 °C temperatūroje.....	100
70 pav. AISI 316L plieno bandinys su įpjova, kurio įpjovos spindulys yra 0,5 ir 2 mm, 300 °C temperatūroje, kontroliuojant pagal įtempius.....	101
71 pav. Pilnas baigtinių elementų (BE) modelis su pritaikytomis ribinėmis sąlygomis.....	104

72 pav. Taikytos kraštinės sąlygos redukuotam baigtinių elementų modeliui .....	104
73 pav. Tuščiaavidurio bandinio tinklinis baigtinių elementų modelis su pritaikytomis ribinėmis sąlygomis.....	104
74 pav. Tinklinis baigtinių elementų modelis su įpjautam bandiniui pritaikytomis ribinėmis sąlygomis.....	104
75 pav. Santykinė deformacija pritaikyta baigtinių elementų modeliui, kai schema valdoma deformacija .....	105
76 pav. Apkrova, taikyta baigtinių elementų modeliui, kai bandinys su įpjova, $r = 0,5$ mm.....	106
77 pav. Apkrova, taikyta baigtinių elementų modeliui, kai bandinys su įpjova, $r = 2$ mm.....	106
79 pav. AISI 304L nerūdijančio plieno izotropinio kietėjimo kreivė, apskaičiuota esant 0,6 % deformacijos amplitudei 300 °C temperatūroje (naudojama <i>Ansys</i> modelyje).....	112
80 pav. AISI316L nerūdijančio plieno izotropinio kietėjimo kreivė, kurio deformacijos amplitudė yra 0,18 % 20 °C temperatūroje (naudojama <i>LS-DYNA</i> modelyje).....	112
81 pav. AISI316L nerūdijančio plieno izotropinio kietėjimo kreivė, naudojama <i>LS-DYNA</i> modelyje, AISI 316L plienas, esant 0,6 % deformacijos amplitudei 300 °C temperatūroje (naudojama <i>LS-DYNA</i> modelyje) .....	112
82 pav. Izotropinės kietėjimo kreivės, naudotos įpjauto bandinio skaitmeniniam modeliavimui, kai $r = 0,5$ mm .....	112
84 pav. AISI304L nerūdijančio plieno įtempių priklausomybė nuo ciklų skaičiaus, esant 0,3 % deformacijos amplitudei 300 °C temperatūroje .....	114
85 pav. AISI304L nerūdijančio plieno įtempių priklausomybė nuo ciklų skaičiaus esant 0,6 % deformacijos amplitudei 300 °C temperatūroje .....	115
86 pav. AISI316L nerūdijančio plieno įtempių priklausomybė nuo ciklų skaičiaus esant 0,18 % deformacijos amplitudei 20 °C temperatūroje .....	115
87 pav. AISI316L nerūdijančio plieno įtempių priklausomybė nuo ciklų skaičiaus esant 0,6 % deformacijos amplitudei 300 °C temperatūroje .....	116
88 pav. AISI316L nerūdijančio plieno pilnavidurio bandinio įtempių priklausomybė nuo ciklų skaičiaus esant 0,5 % deformacijos amplitudei 20 °C temperatūroje (EDF laboratorijos eksperimentiniai rezultatai) .....	116
89 pav. AISI316L nerūdijančio plieno pilnavidurio bandinio įtempių priklausomybė nuo ciklų skaičiaus esant 0,5 % deformacijos amplitudei 300 °C temperatūroje (EDF laboratorijos eksperimentiniai rezultatai) .....	116
90 pav. 1. AISI316L nerūdijančio plieno pilnavidurio bandinio įtempių priklausomybė nuo ciklų skaičiaus esant 1 % deformacijos amplitudei 20 °C temperatūroje (EDF laboratorijos eksperimentiniai rezultatai) .....	117
91 pav. AISI316L nerūdijančio plieno pilnavidurio bandinio įtempių priklausomybė nuo ciklų skaičiaus esant 1 % deformacijos amplitudei 300 °C temperatūroje (EDF laboratorijos eksperimentiniai rezultatai) .....	117

92 pav. AISI316L nerūdijančio plieno tuščiavidurio bandinio įtempių priklausomybė esant 0,3 % deformacijai 300 °C temperatūroje (EDF laboratorijos eksperimentiniai rezultatai).....	117
93 pav. AISI316L nerūdijančio plieno bandinio su $r = 0,5$ mm įpjova įtempių priklausomybė nuo ciklų skaičiaus 300 °C temperatūroje .....	119
94 pav. AISI316L nerūdijančio plieno bandinio su $r = 2,0$ mm įpjova įtempių priklausomybė nuo ciklų skaičiaus 300 °C temperatūroje .....	119
95 pav. Pilno ir sumažinto bandinių modeliavimo rezultatų palyginimas.....	122
97 pav. Pirmasis AISI304L nerūdijančio plieno ciklas 300 °C temperatūroje.....	122
98 pav. 2000 - asis ciklas nerūdijančiam plienui AISI304L 300 °C temperatūroje	122
99 pav. AISI304L nerūdijančiam plienui įtempių priklausomybė nuo ciklų skaičiaus esant 0,3 % ir 0,6 % deformacijos amplitudėms 300 °C temperatūroje .....	122
100 pav. AISI316L nerūdijančio plieno pirmasis ciklas, kai deformacijos amplitudė yra 0,18 % 20 °C temperatūroje .....	123
101 pav. AISI316L nerūdijančio plieno 2000 - asis ciklas, kai deformacijos amplitudė yra 0,18 % ir 20 °C temperatūroje .....	123
102 pav. AISI316L nerūdijančio plieno įtempių priklausomybė nuo ciklų skaičiaus, esant 0,18 % deformacijos amplitudei 20 °C temperatūroje .....	123
103 pav. AISI316L nerūdijančio plieno pirmasis ciklas, kai deformacijos amplitudė yra 0,6 % 300 °C temperatūroje .....	123
104 pav. AISI316L nerūdijančio plieno 500 - asis ciklas, esant 0,6 % deformacijos amplitudei 300 °C temperatūroje.....	123
105 pav. AISI316L nerūdijančio plieno įtempių priklausomybė nuo ciklų skaičiaus, esant 0,6 % deformacijos amplitudei 300 °C temperatūroje .....	123
106 pav. Pilnavidurio bandinio pirmasis ir 1000 - asis ciklai esant 0,5 % deformacijos amplitudei 20 °C temperatūroje.....	124
107 pav. Pilnavidurio bandinio pirmasis ir 1000 - asis ciklai esant 0,5 % deformacijos amplitudei 300 °C temperatūroje.....	124
108 pav. Pilnavidurio bandinio pirmasis ir 900 - asis ciklai esant 1 % deformacijos amplitudei 20 °C temperatūroje.....	124
109 pav. Pilnavidurio bandinio pirmasis ir 300 - asis ciklai esant 1 % deformacijos amplitudei 300 °C temperatūroje.....	124
110 pav. Tuščiavidurio bandinio pirmasis ir 3000 - asis ciklai esant 0,3 % deformacijos amplitudei 300 °C temperatūroje.....	125
111 pav. Pilnavidurio bandinio įtempių priklausomybė nuo ciklų skaičiaus esant 0,5 %, deformacijos amplitudei 20 °C temperatūroje.....	125
112 pav. Pilnavidurio bandinio įtempių priklausomybė nuo ciklų skaičiaus esant 0,5 % deformacijos amplitudei 300 °C temperatūroje.....	125
113 pav. Pilnavidurio bandinio įtempių priklausomybė nuo ciklų skaičiaus esant 1 % deformacijos amplitudei 20 °C temperatūroje.....	125
114 pav. Pilnavidurio bandinio įtempių priklausomybė nuo ciklų skaičiaus esant 1 % deformacijos amplitudei 300 °C temperatūroje.....	125
115 pav. Tuščiavidurio bandinio įtempių priklausomybė nuo ciklų skaičiaus esant 0,3 % deformacijos amplitudei 300 °C temperatūroje.....	125

116 pav. Pirmasis, 900 - asis ir 12000 -asis ciklai, kai bandinio įpjova $r = 0,5$ mm 300 °C temperatūroje.....	126
117 pav. Įtempių priklausomybė nuo ciklų skaičiaus, kai bandinio įpjova $r = 0,5$ mm 300 °C temperatūroje.....	126
118 pav. Pirmasis ir 1000 - asis ciklai, kai bandinio įpjova $r = 2$ mm 300 °C temperatūroje.....	126
119 pav Įtempių priklausomybė nuo ciklų skaičiaus, kai bandinio įpjova $r = 2$ mm 300 °C temperatūroje.....	126

## LIST OF ABBREVIATIONS AND TERMS

### Abbreviations:

$N_f$ : fatigue life;  
 $t_h$ : holding time;  
 $R_t$ : surface roughness;  
 $\Delta\varepsilon_p / 2$ : plastic strain amplitude;  
 $\Delta\varepsilon_e / 2$ : elastic strain amplitude;  
 $2N_f$ : number of reversals to failure;  
 $\varepsilon_f'$ : fatigue ductility coefficient;  
 $E$ : modulus of elasticity;  
 $\sigma_f'$ : fatigue strength coefficient;  
 $\sigma_m$ : mean stress;  
 $\sigma_a$ : stress amplitude;  
 $\varepsilon_1, \varepsilon_2, \varepsilon_3$ : principal strain;  
 $\varepsilon_a$ : total strain amplitude;  
 $b$ : fatigue strength exponent;  
 $c$ : fatigue ductility exponent;  
 $\varepsilon_f'$ : fatigue ductility coefficient;  
 $S_e$ : fatigue strength of material;  
 $S_u$ : ultimate tensile strength;  
 $\Delta\varepsilon_{pl}$ : plastic strain range per cycle;  
 $\sigma_{\max,i}$ : maximum stress for the current cycle;  
 $\sigma_{y,o}$ : initial yield stress;  
PWR: pressurised water reactor;  
LCF: low cycle fatigue;  
HCF: high cycle fatigue.

## INTRODUCTION

Structures operating in hazardous environmental conditions often experience long-term degradation of their surfaces due to erosion and corrosion. This leads to a reduction in cross-sectional wall thickness, an increase in surface roughness, irregularities, and corrosion pitting, as well as a decrease in material strength [1], which affects the durability of these structures.

Most components designed with austenitic stainless steel include parts exposed to variable or cyclic loads. Components exposed to repeated or cyclic strain or stress loading often fail even though the actual maximum stresses are below the ultimate tensile strength of the material, usually at stress levels even below the yield strength. Although numerous elements of the structure may operate effectively at first, they frequently undergo fatigue failure under service load due to repeated cyclic loading. The most notable characteristic is that the failure happened only after applying the stresses a significant number of times [2]. Progressive degradation resulting from the cyclic loading of a component or material, which eventually results in crack initiation and subsequent fractures, is commonly referred to as “fatigue” by practicing engineers [3]. Approximately 95% of all structural failures arise from a fatigue mechanism [2]. Fatigue arises from localised microstructural deformations, which are significantly influenced by factors such as magnitude, frequency, fluctuating stresses, temperature, environmental conditions, geometrical complexity, material imperfections, and discontinuities, resulting in a dislocation density significantly higher than that observed under monotonic loading. The continued cycle of dislocations will result in the formation of dislocation structures, including well-defined cell structures and, ultimately, persistent slip bands [3,4]. Subsequently, results in microcrack initiation, aggregation, and macroscopic crack propagation [3]. Consequently, crack initiation is the only reliable method for evaluating the residual fatigue life, as it is derived from the inherent properties of the fatigue phenomenon [3]. Localised plastic deformation occurs in areas where stress is concentrated on cracks during cyclical loading. The component experiences permanent damage, resulting in the formation of a crack due to plastic deformation. As the number of loading cycles increases, there is a corresponding increase in the crack length. Following a specific number of cycles, the presence of cracks will lead to failure of the component [2].

Environmentally assisted fatigue (EAF) is a condition that can decrease the fatigue life of components in nuclear power plants. Test programmes conducted in Japan, the United States, and later in Europe have demonstrated that the water environment in nuclear power plants significantly reduces their fatigue life, denoted as  $N_f$ . However, the currently operating NPP fleet did not explicitly consider EAF during its construction [5].

In the period 2015-2020, the European Commission initiated the INCEFA-PLUS (Enhancing Nuclear Power Plant Safety by Closing the Gaps in Environmental Fatigue Assessment) project under the H2020 programme. During this project, low cycle fatigue (LCF) tests were performed, assessing the operating conditions of a nuclear power plant and ensuring realistic test durations [5–7]. The main objective of

the project was to investigate how fatigue life ( $N_f$ ) varies depending on various factors: the deformation range (difference between the maximum and minimum deformations), the average deformation, the holding time at constant deformation, the surface roughness ( $R_t$ ) of the specimen and the environmental conditions. During the project, more than 250 fatigue tests were performed in various European laboratories in both air and water environments [5]. The frequency of successful operations of the components and structure is greater than that of their mechanical failures [8]. The most notable characteristic is that the failure only happened after applying the stresses a significant number of times. Fatigue represents a mode of failure and accounts for the majority of failures in mechanical components and structures [8]. The analysis of recent scientific papers and international projects aimed at solving experimental studies of cyclic fatigue and simulation problems shows that the finite element method (FEM) enables us to describe/predict the behaviour of a metal under the effect of cyclic loading and to predict the cyclic fatigue of a metal depending on temperature and time factors. The results of these original, numerical simulation studies are reflected in the publications of the Clarivate Analytics database and received considerable attention from the researchers (a list of references included).

In the period 2020-2025, the European Commission initiated the INCEFA-Scale (improve the prediction of fatigue life of the components subjected to environmentally assisted fatigue loading in nuclear power plant) project under the H2020 programme. This project was built upon the research conducted by its predecessor, INCEFA-PLUS. INCEFA-SCALE aims to advance the understanding and predictive capabilities regarding environmental-assisted fatigue (EAF) in nuclear power plant components, ultimately contributing to improved lifetime prediction [143]. Low cycle fatigue tests were performed on the specimens made by AISI 316L stainless steel and based on the testing results, models / methods are developed to extrapolate lab tests to component scale and producing guidance for use in engineering assessments of NPP components [9].

However, there are still unresolved issues of numerical investigation, including those related to the number of fatigue cycles at which the material should break down and the assessment of steel parameters characterising the softening/hardening of the material during fatigue.

The determination of kinematic hardening parameters for numerical prediction based on experimental results is an extremely complex and time-consuming task. In addition, these parameters usually need to be calibrated so that the simulation results correspond to the experimental ones. Therefore, it is necessary to simplify the process of estimating kinematic hardening parameters while ensuring the reliability of the simulation results.

## **Aim and Objectives**

The aim of this research is to develop a simplified and robust methodology to determine the material parameters which govern the kinematic and isotropic hardening of the austenitic stainless steel, using experimental low-cycle fatigue (LCF) testing and finite element (FE) modelling. The methodology will enable reliable

determination of cyclic hardening/softening behaviour and provide validated predictive capability for LCF performance through direct comparison of numerical simulations with experimental results. To achieve this aim, following objectives were decided and solved:

1. To develop a comprehensive experimental matrix for performing the low-cycle fatigue (LCF) testing on AISI 316L austenitic stainless steel under strain- and stress- controlled regime, exposed to both constant and variable amplitude loading, for generating high quality data of cyclic stress-strain response, fatigue life to develop and validate the numerical simulation model.
2. To develop finite element model capable of capturing the cyclic elasto-plastic and hardening/softening behaviour of austenitic stainless steel using constitutive rules for the kinematic hardening and calibrating the model parameters with experimental data.
3. To develop a simplified and reproducible methodology for the determination of the hardening and softening parameters of AISI 316L stainless steel for minimizing the requirement of experiment results while maintaining the accuracy and reliability of the estimated parameters.
4. To perform numerical simulations of low-cycle fatigue and validate the results of the developed models by comparing the simulation results with corresponding experimental results.

## **Research Methods**

Both experimental and numerical simulation research methods were applied in the dissertation work. The results of the experimental research were used for modelling and determining material parameters for low-cycle fatigue evaluation. The software “Ansys Workbench” and “LS-DYNA” were used for numerical modelling and “SolidWorks” for 3D modelling. The testing machine “Instron ElectroPlus E10000” dynamic-static testing tensile-torsion machine (+/- 10 KN tensile force, +/- 100 Nm torsion force, test temperature -70°C – 350°C) was used for experimental work. The numerical simulation results were verified by the results of experimental research conducted at the Department of Mechanical Engineering of Kaunas University of Technology, the Lithuanian Energy Institute, and the laboratories of “Electricity de France” (EDF, France).

## **Scientific Novelty**

1. A simplified and reproducible methodology for determining the kinematic hardening parameters for low-cycle fatigue of AISI 316/316L austenitic stainless steel is proposed. In this procedure the effects of operating temperature, strain amplitude on these parameters is considered and the requirement of experimental results is reduced while keeping the accuracy of the model.
2. The proposed methodology for determining kinematic hardening parameters eliminates the need to additionally calibrate these parameters according to experimental results to capture the elasto-plastic behaviour of steel during low-cycle fatigue (LCF) simulations, since this methodology allows for reliable

prediction of kinematic hardening parameters using only strain amplitude and operating temperature data.

### **Defended Statements**

1. Accurate prediction of the elastic–plastic and cyclic response of austenitic stainless steels in numerical models fundamentally depends on precisely estimated isotropic and kinematic hardening parameters; these parameters govern hysteresis loop shape, mean-stress evolution and therefore influence the low-cycle fatigue life predictions.
2. The determination of kinematic hardening parameters using conventional approaches is often complex, time-consuming, and highly dependent on extensive experimental data. Therefore, there is a need to develop a simplified, fast, and reliable procedure for estimating these parameters, while reducing the method's dependency on experimental results.
3. Finite element analysis employing kinematic hardening models provides an effective, efficient, and cost-saving alternative to experimental testing for investigating the low-cycle fatigue behaviour of steel.

### **Practical Value**

1. Low cycle fatigue behaviour of autenitic stainless steel can be estimated using proposed methodology for numerical simulation without the requirement of experimental tests data to estimate and calibrate the material parameters.
2. The kinematic hardening parameters estimated using the formulated relations between strain amplitude and operating temperature, effectively captures the elasto-plastic behaviour of steel during low-cycle fatigue, ensuring a realistic material response in numerical simulations.
3. The proposed relations for the estimation of kinematich hardening parameters simplify the process of determining these parameters under low-cycle fatigue, reducing the required number of tests and at the same time the research time. In addition, it reduces the need to perform additional parameter calibrations after their determination, which makes the modelling process more efficient and accessible for engineering applications.

### **Research Approbation**

The results of the study were published in 3 articles in international journals with a citation index (impact factor) and included in the Web of Science databases. The results were also presented at 4 international conferences, 3 articles were published in peer-reviewed conference proceedings included in the Web of Science databases, and one abstract was included in the international conference proceedings.

### **Structure of the Dissertation**

The doctoral dissertation consists of an introduction, 5 chapters, and general conclusions. Chapter 1 reviews scientific literature on low-cycle fatigue. A literature review on the phenomenon of fatigue, the characteristics of low-cycle fatigue, a review of experimental studies on low-cycle fatigue and numerical modelling are

presented. Chapters 2 and 3 present the methodologies of experimental and numerical modelling, which include the preparation of the experimental matrix, the preparation of a finite element model and a material model for numerical prediction. Chapters 4 and 5 present the results of experimental and numerical modelling and the validation of the results of numerical simulation with experimental results. The conclusions present the results of experimental research and numerical prediction. A list of literature sources with 143 references and a list of the author's scientific publications are provided. This doctoral dissertation consists of 148 pages, 119 figures and 26 tables.

## 1. LITERATURE REVIEW

Operational life of the structures and components are highly affected by the fatigue driven degradation, influenced by factors such as load magnitude, frequency, operating temperature and environment. Fatigue contributes to nearly 25% of all reported failures in operating nuclear power plants, leading to a thorough historical analysis of this ageing mechanism [10]. Temperature fluctuations resulting from start-ups and shutdowns, power variations, strain, thermal stratification, and striping contribute to thermomechanical fatigue [11].

Austenitic stainless steel is the preferred material for numerous cooling pipes in the primary circuit of pressurised water reactors (PWR) in nuclear power plants, where high temperatures, irradiation, and intricate thermomechanical loading conditions prevail. Components made of austenitic stainless steels are widely used under harsh conditions, such as high temperature, repetitive loading. These components are exposed to thermal and/or mechanical cyclic strain and stresses, due to which thermos-mechanical fatigue can be observed and experience the fatigue failure [11]. Fatigue failure can be defined as the number of loading cycles required for the specimen to fail. Depending on the number of cycles required for the component to fail, the fatigue failure can be bifurcated into two categories. These categories correspond to high and low cycle fatigue failure, respectively.

### 1.1. High-Cycle Fatigue Failure

High-cycle fatigue is the most challenging phenomenon in solid mechanics and is the primary cause of mechanical component failure during service [2]. Fatigue is classified as high-cycle fatigue when it results from comparatively lower stress levels applied over a substantial number of cycles (greater than  $10^5$  cycles before failure) [2]. The high begins with the initial damage caused by pre-existing defects in components subjected to stresses below the yield strength [2]. High cycle fatigue (HCF) is defined by its low stress amplitude and higher frequency. In this scenario, the stress remains below the yield strength of the material, resulting in minimal elastic strains [13, 14]. Once the strain accumulates over a considerable number of cycles, it results in failure. The precise number of cycles associated with high-cycle fatigue, in contrast to low-cycle fatigue fractures, depends on the material's actual behaviour. The cycle count is so high that the resulting stresses must remain below the material's endurance limit, or efforts should be made to mitigate the causes of HCF [13]. The prevailing strain in HCF is elastic, and the corresponding fatigue life is defined by stress (instead of strain) in a stress-life (SN-curve) plot. The logarithmic scale of the number of cycles until failure illustrates cyclic stress [14].

## 1.2. Low-Cycle Fatigue Failure

Low-cycle fatigue (LCF) is defined by its high stress amplitude and low frequency [13, 14]. Low-cycle fatigue failure is strain-controlled and associated with elevated stress levels or significant strain amplitudes, resulting in plastic and elastic components for each loading cycle [13, 14]. This feature has significant relevance in regions characterised by geometric discontinuities or stress risers. Consequently, due to plastic deformation in low-cycle fatigue, failure occurs after fewer cycles compared to high-cycle failure.

Furthermore, LCF can be initiated by material flaws that arise during manufacturing and subsequent processes [14]. When the component's deformation reaches the threshold for inelastic behaviour, the structure deteriorates. When a crucial component of a structure fails at a deformation level significantly below its capacity, the structure experiences hysteretic deterioration [2]. If the elastoplastic response fails because the stress goes beyond the yield stress after a few loading cycles ( $10^5$  cycles), this kind of fatigue failure is known as low-cycle fatigue (LCF). Low-cycle fatigue can be divided into four steps and two stages with respect to crack growth in microstructural evolution [13].

Step 1: Unstable softening and hardening are evident, indicating the initiation of surface cracks, marking the onset of fatigue damage [13].

Step 2: Cracks emerge or begin to form on the surface subjected to high shear stresses, and the crack propagates gradually inward; this phase is called stage I crack growth [13].

Step 3: This stage is known as stage II crack growth, during which cracks in the planes of the high tensile stress planes propagate perpendicularly to the applied load [13].

Step 4: Fracture occurs in the reduced area after the fully developed cracks [13].

Low cycle fatigue is induced by significant variations in stress, temperature, and other factors [15]. LCF can be defined independently, allowing its assessment and analysis regarding the design lifetime of the components [15]. Low cycle fatigue significantly affects the material properties due to the high temperature, pressure and repetitive loading conditions [12].

The low-cycle fatigue characteristics of the steel used in the structure play a significant role in its design when exposed to a large cyclic strain loading [16]. Studying the characteristics of LCF increases the understanding of the nonlinear response and degradation of the structure [13]. LCF is a critical design factor for metallic machine components and steel structures, making it a prominent subject of research.

## 1.3. Austenitic Stainless Steel

The term austenitic describes the crystal structure found in the steel. Austenitic stainless steels are referred to as such because their stable FCC (face-centered cubic) austenite microstructure is maintained at room temperature, due to the presence of

nickel. Table 1 illustrates the primary distinctions among the various types of stainless steels. Austenitic stainless steels exhibit superior toughness, enhanced corrosion resistance, and improved weldability compared to ferritic or martensitic steels, which contributes to their prevalence as the most commonly utilised type of stainless steels in power plants and various other industries.

**Table 1.** Overview of stainless-steel types and their key characteristics [17]

Type	Crystal Structure	Key Alloying Elements	Main Properties	Examples
<b>Austenitic</b>	FCC (face-centered cubic)	High Cr (16–20%), Ni (8–12%), sometimes Mo, N	Non-magnetic, excellent corrosion resistance, good weldability, high ductility, good at cryogenic and high temps	304, 304L, 316, 316L
<b>Ferritic</b>	BCC (body-centered cubic)	High Cr (11–18%), very low Ni	Magnetic, lower toughness, moderate corrosion resistance, cheaper	430, 446
<b>Martensitic</b>	BCT (body-centered tetragonal)	11–18% Cr, higher C (0.1–1.2%)	Magnetic, very hard and strong, but lower corrosion resistance	410, 420, 440C
<b>Duplex</b>	Mix of FCC (austenite) + BCC (ferrite)	18–28% Cr, 4–7% Ni, some Mo, N	Balanced: higher strength, good corrosion resistance	2205, 2507
<b>Precipitation-Hardening (PH)</b>	Martensitic or semi-austenitic	Cr, Ni, Cu, Al, Nb, Ti	Can be heat-treated for very high strength with decent corrosion resistance	17-4PH

The components undergoing cyclic or repetitive loading in harsh environments such as high-temperature pressure are manufactured with austenitic stainless steel. Austenitic stainless steels are widely used in nuclear power plants due to their

exceptional mechanical properties at elevated temperatures. Table 2 presents the comparison between AISI 304L and AISI 316L stainless steel. These properties make these materials ideal for application in the components working at high temperatures. Austenitic 304L and 316L SS have high resistance to corrosion, oxidation, pitting, etc. AISI 316L SS exhibits stable behaviour under neutron irradiation, which makes it suitable for application in the core internals and fuel cladding. This type of stainless steel also possesses properties such as being non-magnetic, having improved weldability, and enhanced fabricability. In environments such as primary coolant loops of nuclear power plants, which require high purity of water under the pressure and elevated temperature these steels are used for these purposes. Also, these steels have been used in pressurised water reactors (PWRs) and boiling water reactors (BWRs) for several decades and have good performance and characteristics under operational and accidental conditions [18].

**Table 2.** Comparison of AISI 304L and AISI 316L stainless steels and their relevance in power plant applications [17]

Property	AISI 304L	AISI 316L	Relevance in Power Plant
<b>Chemical Composition</b>	18–20% Cr, 8–12% Ni, low C (<0.03%)	16–18% Cr, 10–14% Ni, 2–3% Mo, low C (<0.03%)	Mo addition in 316L greatly improves resistance to chlorides and acidic media.
<b>Corrosion Resistance</b>	Excellent general corrosion resistance; prone to pitting in chloride environments	Superior resistance to pitting, crevice corrosion, and acids (due to Mo)	316L preferred in cooling water systems, marine/coastal plants, and aggressive environments.
<b>Oxidation/Scaling Resistance</b>	Up to ~870 °C (intermittent); ~925 °C (continuous)	Similar, but slightly better creep resistance at high temperature	Suitable for boilers, heat exchangers, superheaters.
<b>Mechanical Properties (Annealed)</b>	Yield: 170–240 MPa; Tensile: 485–620 MPa; Elongation: ~40%	Yield: 170–290 MPa; Tensile: 485–620 MPa; Elongation: ~40%	Both maintain ductility and strength at high temperatures; 316L has better creep strength.
<b>Weldability</b>	Excellent; low carbon prevents sensitization	Excellent; low carbon + Mo → stable against	Important for large, welded structures (boiler tubes,

		sensitization in corrosive service	piping, reactor components).
<b>Cost</b>	Lower (more economical)	Higher (due to Mo content)	304L often chosen for cost-sensitive applications; 316L where service conditions demand better corrosion resistance.
<b>Typical Applications in Power Plants</b>	Boilers, pressure vessels, condensers, turbine casings, steam piping	Heat exchangers, condenser tubes (esp. seawater cooling), nuclear reactor cooling systems, high-chloride environments	304L = general use; 316L = critical parts exposed to corrosive media.

Figure 1 shows the typical design of PWR and BWR with the materials used for it. BWR (boiling water reactor) (Figure 1b) is a type of light water nuclear reactor in which water is used for both coolant and moderator. Water is boiled in the reactor core to convert it to steam, which is supplied to the turbine to generate power. BWR typically works at 7-8 MPa pressure. A pressurised water reactor (PWR) has two separate circuits: primary and secondary. The primary circuit operates at a temperature between 275 and 315°C and 15.5 MPa pressure. The heat is exchanged between the primary and secondary circuits' water in the steam generator, then the water from the low-pressure steam generator converts to steam and runs the turbine. The pressure in the primary circuit of PWR is maintained with the pressuriser, which works by heating the water to the boiling point at the required pressure with submerged electrical heaters [19]. Another type of reactor which is a compact nuclear reactor called a small modular reactor (SMR) is a next-generation reactors. SMRs are designed to be fabricated in the factories and transported to the site, such as rural areas, industries, etc. The focus on SMR is to enhance safety and cost-effectiveness; it can generate power output in the range of 10-300 MW. SMR can operate for more than 10 years without refuelling.

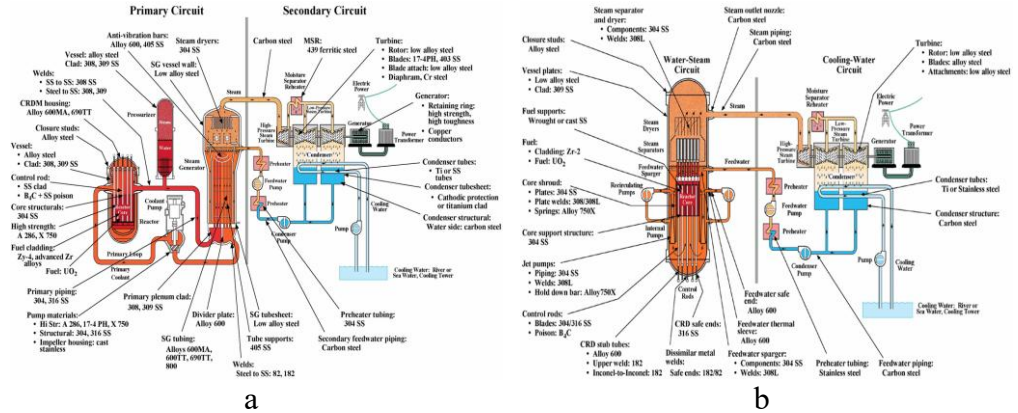


Fig. 1. Typical design and materials in a) PWR, b) BWR [15]

Next-generation reactors like generation IV reactors are developed for the improvement of safety, reduction of nuclear waste, efficient use of fuel, etc. Gas-cooled fast reactor (GFR), lead-cooled fast reactor (LFR), molten salt reactor (MSR), sodium-cooled fast reactor (SFR), supercritical water reactor (SCWR), and very high temperature reactor (VHTR) are some of the generation IV reactors. Austenitic stainless steel is used for fuel cladding, pressure vessels, internal core structure, coolant circuit pipes, cladding of control rods, heat exchangers, and condensers in PWRs, BWRs, SMRs, and generation IV reactors. All these components operate at high temperatures and under pressure.

#### 1.4. Fatigue Loading

The fatigue is caused by repeated or cyclic loading. Based on the loading amplitude changes, there are two types of loading, constant amplitude loading and variable amplitude loading.

In the practical scenario, the magnitude of the mean loading and its amplitude are important. The fatigue stress is calculated according to the loading; the stress needs to be calculated for the period. Due to this, it becomes a bit tricky to calculate the stress in the case of variable amplitude loading.

The type of mean stress in the fatigue loading is represented with the loading ratio (R). This 'R' value shows the means stress is positive, negative or zero.

The load ratio (R) can be calculated as in equation (1):

$$R = \frac{\sigma_{min}}{\sigma_{max}} ; \quad (1)$$

Based on the load ratio (R), fatigue loading is bifurcated into three types: R = -1, R = 0, and R = 1. Figure 2, shows the loading waveform based on the load ratio.

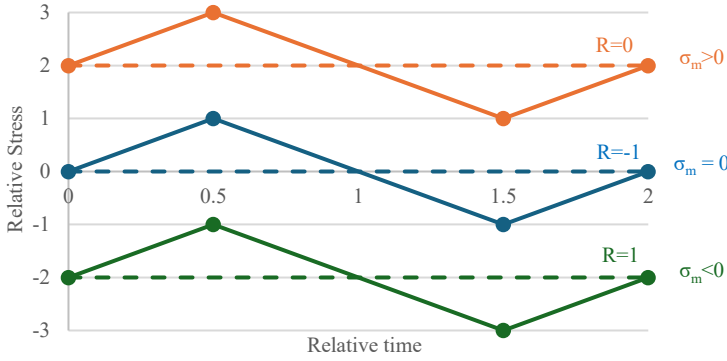


**Fig. 2.** Loading waveform for different loading ratio

The negative load ratio represents the alternating load in this case mean stress is zero. For tensile pulsating load where, mean stress is positive load ratio (R) is zero. The positive load ratio is the pulsating (compression) loading with negative mean stress.

### 1.5. Fatigue Life

Fatigue life refers to the total number of cycles required for a crack to fully propagate and cause fracture. This parameter assesses the ability to withstand defects. The number of cycles ( $N_f$ ) necessary for the material to experience failure as a result of cyclic stress is inversely related to the alternating stress and strain [14].

For decades, the fatigue life of materials in engineering has been a significant challenge and a specialised area of study. Fatigue accounts for approximately 50% to 90% of all mechanical failures [20].

Fatigue damage is governed by the fluctuation of stress and not by the maximum stress ( $\sigma_{max}$ ), or the stress amplitude ( $\sigma_a$ ). The mean stress ( $\sigma_m$ ) plays a critical role in estimating fatigue equation (2). The stress range ( $\Delta\sigma$ ) is used for the welded components, and the stress amplitude is used for the machined components [21]. The stress range can be calculated using the following formula:

$$\Delta\sigma = \sigma_{max} - \sigma_{min} = 2 \sigma_a; \quad (2)$$

The surface condition of a component significantly influences its fatigue life, as fatigue cracks usually initiate on the free surface [2]. Surface roughness must be regarded as a stress concentrator, with residual stresses introduced by the machining process in the surface layer, along with hardening or softening of the surface layer and microstructure alterations resulting from plastic deformation [22]. Assessing fatigue strength influenced by surface finish is a complex and critical process; consequently, it is essential to assess the impact of each factor independently before integrating them [22].

To assess the potential for failure and the service life of a component that has an existing crack or similar defect, it is crucial to perform crack propagation analyses [15]. Through experimentation, it has been observed that the crack growth rate per

cycle,  $da/dN$ , is correlated with variations in the stress intensity factor  $\Delta K$ , as illustrated in equation (3).

$$\frac{da}{dN} = A \Delta K^m; \quad (3)$$

The relation in equation (3) is recognised as the Paris law, with the parameters ‘A’ and ‘m’ influenced by various factors, including environment, material properties, load frequency, stress ratio and temperature [16].

When cracks arise from corrosion without the influence of cyclic fatigue, equation (4) can express the relations between  $da/dt$  (the rate of crack growth over time) and the applied stress intensity ‘K’.

$$\frac{da}{dt} = B K^n; \quad (4)$$

When George Antaki and Ramiz Gilada [15] examined the experimental situation, they involved a great number of variables compared to the  $da/dN$  relation.

The overall fatigue life  $N_f$  consists of two distinct phases: the crack initiation phase  $N_i$  and the crack propagation phase  $N_p$  [21]. In most cases, the largest chunk of fatigue life is consumed by the initiation of cracks, which is subsequently followed by a relatively quick propagation of those cracks. However, when examining welded structures, it is evident that small cracks or similar defects are often present during production, leading to the conclusion that the entire useful life is effectively consumed by the propagation phase [21]. The surface condition significantly influences the crack propagation phase and is less dependent on the strength of being dependent on the material's elastic modulus [21]. Given that the two phases operate under different mechanisms, it is crucial to differentiate between them [21]. Currently, there is a lack of a universally accepted quantitative measure to clearly distinguish between the conclusion of the first phase and the beginning of the second phase. In some cases, a single cycle can be enough to generate a microscopic crack [21].

Accelerating the initiation of fatigue cracks, followed by their growth, can reduce fatigue life. Mechanical and residual thermal stresses, caused by a severe non-uniform temperature distribution in the heat-affected zone around the weld, have an impact on the evolution of the microstructure [13]. Some studies have found that eliminating residual stress does not improve low-cycle fatigue strength and its effects, so it can be ignored because significant plasticity may occur as a result of external loading, which reduces residual stress [13]. For the design and maintenance of components subjected to fatigue, accurate prediction of fatigue life is essential [20]. An accurate prediction of fatigue endurance is essential for the design of an element affected by fatigue [23]. The use of finite element software for fatigue analysis has gained significant popularity due to the high costs associated with laboratory experimental investigations. The design guidelines outlined in the code of practice are applicable primarily to simple shapes [23].

## 1.6. Fatigue Analysis

Estimating the fatigue life of the components operating under cyclic loading, exposed to corrosive environments, etc., is essential to eliminate the unexpected failure of the components.

### 1.6.1. SN Curve

The SN curve is a simplified way to represent the results of the fatigue test [15]. The SN curve is expressed as the number of cycles ( $N$ ) as a function of the applied alternating stress intensity ( $S$ ) for various materials [15]. The equivalent elastic stress is calculated by multiplying strain, the modulus of elasticity, and a correction factor that accounts for plasticity effects. The procedure results in the ordinates of the fatigue curves being in the range of hundreds of ksi [15].

The SN curve is expressed on a log-log scale (Figure 3). A point on the curve is called the “knee point”. The knee point is identified in a specific range of loading cycles, typically between  $10^6$  and  $10^7$ . The SN curve consists of two distinct sections: the primary section is located to the left of the knee point, characterised by slope  $m_1$ , and the secondary section is positioned to the right of the knee point, characterised by slope  $m_2$ . The value of ‘ $m$ ’ represents the negative reciprocal of the slope, and it falls within the range of 3-10 for the primary segment of the SN curve. The fatigue strength can be expressed in terms of range or amplitude [21].

The behaviour of the SN curve exhibits distinct characteristics in both sections, with the knee sometimes displaying two forms following the kneepoint. The initial form typically produced in laboratory tests is a flat line, while the second form, observable in real-world scenarios, exhibits a gradual decline over time [21]. In the context of flatline, fatigue strength can be considered the fatigue limit, as it may not be evident under variable-amplitude loading. Furthermore, certain materials may not have a fatigue limit under specific conditions [21].

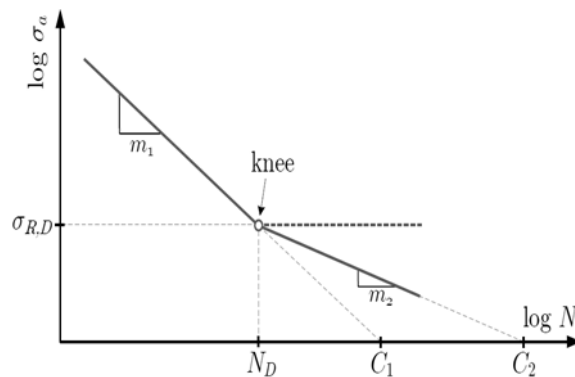


Fig. 3. Representation of bilinear SN curve [21]

If the fatigue capacity is known from the SN curve, then we can estimate the fatigue life of the component for the corresponding stress amplitude by employing the following equation (5).

$$N \sigma_a^m = C; \quad (5)$$

Fatigue capacity (C) is the intercept of the SN curve with the axis for the number of cycles at the stress amplitude of 1 (i.e.,  $\sigma_a=1$ ). The allowable stress amplitude ( $\sigma_a$ ) can be estimated using the following relation presented in equation (6). This stress amplitude ( $\sigma_a$ ) is required for the estimate of fatigue life ( $N_f$ ).

$$\sigma_a = \sqrt[m]{\frac{C}{N}}; \quad (6)$$

For the fatigue analysis, there are three methods, namely the experimental method, the analytical method, and the numerical method; each method has its significance. The experimental method is an expensive, difficult, and complex process of creating and maintaining the required environment throughout the experiment's life. The analytical method is a time-consuming and complex process for obtaining a solution. Numerical methods, such as the finite element method, use constitutive models in computer software to provide approximate solutions that may contain errors.

### 1.6.2. Experimental Method

Experimental techniques that have been consistently employed to investigate the significance of cyclic stresses include component tests and polished bar specimen tests [15].

#### a. Component Testing

This technique for evaluating fatigue is one of the oldest and relies on cyclic component tests. This method was employed in the formulation of stress intensification factors (SIF) for plumbing components. The SIF methodology is utilised for the examination of ASME III class 2 and 3 piping systems [15].

#### b. Polished Bar Specimen Testing

This technique involves the development of SN curves, or stress cycle curves, for various polished bar specimens produced from different materials. An adjustment factor of 20 is applied to stress, and a factor of 2 is applied to cycles to obtain the ASME II design fatigue curve from the failure SN curves. To replicate the stress concentration that results from shape discontinuities and localised plasticity within the component, the calculated stress is adjusted using the stress concentration factor for the SN curve [15].

The experimental approach has been used extensively for an extended period. However, predicting structural life using experimental methods is considerably more costly. Moreover, performing experiments on certain intricate systems is challenging [24].

### 1.6.3. Analytical Method

For the analytical method, no knowledge of the software is necessary to perform the analysis. Several analytical models were proposed in several works by the authors. These analytical models can be combined with coding software such as MATLAB for mathematical solutions. This process reduces the time consumed for the physical calculation.

Coffin and Manson [22, 25] proposed a constitutive model to describe the relations between plastic strain and fatigue life for the low-cycle scheme; equation (7) presents the Coffin-Manson relation.

$$\frac{\Delta \varepsilon_p}{2} = \varepsilon'_f (2N_f)^c ; \quad (7)$$

Basquin [26] proposed a constitutive model to describe the relation between plastic strain and fatigue life in an elastic nature. The Basquin's equation is presented in equation (8).

$$\sigma_a = \frac{\Delta \varepsilon_e}{2} = \frac{\sigma'_f}{E} (2N_f)^b ; \quad (8)$$

The Coffin-Manson-Basquin model is a combination of the Coffin-Manson relationship [25-27] and the Basquin relationship [28]. This model is investigated for several materials because of its ease of application and simplicity. Equation (9) represents the Coffin-Manson-Basquin relation [28].

$$\varepsilon_a = \left( \frac{\sigma'_f}{E} \right) (2N_f)^b + \varepsilon'_f (2N_f)^c ; \quad (9)$$

The total strain amplitude is composed of the elastic strain amplitude and the plastic strain amplitude. The parameters for the Coffin-Manson-Basquin model are temperature-dependent. Equation (9) can predict the fatigue life based on the specified total strain amplitude [28]. Marrow [29] and Smith-Watson-Topper [30] further modified the Coffin-Manson-Basquin model, taking into account the mean stress effect.

Equations (10) and (11) represent the Marrow's and SWT (Smith-Watson-Topper) equations, respectively. Morrow's equation targets the elastic strain, due to which it is effective with constant amplitude or compression mean stress. On the other hand, SWT cannot be applied to the mean compressive stress.

$$\varepsilon_a = \left( \frac{\sigma'_f}{E} \right) \left( 1 - \frac{\sigma_m}{\sigma'_f} \right) (2N_f)^b + \varepsilon'_f \left( 1 - \frac{\sigma_m}{\sigma'_f} \right) (2N_f)^c ; \quad (10)$$

$$\sigma_{max} \varepsilon_a = \left( \frac{\sigma'^2_f}{E} \right) (2N_f)^{2b} + \sigma'_f (2N_f)^{b+c} ; \quad (11)$$

Brown and Miller introduced the theory of multiaxial shear stress fatigue to prevent the crack nucleation phase [31, 32]. Equation (12) represents the maximum shear strain criterion, and equation (13) presents the Brown-Miller criterion [33, 34].

$$\frac{\Delta \gamma_{max}}{2} = 1.3 \frac{\sigma'_f}{E} (2N_f)^b + 1.5 \varepsilon'_f (2N_f)^c ; \quad (12)$$

$$\frac{\Delta\gamma_{max}}{2} + \frac{\Delta\varepsilon_n}{2} = 1.65 \frac{\sigma'_f}{E} (2N_f)^b + 1.75 \varepsilon'_f (2N_f)^c ; \quad (13)$$

here:

$$\varepsilon_n = \frac{\varepsilon_{max} \cdot \varepsilon_{min}}{2}$$

$$\sigma_{max} = \sigma_a + \sigma_m$$

The maximum shear strain criterion indicates a conservative result, and the Brown-Miller criterion presents a satisfactory life estimate. Both criteria are generally recommended for ductile metals [34]. For brittle metals, the main strain criteria are generally recommended [34].

Equation (14) shows the Goodman straight-line expression, which can be used for low-ductility materials, such as high-strength steel and cast iron.

$$\frac{\sigma_a}{s_e} + \frac{\sigma_m}{s_u} = 1 ; \quad (14)$$

The Goodman's diagram serves as the predominant approach for estimating the endurance limit associated with a specific set of alternating or mean stresses [15]. The Goodman straight line is used to straight-line to provide information on the fatigue limit of the material.

#### 1.6.4. Numerical Method

The process of creating a fatigue curve is exorbitant, requires a significant time investment, and poses challenges in executing experiments within reactor conditions, such as extreme temperatures and varying alkalinity levels. The numerical simulation serves to identify key points for constructing a fatigue curve and enhances our understanding of the mechanics behind the fatigue mechanism [4]. There are several numerical methods, such as peridynamics (PD), the finite element method, the finite difference method, the meshless method, and the boundary element method, to analyse fatigue behaviour, crack growth, etc. Peridynamics (PD) is another option of classical continuum mechanics (CCM) [35,36]. The classical continuum mechanics equation is modified to become without spatial derivatives for the PD, which is the integral equation of motion, which is useful in the case of fatigue or crack growth modelling [35,36]. Therefore, PD is a different approach than that of the CCM equation [35,36]. Silling [37] kept forward the original PD in the year 2000, which was only applied to the brittle materials. Further, Silling et al. [38], Bobaru and Hu [39], and Madenci [40] developed PD models for both brittle and ductile material [35]. The single PD model can estimate the fatigue crack initiation, growth, and final fracture phases without the predefined crack path [35, 41]. PD can capture the material's hardening behaviour [42]. In contemporary practice, the finite element method has emerged as a widely recognised analytical approach in structural design. The approach results in the development of a discrete framework of matrix equations that encapsulate the mass and stiffness influences of a continuous structure. The matrices typically exhibit banded and symmetric properties. The geometrical

complexity of the structure is unrestricted, as the mass and stiffness matrices are constructed from the contributions of individual finite elements that possess simple shapes. Consequently, every finite element is linked to a mathematical expression that corresponds to a straightforward geometric representation, regardless of the overall shape of the structure. The structure is organised into distinct areas or volumes, referred to as 'elements'. Element boundaries are established when nodal points are linked by a distinct polynomial curve or surface. In widely used elements of the isoperimetric and displacement type, a consistent polynomial description is used to connect the internal displacements of the element to the displacements at the nodes. This method is commonly referred to as shape function interpolation. Given that the boundary nodes are common to the adjacent elements, the displacement field is typically continuous across the element's boundaries [43].

The finite element method has been proven to be valuable for material examinations, particularly in assessing the fatigue behaviour of steel specimens [4]. The FEM is a reliable tool to predict the fatigue life of the component as closely as possible to the actual scenario [44]. The fatigue testing matrix can be formulated based on the outcomes of fatigue modelling using the finite element method. The development of sophisticated models capable of tackling the previously discussed phenomena, along with the effective integration of these models into widely used finite element codes such as ABAQUS, ANSYS, and LS-DYNA, is essential for achieving a more precise assessment of the mechanistic-based structural integrity of reactors and other safety-critical components [43]. The significant complexities associated with cyclic plastic deformation mean that many current models struggle to accurately represent the cyclic plasticity behaviour observed in experiments. The cyclic plastic behaviour of metals presents significant complexity, necessitating a series of experiments to thoroughly investigate aspects such as the cyclic hardening or softening of the material and the progressive deformations (ratcheting) that arise from the plastic deformation occurring in each cycle.

### **1.7. Fatigue Failure**

Fatigue failure is commonly referred to as brittle failure, since global plasticity and necking are often minimal in numerous instances. The propagation of fatigue cracks involves plastic deformation in a small area surrounding the crack tip. There is a scenario in which certain small fatigue cracks merge and propagate together, often leaving behind a pattern of dark and light bands on the fracture surface.

When a metallic component is subjected to a loading condition, shear stress can arise in the parallel planes that tend to move relative to one another. The adjacent planes slide over each other within the grains, leading to slip plastic deformation. The surface grains exhibit the lowest strength, making them susceptible to slippage and plastic deformation, which subsequently leads to the formation of the microstructure [8].

In many cases, the appearance of fatigue cracks occurs through microcracking of the surface, reaching a length that can vary from 1% to 100% of the fracture surface, influenced by the type and intensity of load as well as the strength of the material [8].

Microcracks typically start in the plane subjected to the highest shear stress, although there are exceptions in cases of torsional and multiaxial loading [8]. Under uniaxial loading conditions, the slip occurs at an angle of  $45^\circ$ , corresponding to the orientation of the maximum shear stress plane [8].

Schijve [23] explains the crack initiation process as follows: when the stress amplitude is below the yield limit, a cyclic slip occurs at the microscopic level, involving only certain grains in the material. This process occurs on the surface, where the material experiences fewer constraints than in the internal regions of the component. Slip is irreversible as a result of the metal surface being covered by a layer of oxide after slip, along with the appearance of strain hardening. Microcracks form as slips accumulate in proximity, leading to crack growth under continued cyclic loading.

### **1.8. Previously Recorded Work on LCF**

The study by Meng et al. [45] looked at how temperature and strain rates affect the low-cycle fatigue behaviour of austenitic stainless steel. Facheris and Janssens [46] performed a set of tests on stainless steel 316 at room temperature and  $200^\circ\text{C}$  to see how strain amplitude and temperature affect low-cycle fatigue. Chen et al. [47] investigated how modified 9Cr-1Mo steels with 0.38% and 1.2% silicon behave under low-cycle fatigue at a temperature of  $450^\circ\text{C}$  [11].

Cao et al. [48] examined the low-cycle fatigue characteristics of additively manufactured 316 stainless steels, contrasting the findings with the fatigue characteristics of rolled 316 SS components. Branco R et al. [49] conducted fully reversed strain-controlled low-cycle fatigue experiments for strain amplitudes ranging from 0.3 to 0.1% strain on AISI 18Ni300 steel at room temperature. Wang X et al. [50] examined how hold time, strain amplitude, and temperature influence the fatigue life of P92 steel through a series of low-cycle fatigue experiments and forecasted the fatigue life for various experiments carried out.

G. Kang and Y. Liu [51] investigated low-cycle fatigue failure and ratchet failure on a tempered, heat-treated, and annealed 42CrMo steel sample under uniaxial cyclic loading. Similarly, Yang, X. [52] performed experiments on low carbon steel with tempered and quenched treatment to study the effect of mean strain on cyclic strain, low cycle fatigue and the mean stress effect of mean stress and stress amplitude for stress-controlled ratcheting failure. X. Zhang et al. [53] and Wang et al. [54] studied the effects of temperature on the softening behaviour of steel using an experimental low-cycle fatigue test at different temperatures. The American Iron and Steel Institute (AISI) examined the relationship between monotonic tensile properties and fatigue properties controlled by constant amplitude strain [11]. J-You and Miskiewicz [55] investigated the cyclic plasticity of metal using experimental and numerical methods. They used the Frederick-Armstrong-Chaboche combined nonlinear isotropic and kinematic hardening law [55]. Roessle, ML, and Fatemi, Ali [56] published the results of the research carried out by AISI, which estimated the strain life curve and the strain life fatigue properties.

Abarkan et al. [57] studied the cyclical behaviour of 316LN stainless steel. In their studies, they predicted the fatigue life of specimens exposed to several strain amplitudes at room temperature. They predicted the fatigue life using several numerical methods, including the approach based on total strain energy density, the maximum shear strain, and the Brown-Miller criteria. They also employed some analytical models, such as Langer's analytical equation and modified versions by Diercks [58], Jaske and O'Donnell [59], and Chopra [60]. The numerical simulations were performed on the finite element software ABAQUS. Tsutsumi et al. [61] did experiments and used finite element analysis with ABAQUS software on two samples made of SM490 and HT780 steel that had notches. The crack initiation was investigated using the fatigue subloading surface (fatigue SS) model, and crack propagation was studied as the sequence of crack initiations. S. Tsutsumi et al. [62] performed an experimental and numerical inspection on SM490B steel for fully reversed cyclic and monotonic loading. They kept forward a constitutive model to capture the softening behaviour of the metals. They tested the developed model by incorporating it into a numerical model using the ABAQUS subroutine, which replicated the experimental data. Fincato, R., et al. [63] investigated SM490, SM570, and F18B steels for stress-strain behaviour experimentally and numerically. The numerical investigation was performed using the ABAQUS software, and the material parameters required for the model were estimated and calibrated using experimental data.

Roy S et al. [44] predicted the low-cycle fatigue life of AISI316L stainless steel at room temperature. They conducted multiple strain-controlled low-cycle fatigue experimental tests for strain levels between 0.3% and 1% with a strain rate of 0.3%/sec. Additionally, they carried out a numerical investigation using finite element analysis, applying the Chaboche kinematic hardening model alongside isotropic hardening to forecast the fatigue life of the specimen. In their study, Yang, H. et al. [64] performed a strain-controlled constant-amplitude uniaxial tension-compression cyclic test to calibrate the Chaboche kinematic hardening parameters in steel. Zhang et al. [65] conducted an experimental study on the low-cycle fatigue characteristics of steel P92 at room temperature, alongside a numerical analysis that involved estimating and calibrating the isotropic and kinematic hardening parameters. Han, J. et al. [66] conducted a numerical implementation of the Chaboche kinematic hardening model through a user-defined material model. Hai, L. et al. [67] calibrated the parameters of the Chaboche model across various strain ranges on structural steel, having conducted the 171-test beforehand. Mohanty, S. et al. [68] determined the Chaboche kinematic hardening parameters for SS 316 through a numerical investigation, utilising the strain versus strain curve derived from experimental fatigue tests conducted at different temperatures and strain ranges. Santus et al. [69] introduced a procedure to estimate Chaboche kinematic parameters and developed the Chaboche isotropic kinematic hardening model by incorporating the Voce isotropic hardening equation with the Chaboche model. Shiva et al. [70] carried out an experiment and a numerical analysis on flat-on-flat contact of modified P91 steel, applying maximum cyclic stresses of 450 MPa, 500 MPa, and 550 MPa with a stress ratio of 0.3.

R. Hormozi et al. [71] conducted an experimental investigation of a fully reversed isothermal fatigue test for various strain ranges at 650°C on 316 steels, along with numerical analysis employing the isotropic and nonlinear kinematic hardening rule to replicate the behaviour of the experimental material until the stabilisation of the component. Ondrej S et al. [72] examined the low-cycle fatigue behaviour of AISI 316L austenitic steel through both experimental and numerical methodologies and subjected it to cyclic loading in a hollow cylindrical specimen that contained a pre-existing crack.

Zhu P et al. [73] proposed a hardening function and examined the factors that influence the hardening process. H. Mahbadi and M.R. Eslami [74] utilised the Prager and Armstrong-Frederick kinematic hardening models to explore the effects of cyclic loading. Li-Yan et al. [75] performed experimental and numerical research on BLY160 steel to study its cyclic softening and hardening behaviour. They formulated an elastoplastic constitutive mode based on the combined isotropic and kinematic hardening models. The formulated constitutive model was tested using it for the numerical simulation and compared with the experimental results. Chen et al. [76] carried out an experimental investigation to study the dependence of the steel strain range, followed by the numerical investigation using the ABAQUS UMAT platform. They kept forward a constitutive model to capture the cyclic softening phenomenon, and the accuracy of this model was validated by using it for the numerical simulation and comparing the numerical results with the experimental. Moeini G. et al. [77] conducted experimental and numerical investigations on the low-cycle fatigue behaviour of dual-phase steel. The stable hysteresis loop was simulated using micromechanical modelling techniques.

Wang et al. [78] prepared a finite element for the growth of fatigue cracks based on the theoretical background of the Gaussian process validated by the experimental results of the SCM435 material. Experiments were performed by M.A. Meggiolaro and Castro J.T.P. [79] on 724 specimens made of steel for the estimation of the Coffin-Manson model. Gardner, L. and Nethercot, D. [80] conducted a numerical study on the structural response of hollow stainless steel using finite element modelling. G. Dundulis et al. [4] kept forward a finite element model to study the low cyclic fatigue behaviour of P91 steel. To validate the finite element model and calibrate the material parameters, they performed a strain-controlled low-cycle fatigue test at 550°C. B. Das and A. Singh [81], Hyde et al. [82], Tanner et al. [83], and Saad et al. [84] also performed a numerical investigation on P91 steel to study the behaviour of the material and estimate the model parameters to determine the material for the simulation by referring to low-cycle fatigue. N. Shamsaei and S. SA McKelvey [85] utilised the Baumel–Seeger, Muralidharan–Manson and Roessle–Fatemi methods to estimate the fatigue life of steel based on general tensile properties under multiaxial loading conditions without using the fatigue experimental test data. A. Dutta et al. [86] performed a finite element simulation using ABAQUS software to study low-cycle fatigue in the elastic-plastic regime on AISI316L stainless steel. The required parameters were estimated from the uniaxial loading low-cycle fatigue experimental data at room temperature. R. Janulionis and G. Dundulis [87] studied the low-cycle

fatigue behaviour of the 9Cr-1Mo steel at 550°C. Their study included both experimental and numerical investigations. Strain-controlled low-cycle fatigue tests were performed, and finite element modelling was used for the numerical simulation.

Although significant efforts have been made to estimate and calibrate the material parameters, still the process of estimation of material parameters highly depends on the calibration of the parameters using experimental data. Further investigation is required regarding the procedure for estimating the kinematic hardening parameters to reduce the complexity and time required for the estimation and calibration of these parameters. Such work is essential to tackle the challenges encountered while applying the estimated hardening parameters in various FE simulation software. In addition, numerical methods continue to face certain challenges in accurately forecasting behaviour during the initial cycles.

## **1.9. Chapter Conclusion**

This chapter presents a comprehensive review of the fatigue phenomenon, fatigue failure, and previous work done on the topics related to this dissertation. The following list highlights the key insights from this chapter:

Researchers have extensively studied the fatigue life of austenitic stainless steel, paying particular attention to its low-cycle fatigue behaviour. Researchers have investigated the effects of temperature, strain rate, strain amplitude, specimen size, and design on the fatigue behaviour of the components under cyclic loading. Researchers have observed low-cycle fatigue failures in AISI 304L, AISI 316L, and AISI 316LN stainless steels, as well as AISI 18Ni300 steel, P91, and P92 steel.

Theoretical, analytical, and finite element simulation methods are found in the literature used for fatigue analysis. The finite element method is the most widely used numerical method for fatigue analysis. ABAQUS, ABAQUS UMAT, Cast3M, and Ansys are employed as software for the FE simulation. The Chaboche kinematic hardening model has been used to predict the low-cycle fatigue life of stainless steel, focusing on its elastoplastic response. Accurate determination of hardening parameters is crucial for capturing cyclic behaviours and improving simulation precision. Researchers have used various methods to study the fatigue life of various materials, including AISI 316L austenitic steel, dual-phase steel, P92 and P91 steel.

Despite these extensive studies, more research is needed to accurately estimate the fatigue life using numerical simulation tools of these materials and address challenges in estimating hardening parameters and forecasting stress-strain behaviour during fatigue life. Estimating and calibrating the kinematic hardening parameters remains a time-consuming and complex task, often relying on experimental data to validate the simulation results. The low-cycle fatigue experiment is expensive, and it is difficult to maintain environmental conditions. Simplifying and improving the process of estimating the kinematic hardening parameters is important to reduce estimation errors, nearly eliminate the calibration process, and enable the estimation of approximate fatigue life without relying on experimental data.

The analysis of research publications assessing the outstanding issues mentioned in the review allowed to identify the aims and objectives of the dissertation.

The aim of this research is to analyse and develop numerical simulation methodology for the analysis of the low-cycle fatigue behaviour of the steel to estimate the approximate fatigue life of the components operating under harsh environments by simplifying the process of the estimation of kinematic hardening parameters to capture the elastoplastic behaviour of the steel during the numerical simulation. The following objectives are set to achieve the aim.

1. To develop a comprehensive experimental matrix for performing the low-cycle fatigue (LCF) testing on AISI 316L austenitic stainless steel under strain- and stress- controlled regime, exposed to both constant and variable amplitude loading, for generating high quality data of cyclic stress-strain response, fatigue life to develop and validate the numerical simulation model.
2. To develop finite element model capable of capturing the cyclic elasto-plastic and hardening/softening behaviour of austenitic stainless steel using constitutive rules for the kinematic hardening and calibrating the model parameters with experimental data.
3. To develop a simplified and reproducible methodology for the determination of the hardening and softening parameters of AISI 316L stainless steel for minimizing the requirement of experiment results while maintaining the accuracy and reliability of the estimated parameters.
4. To perform numerical simulations of low-cycle fatigue and validate the results of the developed models by comparing the simulation results with corresponding experimental results.

## 2. EXPERIMENTAL METHODOLOGY

The experimental study of the low-cycle fatigue of austenitic stainless steel is still relevant because of its ability to showcase the fatigue behaviour of the material in actual working conditions under cyclic loading. The experimental investigation still plays a vital role in the preparation of the safety guidelines for the structures as well as the validation of the numerical models.

The low-cycle fatigue experiments are performed on AISI316L stainless steel, which is used in the nuclear power plant. Reliable management of the structure and components working under harsh environment has a high priority for safe operation of these structures. The experimental testing of these structures for safe operation is crucial. However, in some cases, conducting experimental testing under real operating conditions is very expensive. It should be noted that the determination of fatigue curves is expensive, time-consuming, and difficult to implement in the experiment, especially in a reactor environment (high or low temperatures, acid or alkaline environments, etc.). Usually, the data obtained from laboratory fatigue tests do not accurately reflect in-plant observations.

Temperature variations associated with start-ups and shutdowns, power adjustments, thermal stratification and striping are responsible for thermomechanical fatigue. Significant amount of research has been performed on the fatigue life of austenitic stainless steels in air environment; however, numerous challenges still exist regarding in the field of environmentally assisted fatigue (EAF) in LWR environments. The fatigue life in of components in such environments is now clearly understood to be reduced compared to that in air, influenced particularly by factors such as temperature, strain rate, and water chemistry. According this the testing of the specimens in the operation environment is main task in of the steel tests for the prognosis of the lifetime of the equipment. The test in the air condition is only a initial estimation of the steel parameters in low cyclic fatigue. The equipment used for testing of the specimen in operation environment, specialy at high temperature, pressure environment such as in PWR is very expensive. The numerical simulation methods are useful to evaluate the strength of the components at different loadings. Therefore, the PWR (pressurised water reactor) environment was selected for one test to evaluate the material behaviour under that condition and compare it to the tests in air. KTU do not have specialized testing equipment and can perform tests only in air environment. The FE models were prepared for the modeling of LCF behavior in the PWR operation environment on hollow specimen and these models were validated by experimental tests performed at the facility of EDF (Électricité de France), as per the description by Spatig, P. et al. [7].

As it is mentioned earlier, the determination of fatigue curves is expensive and time-consuming; due to the requirement to analyse low-cycle fatigue behaviour in detail, AISI 316L stainless steel was selected. In this work, AISI 304L stainless steel is also examined, but only under air conditions.

This section lists some of the standards available for the experimental design, specimen design, and calibration of the testing equipment related to the topic of this

dissertation. This chapter also consists of the description of the specimen design and the experiment matrix.

## **2.1. Standards for Experimental Analysis**

For a proper assessment of fatigue behaviour using an experimental method, it is important to refer to the standards published for this purpose. There are several standards available for the different fatigue assessments.

Some of the standards commonly used for low-cycle fatigue investigations include ASME Section III, Class 1 and the ASME III fatigue curve [15]; ISO/DIS 12106, which specifies axial strain-controlled fatigue testing of metallic materials [88]; ISO 7500-1, which addresses the calibration and verification of force measurement systems in tension/compression testing machines [89]; ISO 9513-2012, covering calibration of extensometer systems [90]; ISO 23788-2013, which specifies verification of fatigue testing machine alignment [91]; ISO 1099-2017, describing axial force-controlled fatigue testing [92]; ISO 4965-1:2012, concerning dynamic force calibration for uniaxial fatigue testing systems [93]; ASTM E606/E606M, the standard practice for strain-controlled fatigue testing [94]; ASTM E1012, which addresses specimen alignment under tensile loading [95]; and corresponding national standards such as AFNOR A03-403 [96], BS 7270 [97], JIS Z 2279 [98], ISO 11782-1 for corrosion fatigue testing [99], and EN 10002-1 [100] and EN 10002-5 [101] for tensile testing at ambient and elevated temperatures, respectively.

The standards should be referred to for the elimination of errors in the experiment process and collection of the results. In this research, ASTM E 606/E606M [94], ASTM E 1012 [95], ISO 11782-1 [99], EN 10002-1 [100], and EN 10002-5 [101] standards are used for the preparation and performing the low cycle fatigue experiments.

## **2.2. Austenitic Steel**

Austenitic stainless steels are extensively used as structural materials in light water reactor (LWR) environments where high temperature, irradiation and complex thermomechanical loading conditions exist [7]. Austenitic stainless steel has shown satisfactory performance in strain hardening, ductility, and structural overstrength [90]. Stainless steels have an extensive application across various industrial components, covering the energy sector to biomedical uses. Understanding the behaviour of the cyclic plasticity of the material is crucial, particularly with respect to the latter property, especially within the low cycle fatigue regime (LCF) [102]. Table 3., presents the chemical composition of AISI 304L and AISI 316L stainless steel.

**Table 3.** Chemical composition of AISI 304L and AISI 316L stainless steel (wt%) [103]

	<b>C</b>	<b>Si</b>	<b>Mn</b>	<b>P</b>	<b>S</b>	<b>N</b>	<b>Cr</b>	<b>Mo</b>	<b>Cu</b>	<b>Ni</b>	<b>Fe</b>
AISI 304L	0.029	0.75	1.86	0.045	0.03	0.1	18	0.04	0.02	10	69.126
AISI 316L	0.026	0.42	1.81	0.033	0.004	0.05	16.96	2.43	0.03	12	66.237

AISI 304L and AISI 316L are the type of low carbon stainless steel. The ‘L’ represents the low carbon content of the alloy, which is below 0.03%. These types of steels are used to avoid the corrosion problem. AISI 316L contains additional amount of Mo (molybdenum) as compared to AISI 304L, due to which 316L is more corrosion resistant [103].

Type 316 austenitic stainless steel is extensively utilised in different types of nuclear reactors, encompassing existing nuclear power plants and next-generation advanced reactor concepts, such as sodium-cooled fast reactors, molten salt reactors, and gas-cooled high-temperature reactors.

Type 316 stainless steel can be engineered to function effectively in high-temperature environments characterised by significant temperature gradients, such as those found in aircraft gas turbine engines or hot-section combustor liners. Materials experience cyclic strains generated through thermal and/or mechanical processes under the influence of these constant and cyclic temperature-strain conditions; isothermal and thermomechanical fatigue damages arise, resulting in the initiation of cracking and subsequent crack growth. In addition to low-cycle fatigue (LCF) damage resulting from start-up and shutdown cycles, high-temperature components also face time-dependent creep damage as a consequence of their regular operation at elevated temperatures during service [71].

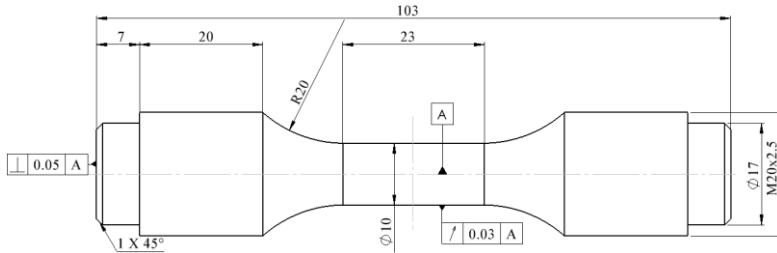
### 2.3. Specimen Design

The test specimens were designed according to ASTM E606/E606M [94] standard practice for strain-controlled fatigue testing requirements and recommendations. Several specimens were prepared for each experiment scheme. The experiments were performed for solid elements, hollow specimens, and notch specimens.

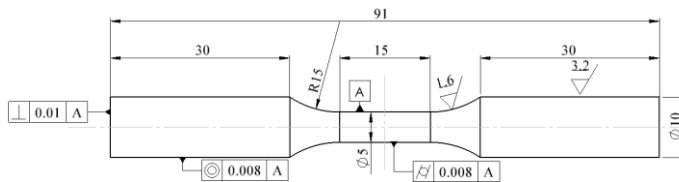
Cylindrical test specimens for low-cycle fatigue experiments of stainless steel AISI 304L and 316L were designed according to the standard [94]. Detailed specimen geometries for all experiments performed are shown in Figure 4 to Figure 8.

Figure 4 shows the specimen drawing used in the low-cycle fatigue test at 300°C for a strain amplitude of 0.3% and 0.6%. The specimen was manufactured with a solid bar of AISI 304L stainless steel. Another two experiments were performed on solid specimens made of AISI316L stainless steel. The experiments were carried out for the strain amplitude of 0.18% at 20°C and 0.6% at 300°C. The drawing of the solid specimen of AISI316L SS is presented in Figure 5. The effects of the change in strain amplitude and change in temperature on the four experiments of LCF behaviour of

the AISI 316L stainless steel in a solid specimen were performed in air. In addition to the solid specimen, LCF testing was also performed on a hollow specimen of AISI 316L SS in a PWR environment. Figure 6 and Figure 7 present a drawing of the solid and hollow specimens for these tests. Figure. 8 shows the drawing of the notched specimen used for the LCF test.



**Fig. 4.** Solid specimen of AISI 304L tested under 0.3 and 0.6% strain amplitude



**Fig. 5.** Solid specimen of AISI 316L tested at 20 °C and 300 °C for 0.18 and 0.6% strain amplitude

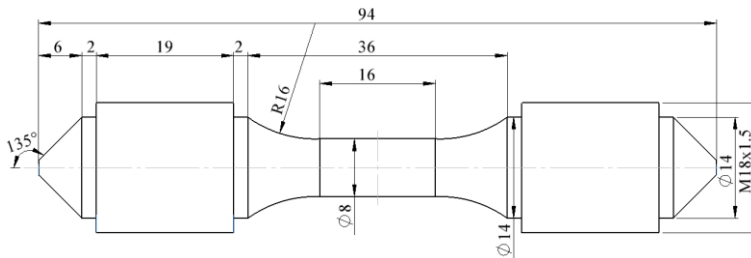


**Fig. 6.** Solid specimen of AISI 316L for the LCF test in air at 20 °C and 300 °C for 0.5 and 1 % strain amplitude (specimen used in EDF laboratory test)

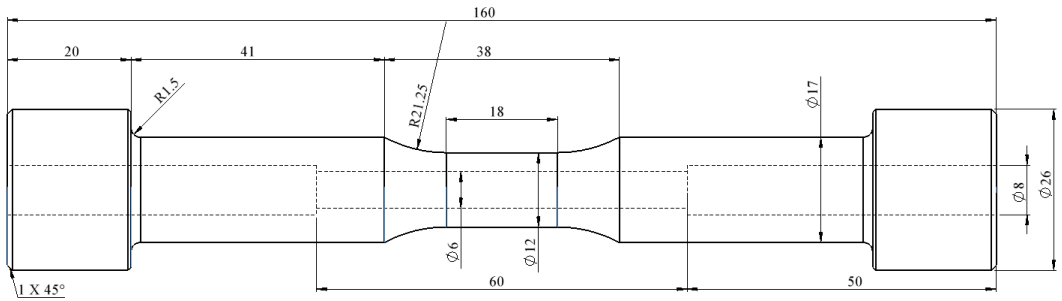


**Fig. 7.** Hollow specimen of AISI 316L for 0.3% strain amplitude LCF test in a PWR environment at 300°C (specimen used in EDF laboratory test)

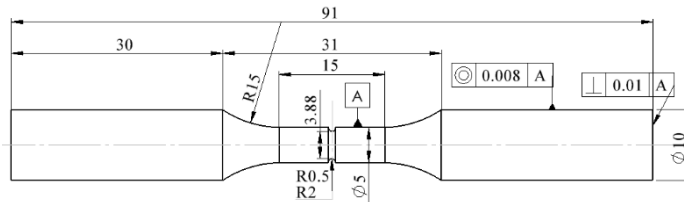


**Fig. 8.** Notched specimen of AISI 316L, notch radius 0.5 and 2 mm at 300°C for stress-controlled LCF test

Geometrical discontinuities such as welds, bolt holes, threads, etc. are generally treated as notches. These features create stress concentrations that may decrease the fatigue life of the component and are often the site for nucleation and growth of fatigue cracks in components subject to cyclic loading. Stress concentration areas such as notches are common in nuclear plant components and have to be considered in fatigue life analyses. Therefore, the testing of notched specimens has been developed and performed to evaluate the effect of stress concentration area strain gradient for low cyclic fatigue on AISI316L stainless steel.

## 2.4. Experimental Setup

The low-cycle fatigue tests were performed on several types of samples: solid and hollow specimens with smooth surface finishes and solid ones with notches. The tests were conducted at both ambient and elevated temperatures, in air and pressurized water reactor (PWR) environments, using strain-controlled and stress-controlled (notched specimens) testing methods. Table 4 and Table 5 present the experiment schemes.

The stress/force-controlled tests were performed according to EN 10002-1 [100] at ambient temperature and EN 10002-5 [101] at 300°C.

The strain controlled low cycle fatigue tests at ambient and elevated temperatures were performed in accordance with ASTM 606 [94]. Constant strain was applied in triangular waveform at strain rate of 0.4%/s.

Specimen temperature during the fatigue testing at elevated temperature was maintained at  $300\pm 3^{\circ}\text{C}$  throughout duration of test. The maximum allowed bending was 1% at 5 kN and less at larger loads. BS7270:2006 [97] was referred for the detection the number of cycles to failure of the specimen.

For the experimental low-cycle fatigue testing, during the specimen fixation, complete angularity and concentricity adjustments and tests were performed that comply with ASTM E1012 [104].

**Table 4.** Experiment matrix for non-notch specimens

Test No.	1	2	3	4	5	6	7	8	9
Specimen Type	Solid without notch								Hollow
Material	AISI304L		AISI316L						
Test Type	Strain Controlled								
Strain Amp. (%)	0.3	0.6	0.18	0.6	0.5		1		0.3
Temp. ( $^{\circ}\text{C}$ )	300		20	300	20	300	20	300	300
Loading Type	Constant amplitude alternate loading with zero mean stress. $R=-1$								
Environment	Air								PWR

The low-cycle fatigue test in the solid stainless steel AISI 304L sample was carried out on the Instron 8801 servo hydraulic test machine with a dynamic load cell of  $\pm 100$  kN. Reverse stress pull rods were employed to perform the LCF test at high temperature. To mount the specimen, a threaded specimen adapter was used. The concentricity and angularity of the specimen were adjusted using a threaded alignment cell, AignPRO. The K-type thermocouples were mounted on the specimen to measure the temperature. The gauge section throughout the experiment was maintained constant within the desired variation of 1 to  $2^{\circ}\text{C}$ . The Instron 2632 series high-temperature extensometer was used to measure the strain during the experimental testing [43].

**Table 5.** Experiment matrix for the notch specimen

<b>Test No.</b>	10	11
<b>Specimen Type</b>	Solid with notch	
<b>Material</b>	AISI316L	
<b>Notch radius (mm)</b>	0.5	2
<b>Test Type</b>	Stress controlled	
<b>Maximum applied force (N)</b>	2447	8908
<b>Temp. (°C)</b>	300	
<b>Loading Type</b>	Variable amplitude (Stepped Loading) alternate loading with zero mean stress. R=-1	Constant amplitude alternate loading with zero mean stress. R=-1
<b>Environment</b>	Air	

Experiments 1-9 were performed under a strain-controlled scheme. And for the 10-11 experiments, they were performed under a stress-controlled scheme.

The electromechanical tension-torsion machine INSTRON E10000 (Figure 9) was used for experimental testing, with a maximum tensile force of 10 kN and a torsion capacity of 100 Nm. Section 2.3 shows detailed specimen geometry. To ensure proper specimen centricity in the testing machine, the bottom grip was mounted through the alignment flange using four adjustment screws. When adjusting, specimen centricity was determined by measuring deformations of the testing machine's stud using strain gauges bonded to the upper stud of the tensile machine. Signals from strain gauges were connected to a computer via a National Instruments data acquisition system, NI CDAQ-9188, and post-processed in MATLAB.



**Fig. 9.** INSTRON ElectroPuls™ E10000

In a thermal chamber, tests were carried out at 300°C. Strains on the specimen gauge area were measured with a high-temperature external extensometer, 7642-

010M-025SM-TD from Epsilon, mounted on the specimen. To capture fatigue cracks and measure strains on the specimen, a 3D Digital Image Correlation (DIC) system with two Basler acA4112-20 $\mu$ m cameras from Correlated Solutions was used through the thermal chamber window. Specimen images captured by DIC cameras were post-processed in VIC-3D. The software VIC-3D was used to set the speckle pattern subset size to 1.4 mm (77 px) and the step size between the subset centres to 0.28 mm (15 px), yielding an uncertainty interval of 0.04 px for the DIC measurements.

## **2.5. Chapter Conclusion**

Experimental investigation was performed on austenitic stainless steel for the low-cycle fatigue behaviour at room temperature and elevated temperature on solid, hollow and notched specimens under strain-controlled and stress-controlled loading conditions in air and pressurised water reactor environments.

In this chapter, the experimental matrix, material selection, specimen design and experimental setup are explained.

The experimental specimens were designed as per the standard E606-92: 8 solid specimens, 1 hollow specimen, and 2 specimens with notches of different notch radii. And the experiments were performed according to the ASTM E 606 standard using the Instron E10000 fatigue testing machine.

### 3. NUMERICAL SIMULATION METHODOLOGY

Numerical simulation has become a core tool in recent times for the low-cycle fatigue analysis of austenitic stainless steel due to its reliability, cost-effectiveness, and possibility for in-depth analysis. Also, the possibility to be able to predict fatigue life under realistic and complex operating conditions. The numerical simulation of components exposed to low-cycle fatigue failure, the cyclic elastoplastic behaviour of the material should be modelled until stabilisation, which generally occurs at half the number of cycles to failure [105]. In the current research, numerical simulation is performed to study the elasto-plastic behaviour of the austenitic stainless steel during the low-cycle fatigue life of the component. In this chapter the finite element model prepared, applied loading conditions, boundary conditions and material modelling are explained.

#### 3.1. Finite Element Modelling

As mentioned earlier in Section 2.2, for this investigation, several types of specimens were investigated, such as solid, hollow, and with a notch. The specimens used for the experiments were axisymmetric. Two types of specimens were modelled, one full specimen was modeled for the numerical simulation, as shown in Figure 10, and due to the axisymmetry of the specimen, one more model of the same specimen was developed representing one-quarter ( $1/4^{th}$ ) portion of the cross-sectional area of the specimen's gauge length (Figure. 11).

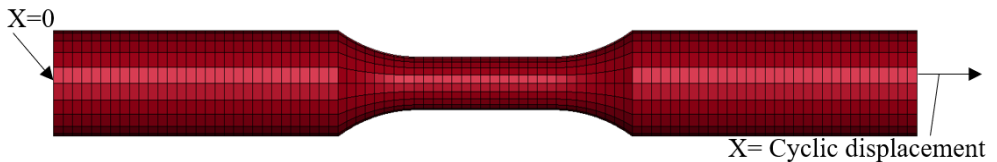


**Fig. 10.** Full specimen FE model with applied boundary conditions

The strain-controlled low-cycle fatigue tests were performed on solid and hollow specimens with a smooth surface finish. To replicate the strain-controlled motion of the experimental testing displacement, the strain-controlled motion was applied to the front face of the specimen model according to the length of the model. To avoid unwanted motions of the element, restrictions were applied to the model. The applied boundary conditions are shown in Figure 11.

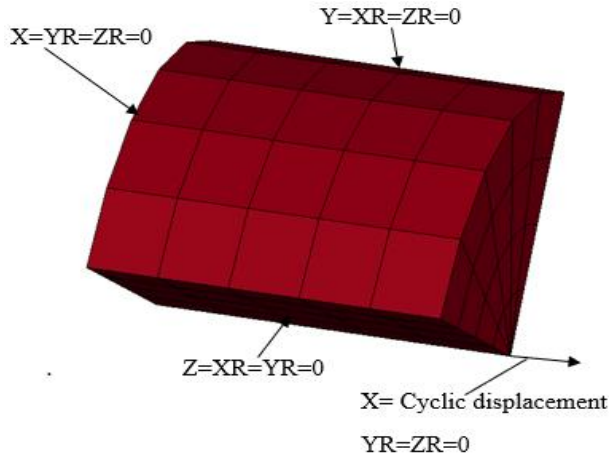


**Fig. 11.** Applied boundary conditions to reduced FE model

Simulations on AISI 304L stainless steel for 0.3% and 0.6% strain amplitude low-cycle fatigue were performed on ANSYS Workbench. The specimen was modelled using ANSYS\_SOLID185 elements; this element is 8-node with three degrees of freedom for each node. The models for AISI 316L stainless steel for 0.18%, 0.6%, 0.5%, and 1% strain amplitude were prepared in LS-DYNA software. Constant stress 8-node hexahedron elements were used to model solid (Figure 11) and hollow specimens (Figure 12). The inside surface of the hollow specimen was exposed to internal pressure to replicate the experimental environment.

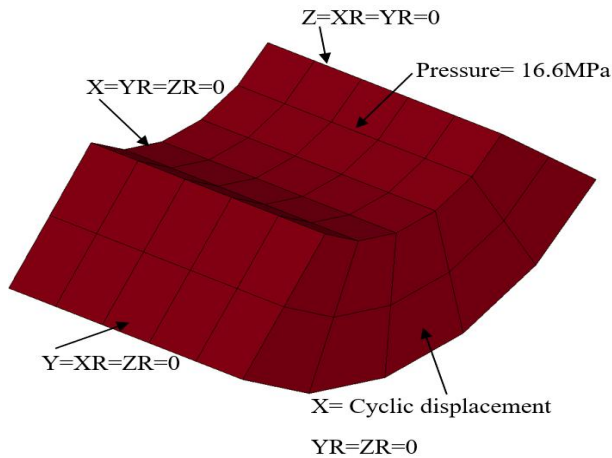


**Fig. 12.** Meshed FE model for a hollow specimen

The simulation model for the notch specimens was prepared with 2D elements. The specimen was modelled using a 4-node, quadrilateral shell element with the Belytschko-Tsay formulation. Figure 13 presents the finite element model and the boundary conditions applied to it.

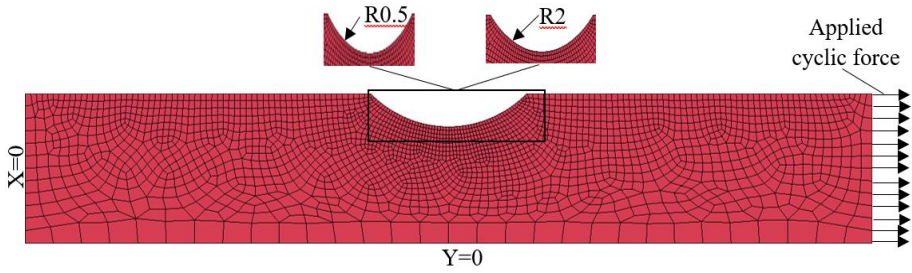


**Fig. 13.** Meshed FE model with applied boundary conditions for the notched specimen

A fine mesh was used to model the notch area to capture the stress concentration occurring there. Also, unlike other models, the full gauge length of the specimen was modelled. There were two different models, one with a 0.5 mm notch radius and one with a 2 mm notch radius. The left end was fixed for the x-translational motions, loading was applied on the right end of the specimen model in the x-direction, and for the bottom side, the y-direction motion was fixed.

### 3.2. Specimen Loading

The fully reversed loading was applied to the specimen along the axial direction with the triangular waveform. Figure 14 represents the relative loading applied to the FE model for the numerical simulation. The first cycle starts at point 0 (Figure 14) when the specimen is at rest. For the first cycle, it is divided into three parts: the first part point (0-1) is the half portion of the tension part, which is followed by the compression cycle point (1 to -1) and again the tension part from point (-1 to 1). This sequence completes the first cycle, and the second cycle follows the point (1, -1, 1) and so on until the full simulation time.

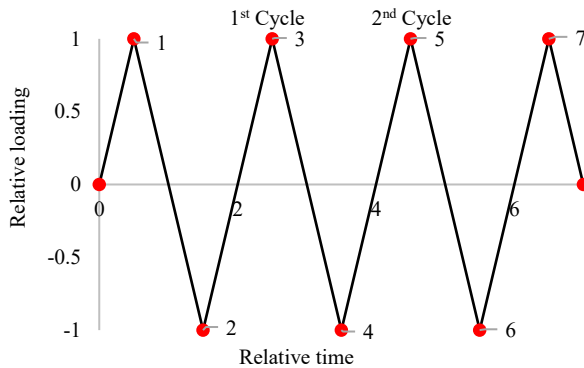


**Fig. 14.** Relative strain applied for the FE model in the case of strain-controlled scheme

In the strain-controlled low-cycle fatigue test scheme, the strain amplitudes were  $\pm 0.18\%$ ,  $\pm 0.3\%$ ,  $\pm 0.5\%$ ,  $\pm 0.6\%$  and  $\pm 1\%$ . Therefore, 1 and -1 represent the strain

amplitude in the positive and negative directions, respectively. To replicate the strain-controlled motion as per experiments, displacement is applied to the specimen during the simulation in correspondence to the strain amplitude (e.g., for the  $\pm 1\%$  strain amplitude and 10 mm length of the specimen model, a displacement amplitude of  $\pm 0.1$  mm is applied to the model).

In the case of the stress-controlled low cycle fatigue test, the loading was applied similarly to the strain-controlled scheme, that is, a fully reversed triangular waveform (Figure 14). There were two different specimens according to the radius of the notch. The notched specimen was tested under a stress-controlled LCF testing scheme. Figure 15 and Figure 16, shows the force applied during the LCF experimental testing.

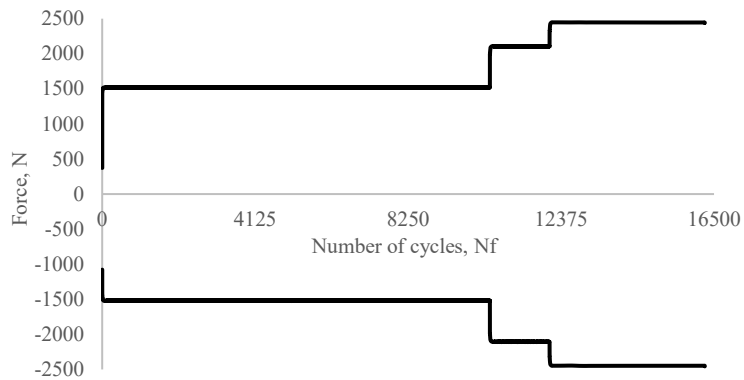


**Fig. 15.** Loading applied for the FE model for the notch specimen with  $r=0.5\text{mm}$

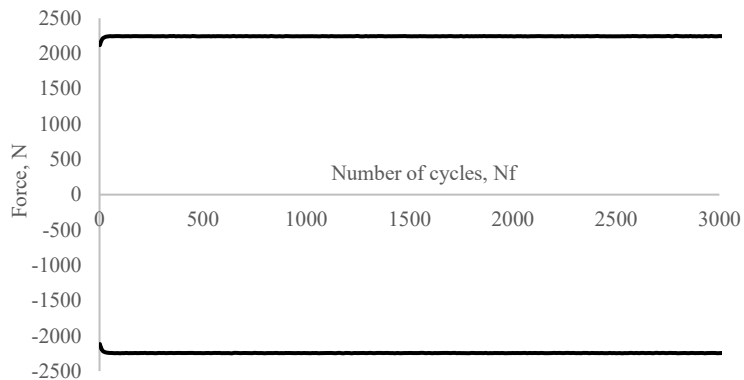


**Fig. 16.** Loading applied for the FE model for the notch specimen with  $r=2\text{mm}$

Two notch radius of 0.5 mm and 2 mm were chosen with the help of finite element elastic calculations and are supposed to be compared to uniaxial standard fatigue tests, choice was made to use comparable strain amplitude.

Finite elements elastoplastic calculations were thus performed to evaluate the loads needed to achieve strain amplitudes of 0.3% and 0.6% at the notch tip. Indeed,

load control was chosen for the fatigue testing to get a common control among all labs and ease the control on PWR rigs (INCEFA-Scale project).

The force applied during the experimental testing was selected based on the target strain at the notch tip of the specimen. For the notched radius of 0.5 mm, the loading was applied in three steps (Figure 15): loading with a maximum force of 1520 N up to 10445 cycles, then the loading force is increased up to 2100 N, and finally, after a total of 12065 cycles, the loading force is 2445 N. A specimen with a notch of radius  $r = 2$  mm was loaded with a single step loading of 2245 N (Figure 16) load until failure.

### 3.3. Material Model

For proper estimation of the low-cycle fatigue life of the component, it is important to model the material for cyclic plasticity. Plasticity is an irreversible strain that occurs when stress reaches a certain level [106-110]. Assuming that plastic strains develop independently of time, various theories exist to characterise the material's response. Plasticity theory identifies three primary components: yield criterion, flow rule, and material (hardening) models [106-110]. In the current research, kinematic hardening is employed along with isotropic hardening to model the material in finite element modelling for the simulation. Table 6 presents the mechanical properties of AISI 304L and 316L stainless steel at 20 and 300°C. Table 7 consists of the initial yield stress. The initial yield stress was estimated from the 1<sup>st</sup> cycle stress versus strain curve of the experimental results.

**Table 6.** Mechanical properties of stainless steel [111-117]

Quantity	Symbol	Units	Values			
Material			AISI304L		AISI316L	
Temperature	$T$	°C	20	300	20	300
Density	$\rho$	Kg/m <sup>3</sup>	7930		7980	
Young's Modulus	$E$	GPa	193	175	193	180
Yield Stress	$\sigma_y$	MPa	200	135	205	149
Ultimate Tensile Strength	$\sigma_{uts}$	MPa	500	380	550	400
Elongation	EL	%	45	37	40	35
Poisson's ratio	$\nu$	-	0.28		0.26	

**Table 7.** Initial yield stress estimated using the first experimental result cycle

Material	Type of specimen	Quantity	Strain Amplitude	Temperature	Initial Yield Stress	
		Symbol	$\Delta\varepsilon$	$T$	$\sigma_{iys}$	
		Units	%	$^{\circ}\text{C}$	MPa	
AISI304L	Solid	Values	0.3	300	79	
			0.6		65	
AISI316L			0.18	20	133	
			0.6	300	68	
			0.5	20	105	
				300	94	
			1	20	120	
				300	91	
			Hollow	0.3	300	133
			Notched, r=0.5 mm	-		76
Notched, r=2 mm	-	37				

To determine the yield stress from the experimental results stress-strain curve, 0.2% offset method was used. The yield point is considered where the curve deviates from the elastic region (i.e. from linear to non-linear). Figure 17 shows the 0.2% offset method for determining the yield stress. This method is widely used because the transition of the curve from elastic to non-elastic region is not always at visible or well-defined point [118].

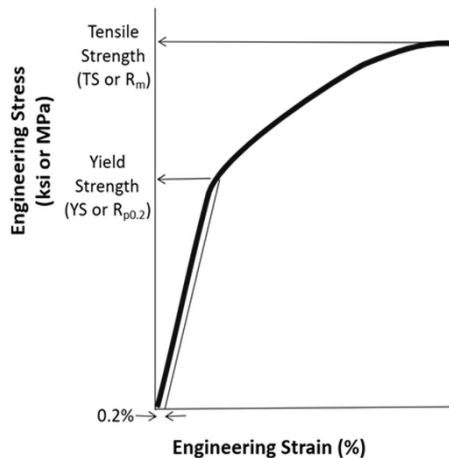


**Fig. 17.** Determination of yield stress by parallel line to the elastic region of curve with 0.2% strain offset [118]

In the 0.2% strain offset method, a line parallel to the elastic region of the curve is drawn at the offset of 0.2% of strain. The intersection point of this line and the stress is defined as the yield stress (Figure 17) [118].

### 3.4. Kinematic Hardening

Experimental observations of metals subjected to cyclic loading indicate that the centre of the yield surface shifts in the direction of the plastic flow, illustrating the Bauschinger effect [110]. A kinematic model effectively encapsulates the described effect, as it posits that during progressive yielding, the yield surface shifts within the stress space while preserving a consistent size [106-110].

In recent years, numerous material models have been developed to enhance our understanding of the cyclic plasticity behaviour of materials subjected to various loading conditions. Shit et al. [119] put forward a cyclic plasticity model to observe the effect of back stress and movement of the plastic strain centre in the plastic strain surface. Chaboche introduced a novel kinematic hardening model that categorised a stabilised stress-strain hysteresis loop into three distinct components [81,120]. Initially, there is the initiation of the yield, followed by a transient nonlinear phase, and ultimately the high-strain segment [81]. The Chaboche-type models [121-123] are widely used in engineering calculations and are incorporated into various commercial finite element software. The Chaboche-type models are based on a nonlinear kinematic hardening framework. The Chaboche-type model in its original form effectively captures plasticity under monotonic loading and the stable cyclic hardening behaviour of reactor materials; it may fall short in accurately modelling non-stable cyclic hardening and/or softening [23]. A more thorough understanding of the cyclic plasticity of metals is essential prior to the development of a reliable plasticity model for practical use, including the assessment of the stress-strain state and fatigue life of reactor components.

The complexities associated with cyclic plastic deformation result in many existing models having limited abilities to accurately represent the cyclic plasticity behaviour observed in experiments. The cyclic plastic behaviour of metals exhibits complexities, necessitating a series of experiments to thoroughly investigate aspects such as the cyclic hardening or softening of the material and the progressive deformations (ratcheting) that arise from the plastic deformation occurring with each cycle.

Equation 15 shows the model proposed by Chaboche, J.L. and Rousselier, G. (1983) [108] without time-recovery effects.

$$\sigma = \chi + (R + k + \sigma_v)sgn(\sigma - \chi) ; \quad (15)$$

This model has kinematic hardening parameters  $a_1$ ,  $a_2$ ,  $C_1$ , and  $C_2$ ; isotropic hardening parameters 'Q' and 'b'; viscous parameters 'Z' and 'n'; and the initial size of the surface of the yield 'k' [91].

Chaboche et al. (1979) [125] and Chaboche (1986) [121] proposed a new kinematic hardening rule. The model is shown in equation (16).

$$d\alpha_i = \frac{2}{3}C_i d\varepsilon^p - \Upsilon_i \alpha_i dp ; \quad (16)$$

here:

$C, \Upsilon$  are the kinematic hardening modulus and exponent respectively.  
 $dp$  is the accumulated plastic strain.

$$dp = \left( \frac{2}{3} d\varepsilon^p : \frac{2}{3} d\varepsilon^p \right)^{1/2} ; \quad (17)$$

We get equations (18-19) by mathematically solving equation (16)

$$\alpha_{xp} = \left[ \frac{2}{3} \frac{C_i}{\Upsilon_i} + \left( \alpha_{ixn} - \frac{2}{3} \frac{C_i}{\Upsilon_i} \right) e^{(-\Upsilon_i \Delta \varepsilon_x^p)} \right], d\varepsilon_x^p \geq 0 ; \quad (18)$$

$$\alpha_{xp} = \left[ -\frac{2}{3} \frac{C_i}{\Upsilon_i} + \left( \alpha_{ixn} + \frac{2}{3} \frac{C_i}{\Upsilon_i} \right) e^{(\Upsilon_i \Delta \varepsilon_x^p)} \right], d\varepsilon_x^p < 0 ; \quad (19)$$

$$\alpha_{xp} = \frac{2}{3} (\sigma_x - \sigma_0), d\varepsilon_x^p \geq 0 ; \quad (20)$$

$$\alpha_{xn} = \frac{2}{3} (\sigma_x + \sigma_0), d\varepsilon_x^p < 0 ; \quad (21)$$

here:

$\alpha_{ip}$ : Maximum value of back stress in tension or compression loading,  
 $\alpha_{in}$ : Minimum value of back stress in tension or compression loading.

Simulations of 0.3% and 0.6% strain amplitudes on AISI 304L stainless steel were performed using ANSYS Workbench. The ANSYS Workbench has a predefined Chaboche kinematic hardening model in it. Equations 18-21 were used to estimate the Chaboche kinematic hardening parameters for the 0.3% and 0.6% strain amplitudes at 300°C in the numerical simulations of AISI 304L stainless steel specimens.

The material parameters used to model the AISI 304L stainless steel in the ANSYS Workbench are presented in Table 6 and Table 7. The kinematic hardening parameters for the strain amplitudes of 0.3% and 0.6% at 300°C were estimated using the second half of the 1000<sup>th</sup> cycle for both models. Table 8 presents the components of kinematic parameters.

**Table 8.** Parameters for the Chaboche model estimated for the Ansys model

$\varepsilon_a$ (%)	$C_1$ (MPa)	$\Upsilon_1$	$C_2$ (MPa)	$\Upsilon_2$	$C_3$ (MPa)	$\Upsilon_3$
0.3	15482.86	2427.214	16950.62	2135.42	61446.98	268.889
0.6	15482.86	575.58	16950.62	1675.4	61446.98	679.35

The Armstrong-Frederick plasticity model was developed by incorporating a dynamic recovery term into the linear hardening rule established by Prager [126]. The

Armstrong-Frederick-type models are increasingly recognised for their strength in handling both proportional and non-proportional loads [120, 127]. Subsequently, the Armstrong-Frederick concept was expanded to accommodate more intricate loading scenarios, enhance the accuracy of the model, and effectively capture phenomena such as the decay of the ratcheting rate [80, 128, 129].

Armstrong and Frederick introduced a model that incorporates a nonlinear kinematic hardening term [130]. A recovery term was incorporated into the Prager linear kinematic hardening rule [126], which is recognised as one of the simplest models available. This term included the memory-fading effect associated with the strain path. The model exhibited an overestimation of ratcheting strain [131] and incorporated a limited set of material constants to improve the precision of ratcheting predictions [132].

As mentioned in Section 3.2.1, the numerical simulations for AISI 316L stainless steel strain amplitudes of 0.18%, 0.6%, 0.5%, and 1% were prepared in LS-DYNA software. LS-DYNA has a predefined material model that combines isotropic and kinematic hardening, named MAT\_153\_DAMAGE\_3. This material model defines kinematic hardening, which is defined using the Armstrong-Frederick kinematic hardening model.

$$\dot{\alpha}_j = \frac{2}{3} C_j \dot{\epsilon}^{pl} - \gamma_j \alpha_j \dot{\bar{\epsilon}}^{pl}; \quad (22)$$

here:

$C$  : Coefficient of Kinematic Hardening (MPa).

$\gamma$  : Exponent for Kinematic Hardening

$\dot{\epsilon}^{pl}$  : Plastic strain

$\dot{\bar{\epsilon}}^{pl}$  : Accumulated Plastic Deformation

$\alpha_j$  : Back stress

The Armstrong–Frederick KH model in the LS-DYNA ‘MAT\_153\_DAMAGE\_3’ material model is defined according to equation (22).

$$\alpha_{max} = \sum_{x=1}^3 \left[ \frac{2}{3} C_x \dot{\epsilon}^{pl} - \gamma_x \alpha_x \dot{\bar{\epsilon}}^{pl} \right]; \quad (23)$$

here:

$\alpha_{max}$  : Maximum cycle stress (MPa).

The kinematic hardening parameters were estimated according to equation 23. The KH parameters were estimated from the stabilised cycles of each experiment.

Table 9 presents the kinematic hardening parameters used during the LS-DYNA simulations.

**Table 9.** Parameters for the Armstrong-Frederick kinematic hardening model estimated for numerical simulation

Strain Amplitude	Temperature	C <sub>1</sub>	γ <sub>1</sub>	C <sub>2</sub>	γ <sub>2</sub>	C <sub>3</sub>	γ <sub>3</sub>
%	°C	MPa	-	MPa	-	MPa	-
0.18	20	150500	1680	450650	2530	10560	1360
0.6	300	5000	83.3	100000	825	1000	1530
0.5	20	1505	1680	15065	253	90500	1360
	300	4000	5	25500	550	100000	1887
1	20	150	1680	1000	253	40000	360

Continuous work has been carried out on the estimation and calibration of the kinematic hardening parameters. Tong, J., and Vermeulen, B. [133]. They performed the experimental and numerical investigation of plasticity, and the viscoplasticity of the nickel-based superalloy kinematic hardening parameters was estimated and optimised for better numerical results. Tong, J. et al. [134], in their extended work from [130], introduced a step-by-step procedure to determine the kinematic hardening parameters and calibrated those using a non-linear least squares method. Zhan, Z., and Tong, J. [135] introduced a dynamic recovery term in the non-linear kinematic hardening model when estimating and calibrating several sets of parameters. Moslemi, N. et al. [136] kept the steps for the estimation of the kinematic hardening parameters for the thin steel sheet under cyclic loading. Koo, G. and Kwon, J. [137] performed an experiment and used these experimental results to estimate the kinematic hardening parameters using a constitutive model followed by finite element simulation using the estimated parameters. Rahman et al. [138] examine several cyclic plasticity models to assess the sensitivity of the model parameters and how the calibration of the initially estimated kinematic hardening parameter affects structural ratcheting during simulations. A study by Kacar [139] reports the process of determination of kinematic hardening parameters from the experimental results with the curve fitting method and the calibration of those kinematic hardening parameters using the finite element simulation approach. Mahmoudi, A. et al. [140] determined the kinematic hardening parameters using a multi-objective generic algorithm. Moslemi et al. [136] estimated the kinematic hardening parameters using a curve-fitting method similar to that in Kacar's [139] work and calibrated these parameters by GA (Genetic Algorithm) and PSO (Particle Swarm Optimisation). Huachao, Y. [64] calibrated the kinematic hardening parameters with the swift extrapolation model using the uniaxial tension flow curve. In their work, Shutong, Z., et al. [141] introduced an approach to estimate and optimise the combined hardening parameters. The parameter optimisation process was performed by the incremental elastic limit concept (IEL), which is implemented by iterative searching under a non-linear curve fitting algorithm. However, the dependence of these parameters on strain amplitude

and temperature was not estimated. To reduce the errors in the estimation of the kinematic hardening parameters, M. Pelegatti et al. [102] developed a new calibration procedure for these parameters.

Despite extensive research on the estimation and calibration of the kinematic hardening parameters, it is still a complex and time-consuming process, and more often than not, these estimated kinematic hardening parameters need to be calibrated during the simulation, which is additional and, again a complex and time-consuming process.

To reduce the complexity, errors, and time consumed during the process of estimating and calibrating the kinematic hardening parameters, relations are formulated for each component, considering the effects of strain amplitude and operating temperature on it. The relations are formulated based on the kinematic hardening parameters presented in Table 10, which are used for the simulation in LS-DYNA. Equations (24-29) present the formulated relation.

$$C_1 = -0.0122\sigma_{YS} - 8.8551 \Delta\varepsilon^2 + 10.5727\Delta\varepsilon + 1.2496T; \quad (24)$$

$$\gamma_1 = -264.3294 \Delta\varepsilon^2 + 715.8896 \Delta\varepsilon + 48.1017T; \quad (25)$$

$$C_2 = 0.1158\sigma_{YS} + 0.0805 \Delta\varepsilon^2 - 26.2504\Delta\varepsilon + 1.4235T; \quad (26)$$

$$\gamma_2 = 9263.575 \Delta\varepsilon^2 + 695.3537\Delta\varepsilon + 21.2144T; \quad (27)$$

$$C_3 = 0.4333\sigma_{YS} + 12.3301 \Delta\varepsilon^2 + 10986.4059 \Delta\varepsilon + 3.2122T; \quad (28)$$

$$\gamma_3 = 10324634.68 \Delta\varepsilon^2 + 5012.0759\Delta\varepsilon + 37.6428T; \quad (29)$$

here:

$\sigma_{YS}$ : Yield stress (MPa)

$\Delta\varepsilon$  : Strain amplitude (%)

$$T = \frac{\text{Operating Temperature } (^{\circ}\text{C})}{20 (^{\circ}\text{C})}$$

The formulated equations (24-29) were used to estimate the kinematic hardening parameters for the strain-controlled low-cycle fatigue tests with different strain amplitudes. The estimated parameters are presented in Table 10. These estimated parameters are employed for the numerical simulation performed using LS-DYNA software.

**Table 10.** Kinematic hardening parameters are estimated using formulated relation

Specimen type		Solid	Hollow
Strain Amplitude	%	1	0.3
Temperature	°C	300	
C <sub>1</sub>	MPa	18640	19300
Y <sub>1</sub>	-	1173.09	912.5
C <sub>2</sub>	MPa	12440	307.4
Y <sub>2</sub>	-	550	485.1
C <sub>3</sub>	MPa	49440	109640
Y <sub>3</sub>	-	842	1642.14

### 3.5. Isotropic Hardening

The isotropic model considers that during any phase of loading, the centre of the yield surface is consistently located at the origin, and the surface expands homothetically in size as the plastic strain progresses. Frequently, a non-linear isotropic model, also called the Voce model [127], is utilised. The alteration of the yield surface is characterised by the variation in the drag stress, R in equation (30) [106-110].

$$R = R_{\infty} [1 - \exp^{-b \varepsilon_{pl,acc}}]; \quad (30)$$

Where  $R_{\infty}$  is the stabilised stress,  $R_{\infty}$  can be positive or negative. Value of  $R_{\infty}$  describes the hardening ( $R_{\infty} > 0$ ) or softening ( $R_{\infty} < 0$ ) behaviour of the material. And b is the rate of stabilisation [43].

The evolution of 'R' in equation (31) can also be estimated as the relative change in the maximum stress of the  $N^{th}$  cycle relative to that of the maximum stress of the first cycle and in the stabilised cycle [11, 107, 109, 121].

$$R = \frac{\sigma_{max,i} - \sigma_{max,1}}{\sigma_{max,s} - \sigma_{max,1}}; \quad (31)$$

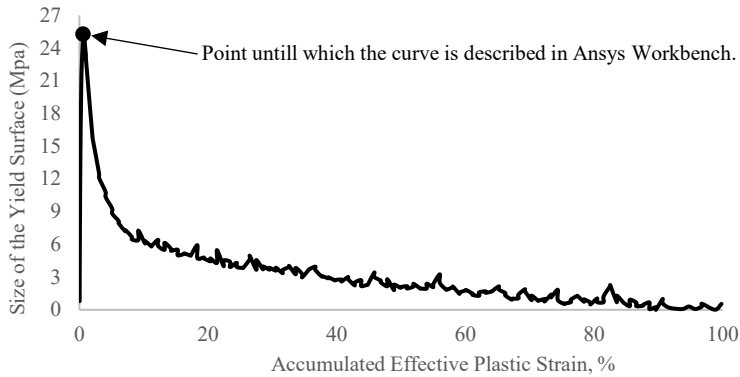
here:

$\sigma_{max,i}$  : Maximum stress in the  $N^{th}$  cycle

$\sigma_{max,1}$  : Maximum stress in the 1<sup>st</sup> cycle

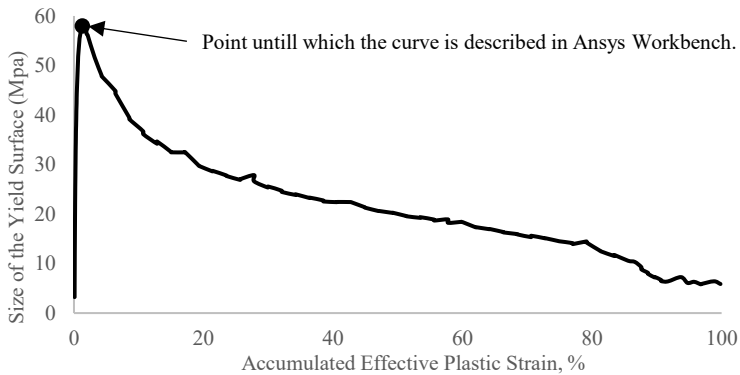
$\sigma_{max,s}$  : Maximum stress in saturated cycle

Figure 18 and Figure 19 illustrate the isotropic hardening curve derived from the experimental results for strain amplitudes of 0.3% and 0.6% at a temperature of 300°C.



**Fig. 18.** Isotropic hardening curve estimated for 0.3% strain amplitude at 300 ° C of the AISI304L stainless steel model

The low-cycle fatigue test simulation for 0.3% and 0.6% strain amplitude was carried out using an Ansys Workbench static structure. While describing the isotropic hardening curve in Ansys Workbench, it did not accept values that were lower than the last entered value for accumulated plastic strain and the evaluation of the surface of the yield. The inability to generate a negative slope resulted in the ability to produce only a positive slope. Consequently, it is limited to accepting only the rising values. To establish the isotropic hardening curve in Ansys Workbench, only a segment of the estimated curve was utilised up to the point highlighted in red in Figure 18 and Figure 19 [11].



**Fig. 19.** Isotropic hardening curve estimated for 0.6% strain amplitude at 300 ° C of the AISI 304L stainless steel model

The isotropic hardening curve was plotted as the evolution of the yield surface versus the accumulated effective plastic strain. Since the elastic modulus is large with respect to the hardening modulus, therefore, the accumulated plastic strain can be calculated as the product of the cycles and the same plastic range. The plastic strain range was calculated according to equation (32).

$$\Delta \varepsilon^{pl} \approx \Delta \varepsilon - \frac{2\sigma_1^t}{E}; \quad (32)$$

The equivalent plastic strain was calculated according to equation (33).

$$\bar{\varepsilon}_c^{pl} = \frac{1}{2}(4i - 3)\Delta \varepsilon^{pl}; \quad (33)$$

The size of the yield surface for each cycle was calculated according to equation (34).

$$\sigma_i^0 = \sigma_i^t - \alpha_i; \quad (34)$$

here:

$$\alpha_i = (\sigma_i^t + \sigma_i^c)/2;$$

The evolution of the yield surface can also be calculated according to equation (35). And the accumulated plastic strain can be presented by equation 36 because, under strain-controlled loading conditions, the  $\Delta \varepsilon_{pl}$  remains roughly constant.

$$\sigma = \sigma_{max,i} - \sigma_{y0}; \quad (35)$$

$$\dot{\bar{\varepsilon}}^{pl} = 2N\Delta \varepsilon_{pl}; \quad (36)$$

The numerical simulations performed using LS-DYNA, the isotropic hardening curve, were calculated using equations (35) and (36). The estimated isotropic hardening curves for 0.18%, 0.6%, 0.5%, and 1% strain amplitude on solid specimens; 0.3% strain amplitude on hollow specimens; and 0.5 mm and 2 mm radius notch specimens are presented in Figure 20 to Figure 28.

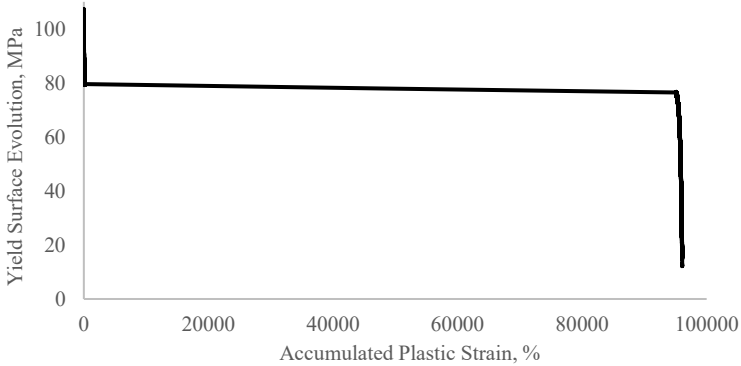


**Fig. 20.** Isotropic hardening curve used in LS-Dyna, AISI 316L for 0.18% strain amplitude at 20°C model

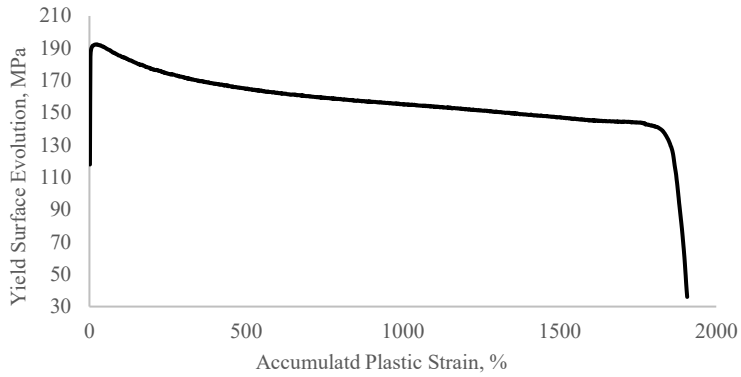


**Fig. 21.** Isotropic hardening curve used in LS-Dyna, AISI 316L for 0.6% strain amplitude at 300°C model

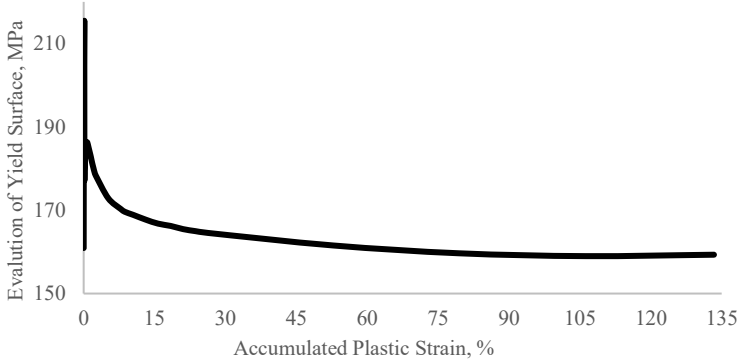


**Fig. 22.** Isotropic hardening curve employed for the numerical simulation of the 0.5% strain amplitude at 20 ° C in a solid specimen

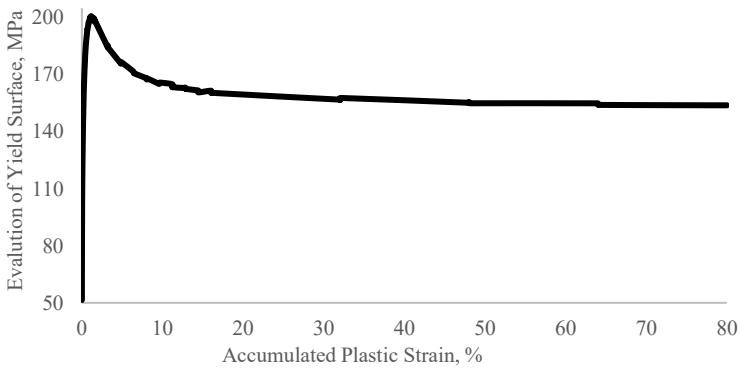


**Fig. 23.** Isotropic hardening curve used for the 0.5% strain amplitude of 0.5% at 300 ° C on a solid specimen

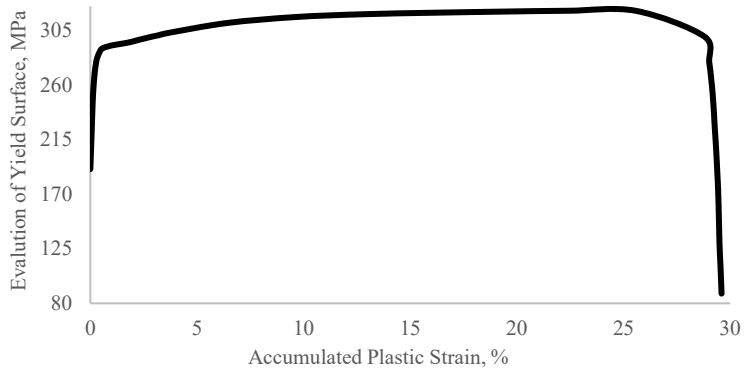


**Fig. 24.** Isotropic hardening curve used for the numerical simulation of the 1% strain amplitude at 20 ° C on solid specimen

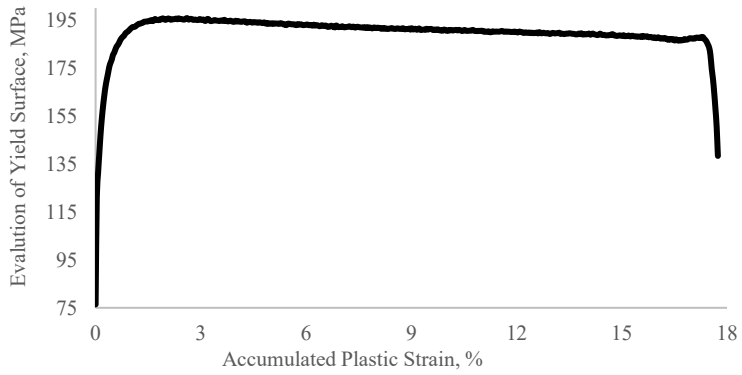


**Fig. 25.** Isotropic hardening curve employed for the numerical simulation of the 1% strain amplitude at 300 ° C in a solid specimen

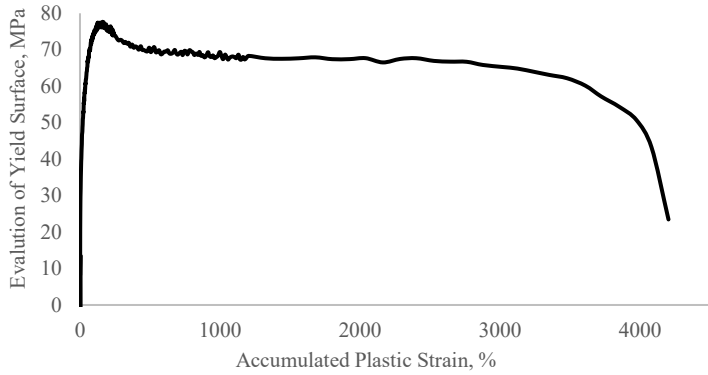


**Fig. 26.** Isotropic hardening curve used for the numerical simulation of 0.3% strain amplitude at 300 ° C in a hollow specimen

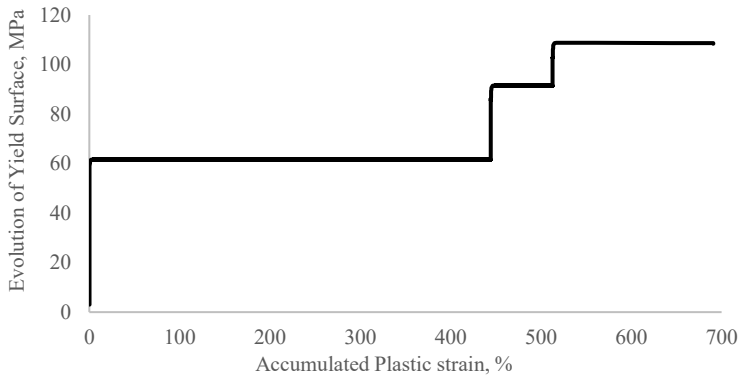


**Fig. 27.** Isotropic hardening curve employed for the notched specimen numerical simulation of the  $r = 0.5$  mm

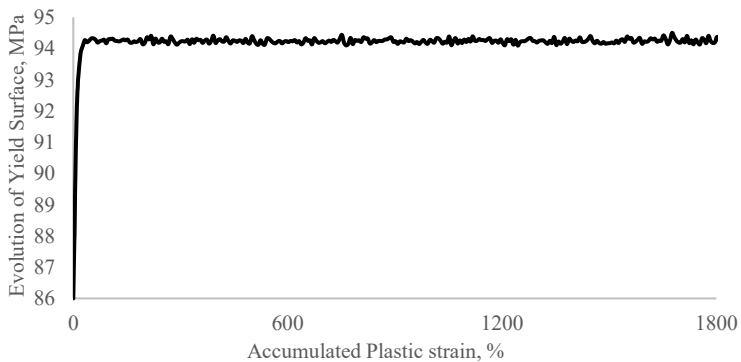


**Fig. 28.** Isotropic hardening curve employed for the numerical simulation of the notched specimen,  $r = 2$  mm

### 3.6. Chapter Conclusion

Numerical investigation using a finite element model is performed for 11 models. The finite element models were prepared on ANSYS Workbench and LS-Dyna software. The elasto-plastic behaviour of the material is described by employing kinematics and isotropic hardening during material modelling. The parameters required to describe the cyclic hardening and softening of the material were estimated using experimental results. The Chaboche and Armstrong-Frederick kinematic hardening rules are used to describe the KH of material in ANSYS Workbench and LS-Dyna, respectively.

The estimation of the kinematic hardening parameters using the available constitutive models is very complex and time-consuming and most of the time requires the calibration to get the expected results, which is an extra step, which is another time-consuming step. Strain amplitude and operating temperature both have their influence on the kinematic hardening parameters. Therefore, relations are formulated for the estimation of kinematic hardening parameters by considering the effects of the strain amplitude and operating temperature and to reduce the time required and eliminate the calibration process. The relations between kinematic hardening parameters, strain amplitude and operating temperature are formulated, and the parameters estimated using these relations are validated by using them in the material model without a calibration process.

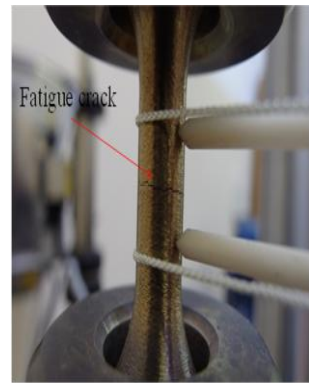
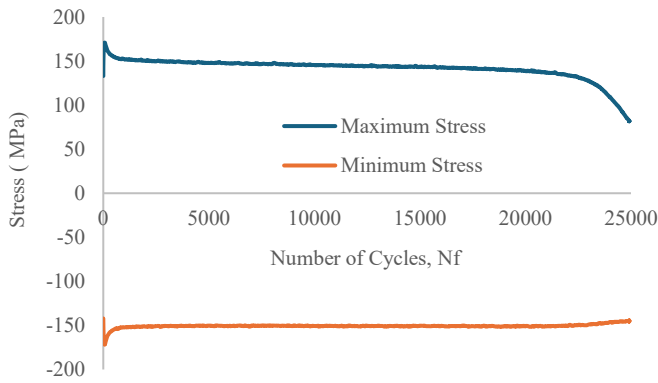
## 4. EXPERIMENTAL RESEARCH RESULTS

Low cycle fatigue (LCF) experimental testing is a crucial method for understanding material fatigue behaviour under controlled, baseline conditions. Air testing provides a reference for the material's fatigue life, allowing researchers to isolate the mechanical fatigue response without environmental interference. This is useful for comparing different materials or heat treatments under consistently standardised conditions. Air testing is simpler and more cost-effective than high-pressure/high-temperature environments, as it does not require complex infrastructure, water chemistry control, or safety measures. International fatigue testing standards (ASTM and ISO) are based on air tests, allowing results to be directly compared to existing data for material qualification and design. Air testing also aids in model development and validation, helping to develop and validate cyclic plasticity models, strain-life curves, and fatigue damage parameters under controlled conditions. Component design and screening are essential for the initial screening of candidate materials for fatigue performance before investing in more expensive, environment-specific testing. Air fatigue data is essential for understanding degradation in more aggressive environments and calibrating environmental penalty factors.

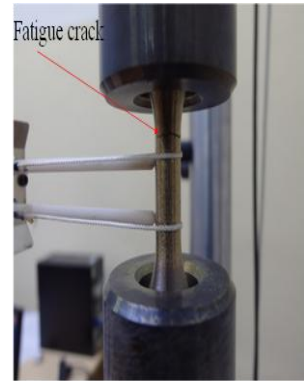
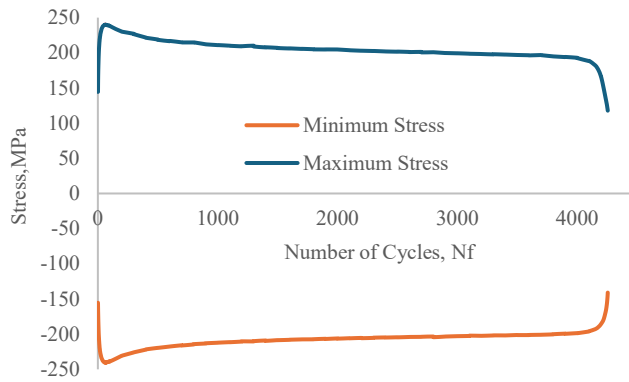
The experimental test results for all 11 low-cycle fatigue experiments performed are plotted as stress versus number of cycles curves for strain-controlled constant-amplitude low-cycle fatigue. For the stress-controlled low-cycle fatigue test, the curve was plotted as strain versus the number of cycles.

Figure 29 presents the experimental results for the 0.3% strain amplitude at 300°C on AISI 304L stainless steel. The stress versus number of cycles is shown in Figure 29a, and Figure 29b, a picture of the specimen with a crack after failure is shown. The crack in the specimen was observed in the centre of the gauge length. From the stress versus number of cycles curve, it is observed that for the initial few cycles, the maximum stress increased for each successive cycle until the 61<sup>st</sup> cycle, and then the reduction in maximum stress was observed, followed by a kind of stabilised region and failure of the specimen. The specimen failed in the 24923<sup>rd</sup> cycle.

Figure 30a and Figure 30b show the experimental results for the 0.6% strain amplitude at 300°C in AISI 316L stainless steel. The material behaviour observed was similar to the 0.3% strain amplitude shown in Figure 29a. The maximum stress increased up to the 61<sup>st</sup> cycle, and a reduction in the maximum stress was observed, and the material failed in the 4256<sup>th</sup> cycle. The crack was observed outside of the gauge length on the upper side of the specimen (Figure 30b). The crack must have occurred outside the length of the gauge, and it may be related to the localised stress concentration near the gauge fillet [47].

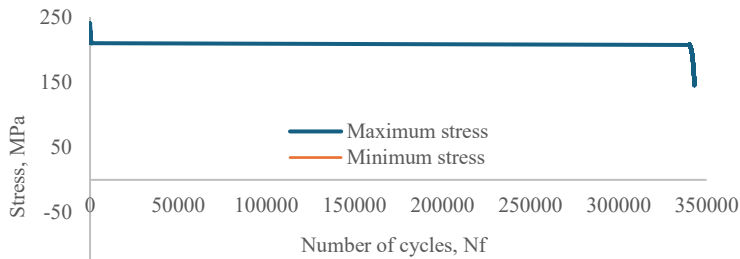


**Fig. 29.** Experimental results: stress curve versus number of cycles for AISI304L stainless steel for 0.3% strain amplitude at 300 °C



**Fig. 30.** Experimental results: stress curve versus number of cycles for AISI304L stainless steel for 0.6% strain amplitude at 300 °C

Experiments on AISI 316L stainless steel for 0.18% amplitude at 20°C and 0.6% strain amplitude at 300°C were performed until the specimen failure. Figure 31 and Figure 32 present the experimental results for the same [12]. In both specimens, a crack appeared at the centre of the gauge length. Figure 31b and Figure 32b show the cracked experimental specimen. The experimental findings for low-cycle fatigue at a strain amplitude and room temperature indicated an increase in the maximum stress observed in each cycle up to the sixth cycle. Beginning with the seventh cycle, the peak stress per cycle diminishes until the 1235<sup>th</sup> cycle, after which a stabilised region appears, maintaining a stress range between 210 MPa and 214 MPa up to the 326,557<sup>th</sup> cycle. Following the 326,557<sup>th</sup> cycle, the maximum stress consistently decreases over successive cycles, leading to the failure of the specimens, specifically the fracture that occurred during the 342,870<sup>th</sup> cycle [12].

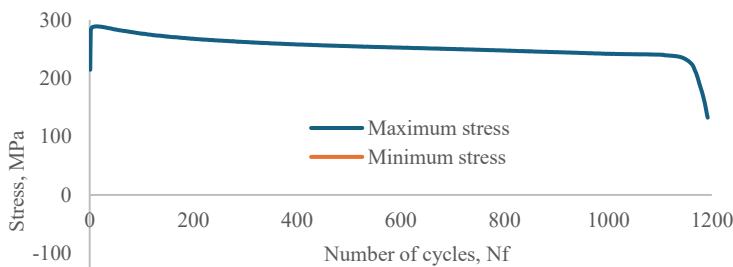


a

b

**Fig. 31.** Experimental results: stress curve versus number of cycles for AISI316L stainless steel for 0.18% strain amplitude at 20 ° C

The findings of another experiment conducted on an AISI 316L stainless steel component at 300°C with a strain amplitude illustrate a similar pattern: the maximum stress during the initial cycles rises until the 10<sup>th</sup> cycle, after which it steadily declines until the component finally fails in the 1183<sup>rd</sup> cycle. No stabilised region was detected in the experiment with a strain amplitude, nor was one found in the experiment with the results of the 0.18% strain amplitude. It is observed in the results of both experiments that there is a typical behaviour where the maximum stress decreases following an increase in stress during the initial few cycles. This evidence indicates that AISI 316L stainless steel demonstrates a softening behaviour of the material when subjected to cyclic loading [12]. Failure was considered when there was a 25% drop in stress level with respect to the maximum stress level. The specimen for 0.18% and 0.6% strain amplitude failed in the 343106<sup>th</sup> (Figure 31) and 1192<sup>nd</sup> (Figure 32) cycles, respectively [43].



a

b

**Fig. 32.** Experimental results: stress versus number of cycles curve for AISI316L stainless steel for 0.6% strain amplitude at 300 ° C

The next set of experiments consisted of a total of 5 experiments performed in the EDF laboratory. The results for all 5 experiments are presented in Figure 33 to Figure 37. This set of experiments was performed on a solid specimen and a hollow specimen. On a solid specimen, four experiments were performed for 0.5% and 1% strain amplitude at 20°C and 300°C. And the hollow specimen was tested for 0.3% strain amplitude at 300°C in a PWR (pressurised water reactor) environment.

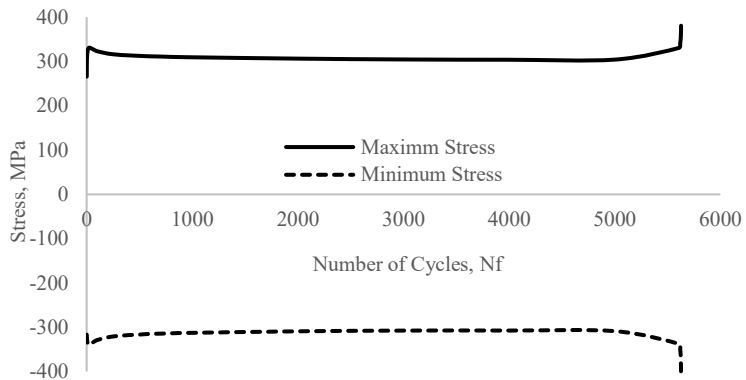


**Fig. 33.** Experimental results of solid specimen for 0.5% strain amplitude, stress versus number of cycles at 20 ° C (EDF laboratory test results)

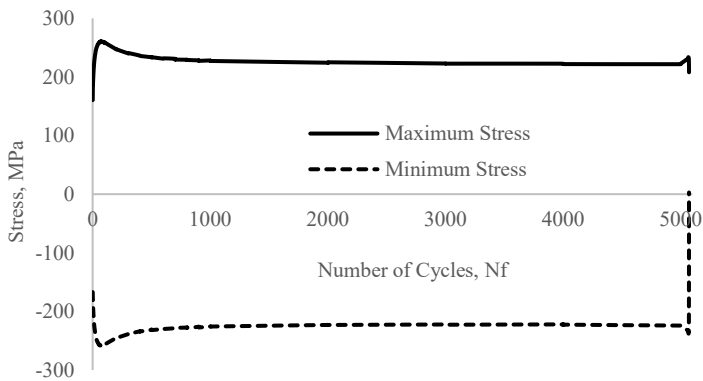


**Fig. 34.** Experimental results of solid specimen for 0.5% strain amplitude, stress versus number of Cycles at 300 ° C (EDF laboratory test results)

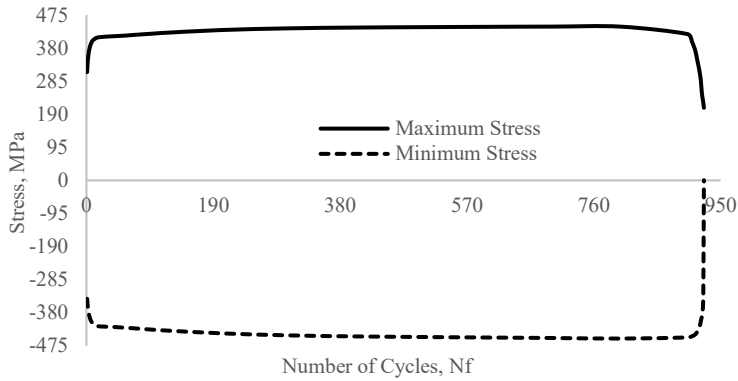


**Fig. 35.** Experimental results of a solid specimen for 1% strain amplitude, stress versus Number of Cycles at 20 ° C (EDF laboratory test results)

The failure of the specimen tested at 0.5% strain amplitude at 20°C was observed at the 5628<sup>th</sup> cycle (Figure 33). The maximum stress in the case of this experiment was observed to increase in the failure cycle, which may occur because the crack was formed outside the gauge length. Figure 34 presents the experimental results for the 0.5% strain amplitude at 300°C; the failure in this test was observed in the 5072<sup>nd</sup> cycle.

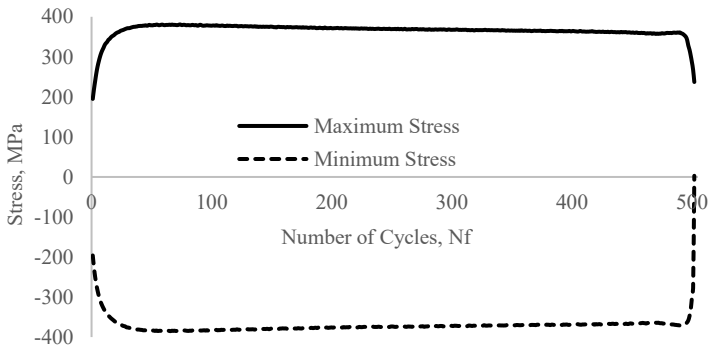


**Fig. 36.** Experimental resultss of a solid specimen for 1% strain amplitude, stress versus Number of Cycles at 300 ° C (EDF laboratory test results)

The specimen tested for 1% strain amplitude at 20 and 300 ° C failed in the 925<sup>th</sup> (Figure 35) and 502<sup>nd</sup> cycle (Figure 36).

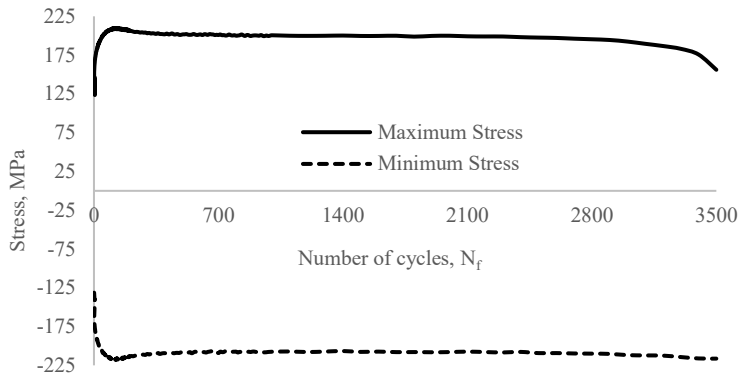


**Fig. 37.** Experimental results of a hollow specimen for 0.3% strain amplitude, Stress versus Number of Cycles at 300 °C (EDF laboratory test results)

Low cycle fatigue (LCF) testing is commonly conducted in pressurised water reactor (PWR) environments to simulate the actual operating conditions of nuclear reactor components, particularly those in the primary circuit. PWRs operate at temperatures of 280-325°C and pressures of 16.6 MPa, and materials exposed to these conditions may degrade differently due to corrosion fatigue, environmentally assisted cracking (EAC), and environmentally assisted fatigue (EAF) effects. Research and operational experience show that fatigue life in PWR environments can be significantly shorter than in air due to oxidation at the crack tip, dissolved oxygen and hydrogen effects, and enhanced crack growth mechanisms. Such evidence has led to the development of environmental fatigue correction factors. LCF testing also helps in ensuring compliance with nuclear regulatory bodies, including environmental effects in fatigue evaluation. It also supports material qualification and ageing studies, evaluating the degradation behaviour of alloys like 316 SS, Inconel, and low-alloy steels under combined mechanical and environmental loading.

Figure 37 displays the experimental results for the hollow specimen tested at a strain amplitude of 0.3% and a temperature of 300°C in a pressurised water reactor (PWR) environment. The failure was observed in the 3500<sup>th</sup> cycle (Figure 37).

The results of all the strain-controlled experimental tests indicate that the material behaved similarly. For the initial few cycles, the maximum temperature increases for each consecutive cycle, followed by a reduction in the maximum stress for the next few cycles, a stabilised region and finally failure. This phenomenon is known as “softening behaviour”. Softening is related to dynamic recrystallisation at room temperature and grain rotation at higher temperatures [142].

From the experimental results, it is observed that the failure of the specimen is largely affected by the strain amplitude applied to the specimen during experimental testing. The number of cycles required for the specimen's failure at the respective strain amplitude is presented in Table 11. It is observed that the operating temperature also has some degree of influence on the failure of the specimen.

**Table 11.** Non-notched specimen failure cycle for experimental test on AISI316L stainless steel

Sr. No.	Strain Amplitude	Temperature	Cycle number
	%	°C	N <sub>f</sub>
1	0.18	20	343106
2	0.3	300	3500
3	0.5	20	5628
4		300	5072
5	0.6	300	1192
6	1	20	925
7		300	502

AISI 316L stainless steel was also tested with the notch specimen. Experimental low-cycle fatigue (LCF) testing is conducted on notched specimens to simulate real-world conditions, study localised behaviour, and improve understanding of fatigue performance in components with stress concentrators. Notched specimens replicate geometric discontinuities like holes, notches, fillets, or grooves, which cause stress concentrations. Stress-controlled loading represents many actual loading situations where force or pressure is applied, rather than prescribed displacement/strain. Notched specimens allow the study of stress gradient effects, localised plasticity under cyclic loading, and the notch sensitivity of different materials, which helps in predicting fatigue life more accurately. Notches induce triaxial stress states and localised plastic deformation, enabling the evaluation of cyclic hardening and softening behaviour and the study of crack initiation and propagation in critical regions. LCF testing validates finite element (FE) models and design criteria, supporting conservative fatigue life estimations in safety-critical components. It also provides challenging validation cases for material models for cyclic plasticity and fatigue, which are then used in FEA simulations. Notched specimens naturally promote crack initiation at stress concentration sites and allow the study of short-crack behaviour, which is important for LCF regimes. There were two specimens with different notch radii of 0.5 and 2 mm, respectively, at a temperature of 300°C. The experiment for the notched specimens was stress controlled, unlike the non-notched specimens, which were strain-controlled tests.

The low-cycle fatigue testing was performed on notched specimens under stress-controlled loading conditions to ensure uniformity throughout the experimental testing program (in air and PWR environments). To make it easy to compare with the strain-controlled uniaxial testing, the loads were applied to create a strain at the notched tip equivalent to the strain amplitude in the case of the strain-controlled LCF tests. The laboratory involved in the testing programme did not have the capability to test in a PWR environment for the required gauge length extensometer.

The specimen with a 0.5 mm radius notch was exposed to fully reversed variable-amplitude loading. Failure was observed in the 16251<sup>st</sup> cycle (Table 12) with the crack in the centre of the specimen, which is also the root of the notch (Figure 38).

Similarly, for the specimen with a 2 mm radius notch, the failure occurred in the 29660<sup>th</sup> cycle (Figure 39). In both cases, it was observed that as the stress loading increased, the strain also increased. Figure 38b and Figure 39b show the cracked notched specimens.

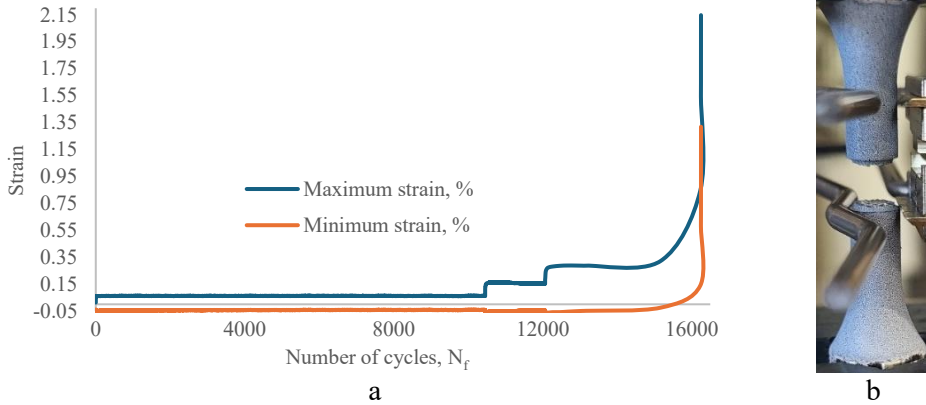


**Fig. 38.** Experimental results for  $r=0.5\text{mm}$  notched sample, strain versus number of Cycles at  $300\text{ }^{\circ}\text{C}$

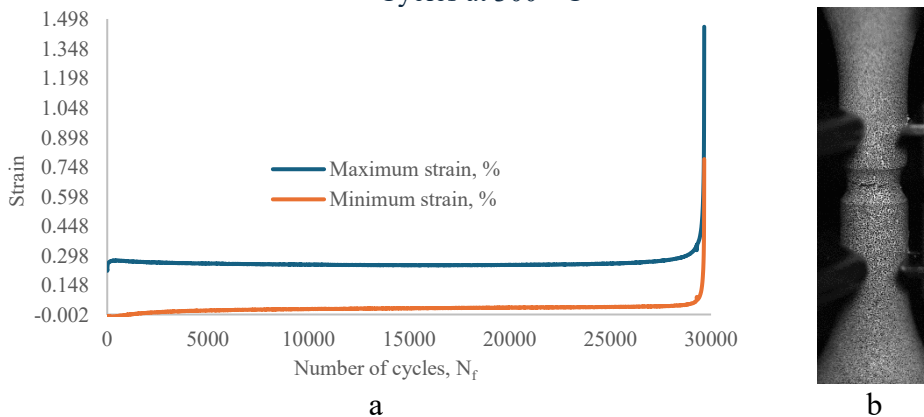


**Fig. 39.** Experimental results for  $r=2\text{mm}$  notched sample, strain versus number of Cycles at  $300\text{ }^{\circ}\text{C}$

**Table 12.** Notched specimen failure cycle for experimental test on AISI316L stainless steel

Sr. No.	Notch radius	Temperature	Type of loading	Cycle number
	mm	$^{\circ}\text{C}$		$N_f$
1	0.5	300	Stepped	16251
2	2		Constant amplitude	29660

## 4.1. Chapter Conclusion

An experimental investigation on the low-cycle fatigue behaviour of austenitic stainless steel was carried out on a non-notched solid specimen, a notched solid specimen, or a hollow specimen exposed to constant or variable amplitude loading at room temperature or elevated temperature in this research. Conducting LCF testing in air is essential for creating a reliable, consistent, and cost-effective basis for fatigue studies. The method facilitates the analysis of materials and the creation of models and serves as a standard for quantifying the impacts of environmental degradation, such as those arising from PWR conditions. A solid specimen made of AISI 304L stainless steel was tested for 0.3% and 0.6% strain amplitude. AISI 316L stainless steel was tested for 0.18%, 0.6%, 0.5% and 1% strain amplitude. A hollow specimen of AISI 316L steel was tested under 0.3% strain amplitude in a PWR environment at 300°C. Testing under PWR conditions is essential to effectively forecast the service life and guarantee the safety and reliability of vital nuclear components by integrating realistic environmental degradation mechanisms. This offers essential information for design standards and safety evaluations in the field of nuclear engineering.

The experiments were carried out using an Instron E10000 fatigue testing machine. AISI 316L SS was also tested with two different radius-notched specimens under a stress-controlled regime. Stress-controlled LCF tests on notched specimens are essential for modelling real service loads and stress distributions, investigating localised fatigue and crack initiation, and assessing material models and design approaches. This turns them exceptionally relevant for evaluations of structural integrity and applications in nuclear, aerospace, or pressure vessel contexts where predicting fatigue life is essential.

The strain amplitude significantly influences the failure cycle number in the strain-controlled low-cycle fatigue test. The failure of the specimen is also slightly affected by the operating temperature. There was a common behaviour observed from the maximum stress versus the number of cycles curve plotted for all the strain-controlled experimental test results: cyclic hardening for initial cycles, cyclic softening followed by a kind of stabilised region, then a drop in the stress level and finally fracture. In the case of stress-controlled experimental test results, the maximum strain versus the number of cycles curve was plotted, and an increase in the strain level is observed as the number of cycles increases and a sudden spike at the failure of the specimen.

## 5. NUMERICAL SIMULATION RESEARCH RESULTS AND VALIDATION

Numerical investigation using a finite element model is performed on austenitic stainless steel for strain-controlled and stress-controlled low-cycle fatigue. In this section all the numerical simulation results along with the validation will be explained.

To begin with the numerical simulation investigation, the full specimen (Figure 10) and the reduced specimen (Figure 12) were both exposed to 0.3% strain amplitude to check the effects of the specimen size on the simulation results. No effects of the specimen size were observed on the simulation results (Figure 40). The results for both the specimens were identical. This conclusion was observed because, if appropriate boundary conditions and loads are applied to the specimen model, the non-gauge part of the specimen, like the shoulder, end section, etc., does not have any significant effects on the numerical simulation results. But the full specimen took more than 1 hour to compute, and the reduced specimen took just a few seconds to compute (Table 13). To reduce the time required for the computation of the model, all the finite elements were prepared for the reduced specimen ( $1/4^{th}$  portion of the specimen gauge length).

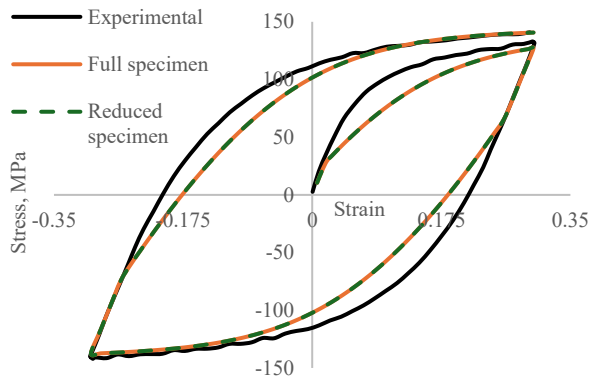


**Fig. 40.** Comparison of simulation results of full specimen and reduced specimen

**Table 13.** Time required for the computation for the first cycle

Model type	Time required for the computation
Full specimen	1h 20m
Reduced specimen	15 sec

After the decision on the specimen size to model, the finite element model was checked for the sensitivity of the numerical simulation to the mesh size of the model. Mesh sensitivity is very important in the numerical simulation of low-cycle fatigue to be sure of the accuracy and reliability of the results, specifically the stress, strain fields and fatigue life of the specimen.

For the mesh sensitivity analysis, 4 finite element models were prepared with the element sizes of 0.5 mm, 1 mm, 5 mm, and 10 mm. All these models were prepared for the 0.3% strain amplitude on the AISI 304L SS experimental test. There were no effects of the mesh size on the simulation results observed (Figure 41) due to the simplicity of the model and boundary conditions. For the reliability and efficiency of the numerical simulation results, 1 mm mesh size was selected for the finite element models for the strain-controlled low-cycle fatigue simulations.

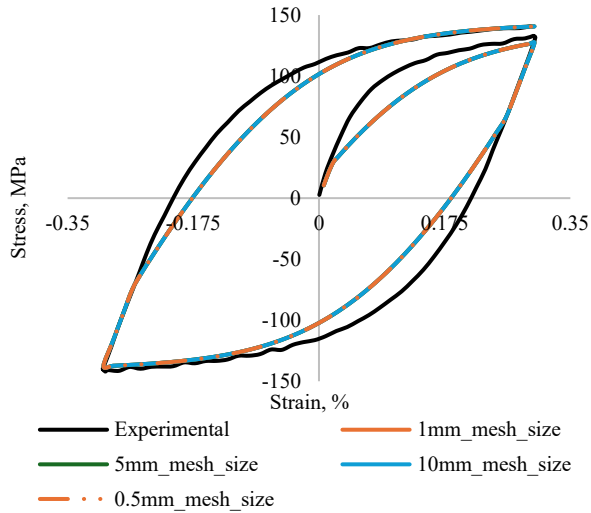


**Fig. 41.** Mesh sensitivity check

The simulation results for the AISI 304L stainless steel LCF tests from the ANSYS workbench showed agreement with the experimental results. As the cycle progresses, a deviation in the maximum stress values is observed. The shape of the stress-versus-strain hysteresis loop plotted for the simulation results against the experimental results was quite similar. Figure 42 and Figure 43 show the hysteresis loop of the 1<sup>st</sup> and the 2000<sup>th</sup> cycles for 0.3% and 0.6% strain amplitudes. For the 1<sup>st</sup> cycle, in the case of both strain amplitudes, the simulation curve is very close to the experimental curve. And in the case of the 2000<sup>th</sup> cycle, deviation is observed for both the strain amplitudes. Figure 44 presents the maximum stress for each cycle versus the number of cycle curves. This figure consists of experimental, and simulation results for both strain amplitudes.

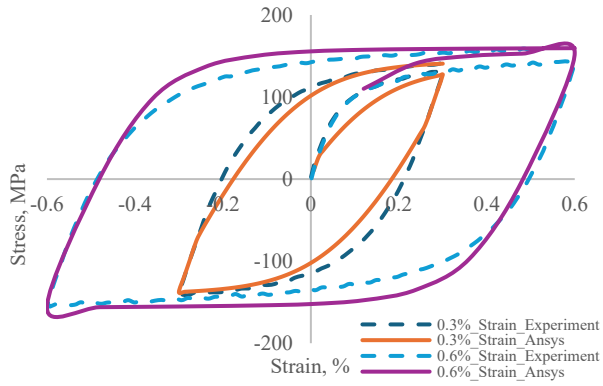


**Fig. 42.** First cycle for AISI304L stainless steel at 300 °C

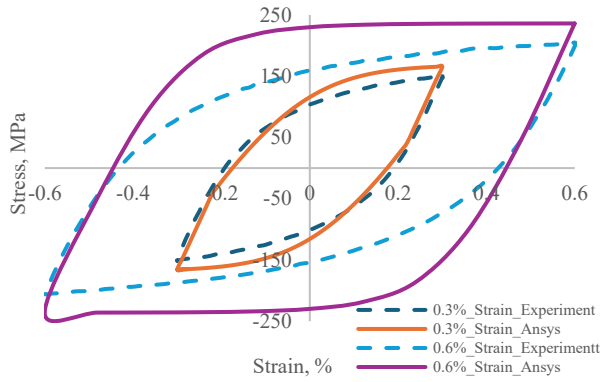


**Fig. 43.** 2000<sup>th</sup> cycle for AISI304L stainless steel at 300 °C

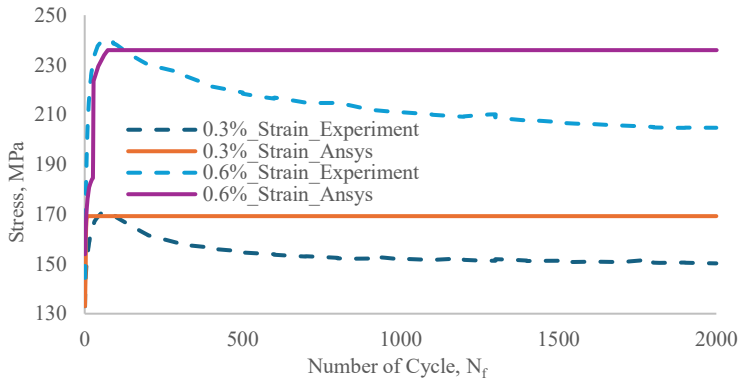


**Fig. 44.** Stress curve versus number of cycles for AISI304L stainless steel at 300 °C

For the simulation results of the 0.3% strain amplitude model, the results matched for the initial few cycles, but after the seventh cycle, the maximum stress did not change for the rest of the simulation, and the values deviated by 18.95% from the experimental results. In the case of the 0.6% strain amplitude simulation model, similar stress versus number of cycle curves with the 0.3% strain amplitude model. During the initial few cycles, the simulation results closely matched the experimental results; however, an unexpected spike occurred in the values, and after the 75<sup>th</sup> cycle, the maximum stress remained constant for all subsequent cycles. The simulation values deviate by 19.9% from the experimental results. Constant values of the maximum stress were observed due to the isotropic curve defined in the ANSYS workbench. It did not accept the values for the curve that have a negative slope, and eventually it was unable to catch the softening behaviour of the material as was observed in the experimental results.

The simulation in the solid specimen produced from AISI 316L stainless steel for the 0.18% strain amplitude at 20°C and the 0.6% strain amplitude at 300°C was carried out using the LS-Dyna FE software employing a default explicit solver. The reliability of components exposed to the cyclic loading can be estimated if the cyclic plastic behaviour of the material should be modelled until the stabilisation of the results, which is observed around the 50% cycles of the total number of cycles till failure of the component [12, 91, 137]. The simulation for the 0.18% strain amplitude model was performed for 170000 cycles, which is 50% of the experimental life of the specimen, and the 0.6% strain amplitude model simulation was performed for full experimental cycles, i.e., 1200 cycles. The simulation results are compared with the experimental results by plotting the stress versus strain loop for the 1<sup>st</sup> (Figure 45) and 2000<sup>th</sup> (Figure 46) cycles in the case of the 0.18% strain amplitude model, and for the 0.6% strain amplitude model, the 1<sup>st</sup> (Figure 48) and 500<sup>th</sup> (Figure 49) cycles were plotted.

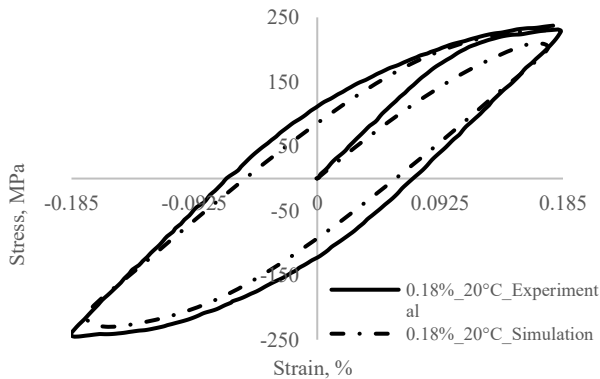


**Fig. 45.** First cycle for AISI316L stainless steel for 0.18% strain amplitude at 20 ° C

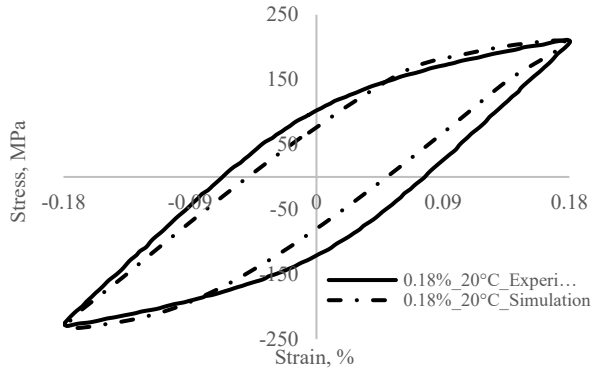


**Fig. 46.** 2000<sup>th</sup> cycle for AISI316L stainless steel for 0.18% strain amplitude at 20 ° C

From the stress versus strain hysteresis loop, it was observed that the plastic-elastic stress and strain interaction point deviates between the simulation and the experimental results.

To validate the simulation model for the complete life of the component, the maximum stress per cycle was plotted against the corresponding number of cycle curves for the simulation results to compare with the experimental results. Figure 47 and Figure 50 present the maximum stress versus number of cycles curves for the 0.18% and 0.6% strain amplitude models, respectively.

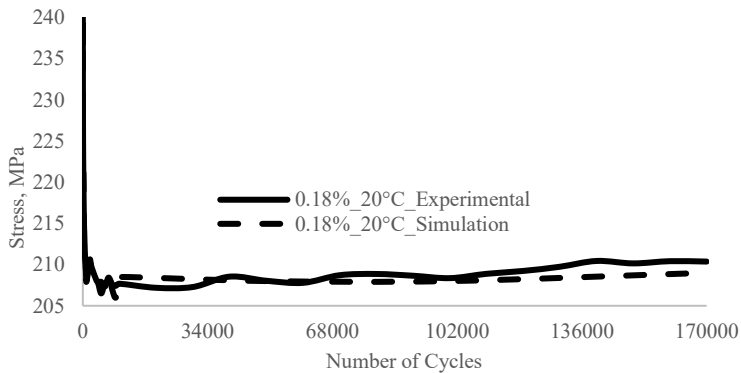


**Fig. 47.** Stress curve versus number of cycles for AISI316L stainless steel for 0.18% strain amplitude at 20 ° C

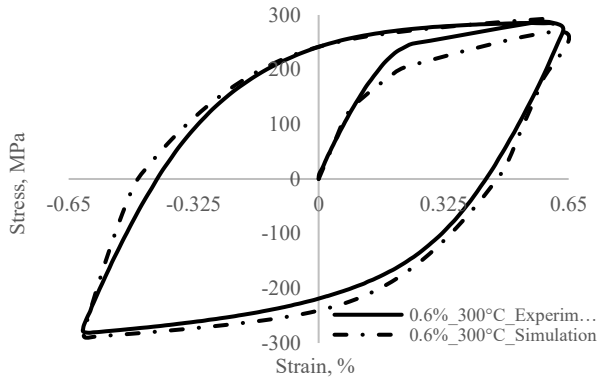


**Fig. 48.** First cycle for AISI316L stainless steel for 0.6% strain amplitude at 300 ° C

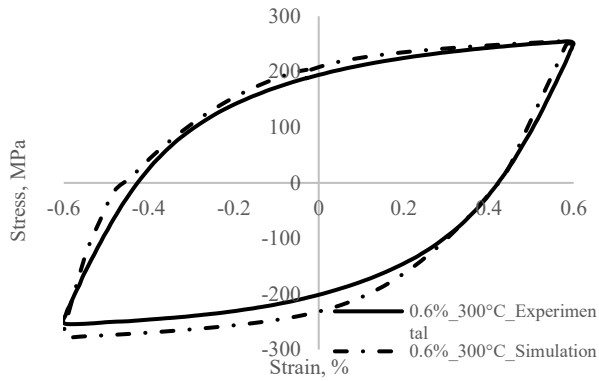


**Fig. 49.** 500<sup>th</sup> cycle for AISI316L stainless steel for 0.6% strain amplitude at 300 ° C

The simulation results were very close to the experimental results. Initially, the maximum stress values from simulation results deviate with respect to the experimental results, but as the simulation progresses, the results get better. The maximum stress differs by 1.58% for the initial 100 cycles: between the 101<sup>st</sup> and 170000<sup>th</sup> cycles, the values deviated by 0.5% for the 0.18% strain amplitude model [12].

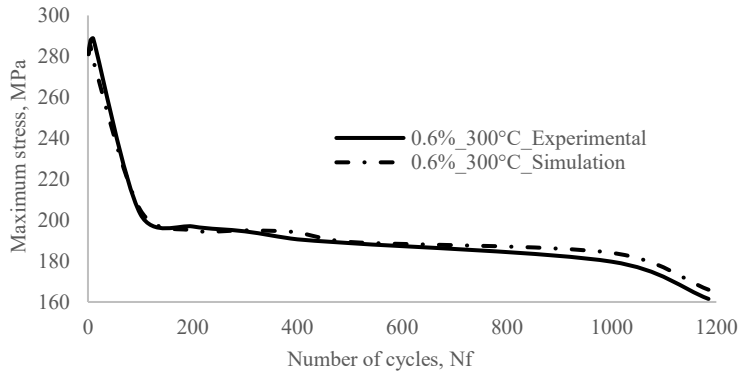


**Fig. 50.** Stress curve versus number of cycles curve for AISI316L stainless steel for 0.6% strain amplitude at 300 ° C

In the case of the 0.6% strain amplitude model, the results are by 3.7% and 1% for cycles between the 1<sup>st</sup> – 61<sup>st</sup> cycle and the 61<sup>st</sup> to 1192<sup>nd</sup> cycle, respectively.

The simulation results performed on the solid specimen at 20°C and 300°C for a strain amplitude of 0.5% and 1% are also presented in the form of a stress versus strain hysteresis loop and curve for maximum stress versus number of cycles. Figure 51 to Figure 54 present the stress versus strain hysteresis loop for 0.5% strain amplitude at 20°C and 300°C and 1% strain amplitude at 20°C. The simulations for these three schemes were performed employing the kinematic hardening parameters estimated by using the Armstrong-Fredrick kinematic hardening model.

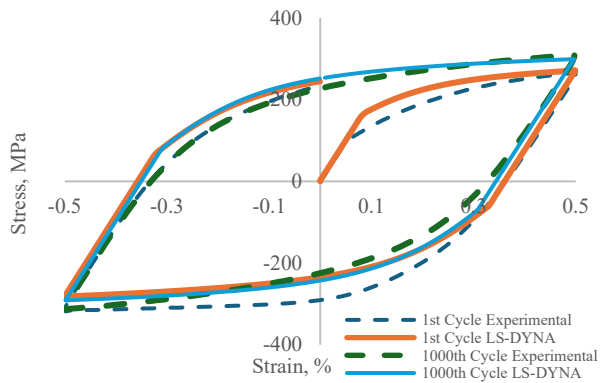


**Fig. 51.** Stress versus strain curve of the solid specimen for 0.5% strain amplitude at 20 ° C

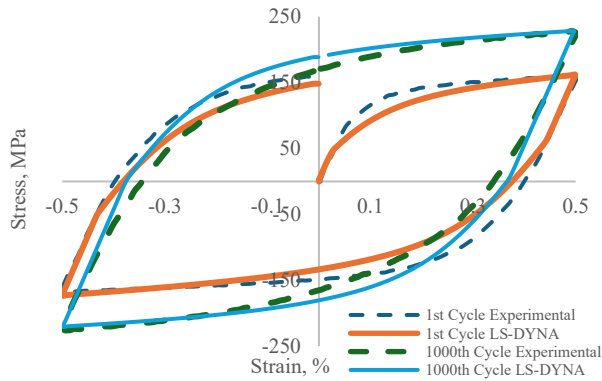


**Fig. 52.** Stress versus strain curve of the solid specimen for 0.5% strain amplitude at 300 ° C

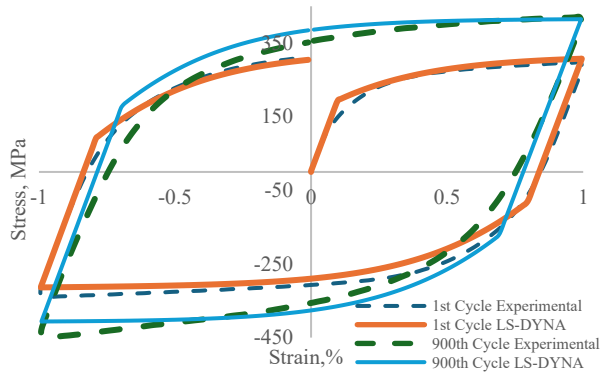


**Fig. 53.** Stress versus strain curve of solid specimen for 1% strain amplitude at 20 ° C

The stress versus strain curves were plotted for the 1st cycle for all the schemes and along the 1000<sup>th</sup> cycle for the 0.5% strain amplitude simulation at both temperatures and the 900<sup>th</sup> for the 1% strain amplitude at 20°C. Upon comparing the simulation results with the experimental results, they were observed to be closely analogous to the experimental results for all three schemes.

The results for these three schemes were acceptable. Therefore, based on the kinematic hardening parameters, using those parameters, relations were formulated for all the kinematic hardening parameters by taking into account the strain amplitude and the temperature. Using the equation formulated (14-19), the kinematic hardening parameters were estimated and used for the simulation of a solid specimen at 1% strain amplitude and a hollow specimen at 0.3% strain amplitude at both 300°C.

Stress versus strain curves were plotted for the 1<sup>st</sup> and 300<sup>th</sup> (Figure 54) and 1<sup>st</sup> and 3000<sup>th</sup> (Figure 55) cycles for a solid and a hollow specimen. The simulation results were very close to the experimental results. Kinematic hardening parameters were used without any calibration of the estimated parameters.

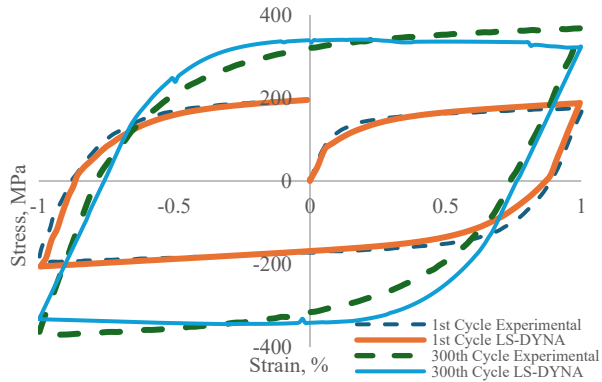


**Fig. 54.** Stress versus strain curve of the solid specimen for 1% strain amplitude at 300 ° C

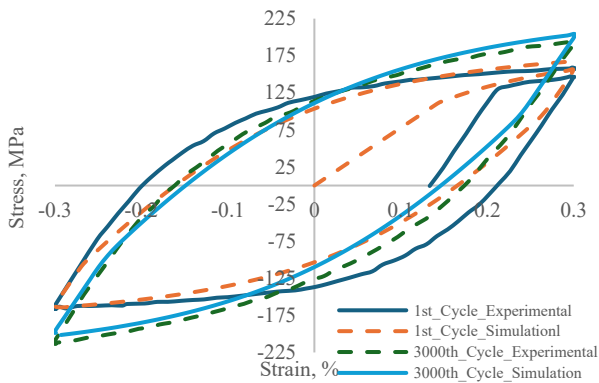


**Fig. 55.** Stress versus strain curve of the hollow specimen for 0.3% strain amplitude at 300 ° C

The maximum stress curve plotted against the corresponding number of cycles for the experimental and numerical simulation results is presented in Figure 56 to Figure 60. On comparing the simulation results with the experimental results, the simulation results were very close to the experimental results.

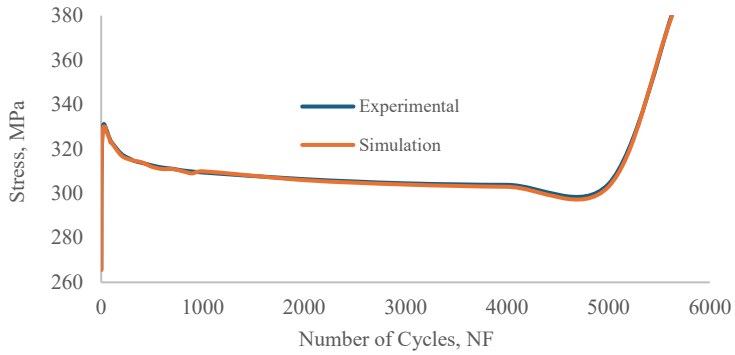


**Fig. 56.** Maximum stress v/s number of cycles for solid experimental and simulation specimen with strain amplitude 0.5% at 20 ° C

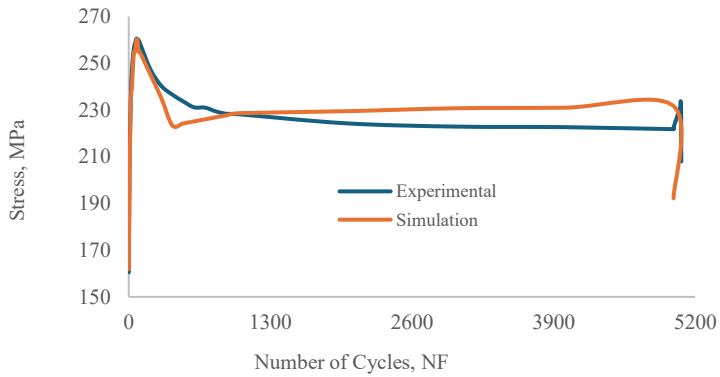


**Fig. 57.** Maximum stress v/s number of cycles for solid experimental and simulation specimens with strain amplitude 0.5% at 300 ° C

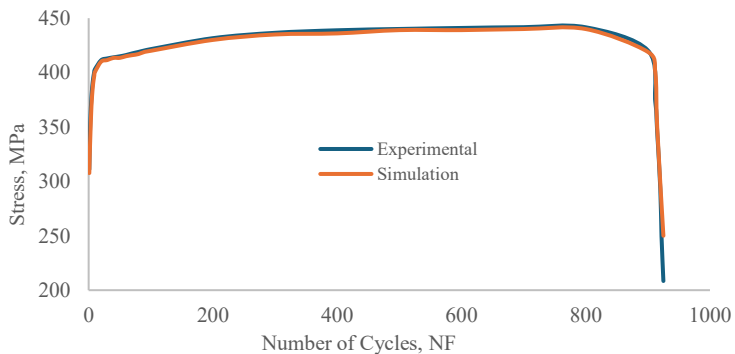


**Fig. 58.** Maximum stress v/s number of cycles for the solid specimen experimental and simulation with strain amplitude 1% at 20 ° C

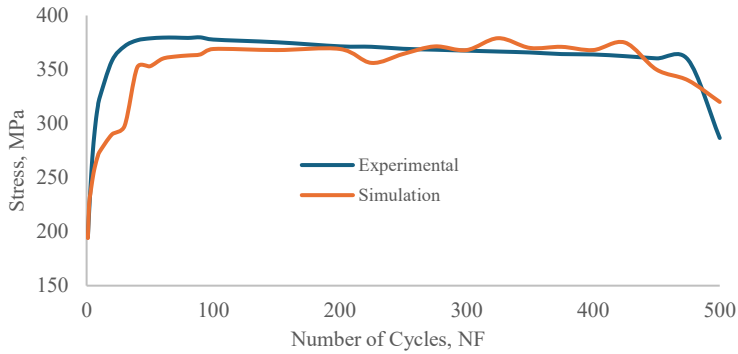


**Fig. 59.** Maximum stress v/s number of cycles for solid experimental and simulation specimen with strain amplitude 1% at 300 ° C

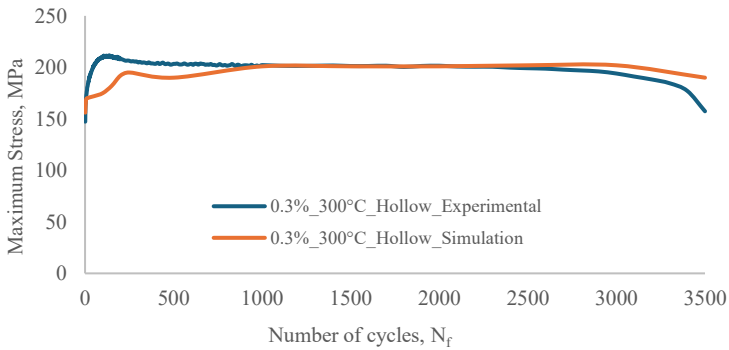


**Fig. 60.** Maximum stress v/s number of cycles for experimental and simulation hollow specimen at 0.3% strain amplitude at 300 ° C

The simulation results vary by a maximum of 0.6% and 8.1% in the failure for 0.5% strain amplitude at 20 and 300°C and 16% at the failure of 1% strain amplitude at 20°C. More deviations were observed for the strain amplitudes of 1% and 0.3% at 300°C. As mentioned earlier, the kinematic hardening parameters used for these simulations were estimated using the formulated equation (21-26) and were not calibrated. The 10% deviation was observed at the failure of the specimen in the simulation for both schemes: 1% strain amplitude solid specimen and 0.3% strain amplitude hollow specimen at 300°C. The maximum deviations of 13% and 19% occurred during the initial cycles [143].

Figure 61 to Figure 64 present the comparison of simulation results with the experimental results for the stress-controlled low-cycle fatigue test on notched specimens

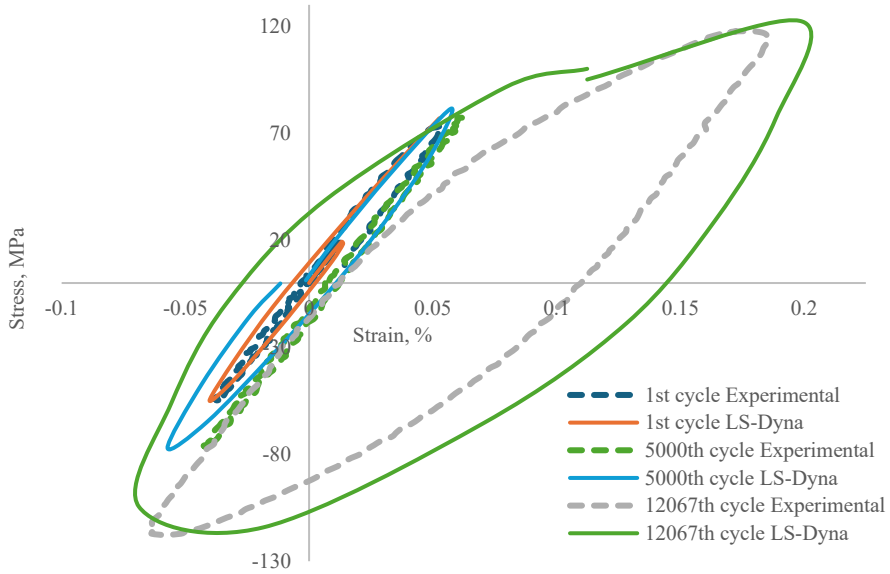


**Fig. 61.** Stress versus strain curve for  $r=0.5$  mm notched specimen at  $300^{\circ}\text{C}$

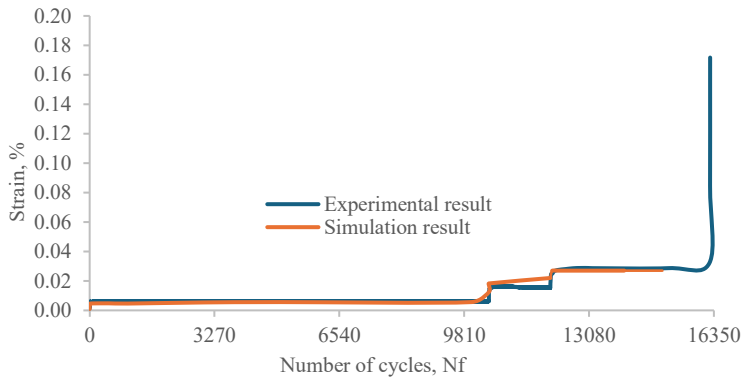


**Fig. 62.** Maximum stress v/s number of cycles for experimental and simulation  $r=0.5$  mm notched specimen at  $300^{\circ}\text{C}$

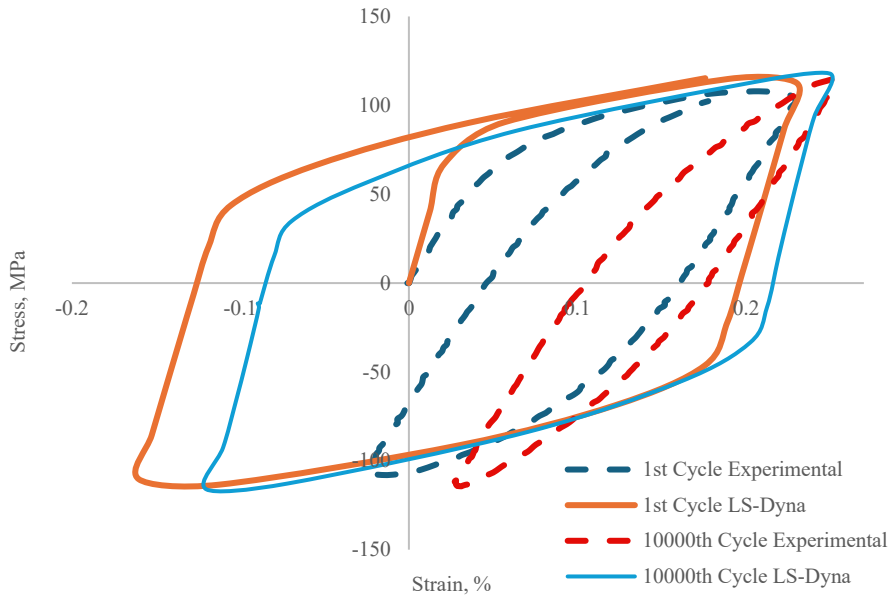


**Fig. 63.** Stress versus strain curve for  $r=2$  mm notched specimen at  $300^{\circ}\text{C}$

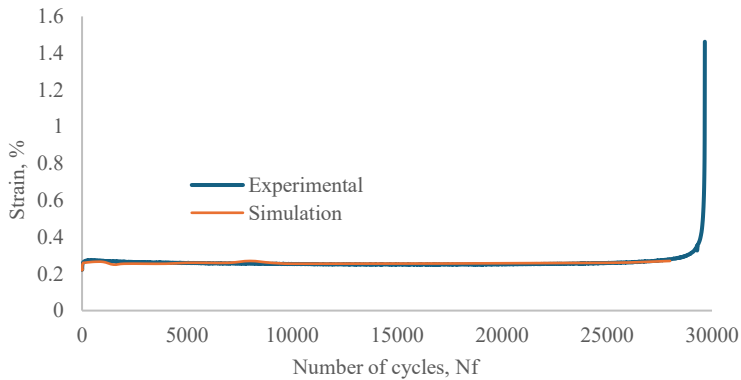


**Fig. 64.** Maximum stress v/s number of cycles for experimental and simulation  $r=2$  mm notched specimen at  $300^{\circ}\text{C}$

Figure 62 and Figure 64 consist of the maximum strain versus number of cycles curve for 0.5 mm and 2 mm radius notched specimen models. For both models, the maximum strain levels agree with the experimental results. The simulations were performed for about 15,000 cycles and 28,000 cycles for the 0.5mm and 2mm notched models; the simulation was not performed until the failure. Figure 60 and Figure 62 present the stress versus strain hysteresis loop. Figure 60 consists of the hysteresis loop for the 0.5 mm radius notched specimen model; the simulation results were close to the experimental results, but as the loading cycle reaches the third step, the curve is observed to be deviating a bit from the experimental curve. The simulation model

was able to capture the ratcheting behaviour of the material as it was observed in the experiment. Figure 63 consists of the hysteresis loop for the 2 mm radius notched specimen model. From the comparison of the simulation results with the experimental results, it was observed that the model stress versus strain curve was symmetric, unlike the experimental results, the reason being that the model was not able to capture the ratcheting behaviour as was observed in the experimental results. However, the simulation model closely matched the experimental results at the maximum strain level (Figure 64). Table 14 shows the maximum deviation between simulation and experimental results for all the experiments and simulation performed.

**Table 14.** Maximum deviation between simulation and experimental results for LCF tests

Test No.	1	2	3	4	5	6	7	8	9	10	11
<b>Specimen Type</b>	Solid								Hollow	Notched	
<b>Material</b>	AISI304L		AISI316L								
<b>Temperature, (°C)</b>	300		20	300	20	300	20	300	300	300	
<b>Strain amplitude, (%)</b>	0.3	0.6	0.18	0.6	0.5		1		0.3	-	-
<b>Kinematic hardening parameters estimated</b>	Using K.H model equation.							Using formulated relations.		Using K.H model equation.	
<b>Software</b>	ANSYS WB		LS-DYNA								
<b>Maximum error, (%)</b>	18.95	19.9	1.58	3.7	0.6	8.1	16	13	16	6.9	9.3

## 5.1. Chapter Conclusion

Low-cycle fatigue studies using numerical simulation methods are more economical and more applicable to various and complex conditions than experimental studies. Although numerical methods cannot completely replace experimental tests, they significantly improve the ability to predict fatigue behaviour, improve designs and reduce the need for detailed physical tests, especially in complex or aggressive environments.

Numerical studies were performed using the finite element computer programs ANSYS Workbench and LS-Dyna. The elastic-plasticity of the material was described using material models that evaluate kinematic and isotropic hardening during fatigue. It was found that the finite element mesh did not have a significant impact on low-cycle fatigue modelling. The models prepared for numerical simulation were validated by the results of experimental studies.

The computer program “ANSYS Workbench” was used to simulate the low-cycle fatigue of an AISI 304L stainless steel specimen at strain amplitudes of 0.3 and 0.6%. The results of the studies showed a significant deviation of the predicted results from the experimental results. The acceptable results were obtained only for the initial cycles, during which the stress amplitudes increase. The computer program “ANSYS” cannot accept the decreasing values for determining the isotropic hardening curve, due to which it cannot evaluate the decrease in material stresses; therefore, it is not possible to model the softening behaviour of the material that was observed in experimental studies.

The computer program LS-Dyna was used to numerically simulate the low-cycle fatigue of AISI 316L stainless steel. The Armstrong-Frederick material kinematic hardening method was used to evaluate the kinematic hardening parameters of the material, and a stabilised cycle was used to calibrate these parameters. Numerical simulations of low-cycle fatigue were performed under strain-controlled loading and at strain amplitudes of 0.18%, 0.5%, 0.6%, and 1%, as well as stress-controlled loading for specimens with 0.5 mm and 2 mm radius notches.

Equations were derived to determine the kinematic hardening parameters of AISI 316L stainless steel, which evaluate the effects of strain and temperature. These equations were validated by simulating a solid specimen at a strain amplitude of 1% and a hollow specimen at a strain amplitude of 0.3%. A low-cycle fatigue simulation using the LS-Dyna software was able to capture the cyclic hardening and softening behaviour of the material, and the numerical simulation results were very close to the experimental results.

The numerical simulation studies of low-cycle fatigue used kinematic hardening parameters, which were calculated using the derived equations, for AISI 316L stainless steel solid specimens at 1% strain amplitude and hollow specimens at 0.3% strain amplitude. The results of numerical simulation studies deviated from experimental studies by no more than 16% and found that the low-cycle kinematic hardening parameters of AISI 316L stainless steel can be used without additional calibration.

In the case of the stress-controlled LCF model for a notched specimen with the notched radius of 0.5 mm and 2 mm. The strain versus number of cycle curves was in agreement with the experimental results for both models. From the stress versus strain hysteresis loop for the 2 mm notched specimen model, it was observed that the model was unable to capture the ratcheting behaviour and the softening behaviour of the material due to force-controlled loading of the specimen, as the curve came out to be symmetric, which was not observed during the experimental investigation.

## CONCLUSIONS

1. In this work, an experimental study is carried out for low-cycle fatigue of AISI 304L and AISI 316L austenitic stainless steels at temperatures of 20°C and 300°C, under strain and stress-controlled loading. Solid, hollow and notched specimens were tested. The experimental program was prepared as per the requirements of ASTM E606/E606M and ASTM E1012. During the experimental study, kinematic hardening for the initial few cycles was observed, which was followed by cyclic softening of the material and finally specimen fracture. The low-cycle fatigue life of the specimens was highly influenced by the strain amplitude and operating temperature also had some degree of influence on the specimen failure cycle. In case of AISI 316L SS, for the increase in strain amplitude by 277.78% at same temperature, the failure cycle decreases by 98.36% and for temperature increase from 20°C to 300°C the failure cycle decreases by 9.88%. During the experimental studies of specimens with 0.5mm and 2mm radius notches under stress-controlled loading, material softening (ratcheting) was observed, as a result of which the stress-strain hysteresis was asymmetric, although the loads were symmetric.
2. The finite element method was used to model low-cycle fatigue for solid, hollow and 0.5 mm, and 2 mm radius notched specimens. The Armstrong-Frederick kinematic hardening rule was employed to describe the kinematic hardening of the material. The kinematic hardening parameters were estimated using a stabilised cycle. The isotropic hardening of the material was determined using a non-linear isotropic hardening model called the Voce model. In the case of the strain-controlled loading model, there was no significant effect of specimen length, and element size was observed on simulation results; therefore, a reduced specimen was used. A full-length specimen was modelled for the specimen with a notch, and fine mesh was used to model the notch zone to capture the stress concentration. The models used for low-cycle fatigue modelling were validated by the results of experimental studies.
3. The kinematic hardening during the low-cycle fatigue numerical simulation was described by employing the Armstrong-Frederick kinematic hardening model. The operating temperature and the strain amplitude both had some degree of influence on the kinematic hardening parameters. Out of which strain amplitude was dominating factor to affect the K.H parameters. As strain amplitude increases the K.H parameters decrease. The estimation of the kinematic hardening parameters is a complex process, and it requires an extra step to calibrate the parameters with experimental results, which is again a complex and time-consuming process. To reduce the complexity and time required to estimate the kinematic hardening parameters and to eliminate the process of calibration, relations between the kinematic hardening parameters, strain amplitude and operating temperature are derived. These relationships were used to estimate. Therefore, equations were derived to determine the kinematic hardening parameters of AISI 316L stainless steel, which evaluate the influences of

deformation and temperature. These equations were validated using the results of experimental studies. Using these equations, kinematic hardening parameters were calculated, which were directly used for low-cycle fatigue modelling without the calibration process, which shortened the evaluation time while maintaining the accuracy of the parameters. Low-cycle fatigue modelling using the LS-Dyna computer program allowed to capture the cyclic hardening and softening of the material, and the results of numerical modelling were very close to the experimental results. The results of low-cycle fatigue modelling using the calculated kinematic hardening parameters without calibration were confirmed by the results of experimental studies.

4. In the work, numerical modelling studies of low-cycle fatigue of AISI 304L and AISI 316L austenitic stainless steels were performed at 20°C and 300°C in air and at 300°C in a reactor environment, with strain-controlled and force-controlled loading on solid, hollow and notched specimens. The computer program “ANSYS” cannot accept the decreasing values for stress during defining isotropic hardening curve; therefore, it is not possible to model the softening behaviour of the material, as was observed in experimental studies. Due to this, “ANSYS Workbench” gave good results at the initial phase of hardening and followed by constant stress amplitude through out the simulation life with deviation of 19.9% with the experimental results. Therefore, the computer program LS-Dyna was used for the low-cycle fatigue simulation. Numerical simulation of the low-cycle fatigue of AISI 316L steels were performed at strain amplitudes of 0.18%, 0.5%, 0.6%, and 1%, while the simulations of the specimen with 0.5 mm and 2 mm radius notches were performed under stress control. The Armstrong-Frederick method of kinematic hardening of materials was used to evaluate the kinematic hardening parameters of the material. The deviation of the results of numerical simulation studies from experimental studies did not exceed 16%. It can be concluded that the prepared models can be used for predicting low-cycle fatigue durability under strain-controlled constant amplitude loading.

## **PROPOSAL FOR THE FUTURE**

The presented numerical simulation methodology can be applied to the strain-controlled constant amplitude with fully reversed loading. A hardening model of the material during LCF needs to be developed that can predict the material's behaviour for unsymmetrical and multiaxial loading cases.

In the case of the stress/force-controlled low cycle fatigue test, the material softening behaviour (ratcheting) occurs under fully reversed cycle loading, which might result from the tension–compression asymmetry. The hardening model of the material in the case of LCF needs to be modified so that it can fairly well predict the trend of accumulation of plastic deformation (ratcheting) for uniaxial and multiaxial loading cases.

## SANTRAUKA

### ĮVADAS

Konstrukcijos, eksploatuojamos aplinkai pavojingomis sąlygomis, dažnai patiria ilgalaikę jų paviršių degradaciją veikiant erozijai ir korozijai. Tai lemia skerspjūvio sienelės storio sumažėjimą, paviršiaus šiurkštumo padidėjimą, netolygumus, korozinių įdubų bei medžiagos stiprumo sumažėjimą [1], o tai turi įtaką šių konstrukcijų ilgaamžiškumui.

Aplinkos sąlygota degradacija ( angl. *Environmentally Assisted Fatigue*, EAF) yra būvis, galintis sutrumpinti komponentų eksploatacijos ilgaamžiškumą branduolinėse elektrinėse. Japonijoje, JAV, o vėliau ir Europoje atliktos bandymų programos parodė, kad vandens ir aplinkos poveikis šiose jėgainėse reikšmingai sumažina komponentų irimo trukmę ( $N_f$ ). Tačiau šiuo metu eksploatuojamų branduolinių jėgainių komponentų atsparumas aplinkos poveikiui nebuvo tiesiogiai įvertintas [5].

2015–2020 metais Europos Komisija inicijavo INCEFA-PLUS (Atominių elektrinių saugos didinimas užpildant aplinkos poveikio vertinimo spragas) projektą pagal H2020 programą. Šio projekto metu buvo atliekami mažo ciklo degradacijos / irimo ( angl. *Low Cycle Fatigue*, LCF) bandymai, įvertinant branduolinės elektrinės eksploatacijos sąlygas bei užtikrinant realią bandymų trukmę [5–7]. Pagrindinis projekto tikslas buvo ištirti, kaip degradacijos / irimo laikas ( $N_f$ ) kinta priklausomai nuo įvairių veiksnių: deformacijos diapazono ( skirtumo tarp didžiausios ir mažiausios deformacijos), vidutinės deformacijos, išlaikymo trukmės  $t_h$  esant vienodai deformacijai, bandinio paviršiaus šiurkštumo ( $R_t$ ) ir aplinkos sąlygų. Projekto metu įvairiose Europos laboratorijose buvo atlikta daugiau nei 250 degradacijos / irimo bandymų veikiant ir orui, ir vandeniui [5].

Naujausių užsienio mokslinių straipsnių ir tarptautinių projektų, skirtų cikliniam irimui tirti bei jų modeliavimo problemoms spręsti analizė rodo, kad baigtinių elementų metodai (BEM) suteikia galimybę aprašyti bei prognozuoti metalų būseną veikiant ciklinėms apkrovoms ir prognozuoti metalų ciklinį susidėvėjimą priklausomai nuo temperatūros ir laiko faktorių. Publikuoti tyrimų rezultatai „Clarivate Analytics“ duomenų bazėje sulaukė didelio mokslininkų dėmesio ( šaltinių sąrašas pateiktas priede).

Tačiau vis dar yra neišspręstų skaitmeninės interpretacijos klausimų įskaitant tuos, kurie susiję su degradacijos / irimo ciklą laiku, per kurį medžiaga turėtų suirti, taip pat plieno parametrų įvertinimu, apibūdinančiu medžiagos minkštėjimą / kietėjimą susidėvėjimo metu.

Vien kinematinio kietėjimo parametrų nustatymas skaitmeniniam prognozavimui, remiantis eksperimentiniais rezultatais, yra itin sudėtingas ir daug laiko reikalaujantis uždavinys. Be to, šie parametrai dažniausiai turi būti kalibruoti, kad modeliavimo rezultatai atitiktų eksperimentinius. Todėl būtina supaprastinti kinematinio kietėjimo parametrų įvertinimo procesą, kartu užtikrinant modeliavimo rezultatų patikimumą.

## Tikslai ir uždaviniai

Šio tyrimo tikslas – sukurti supaprastintą ir patikimą metodiką austenitinio nerūdijančiojo plieno kinematinį ir izotropinį grūdinimą lemiantiems medžiagų parametrams nustatyti, naudojant eksperimentinius mažo ciklo susidėvėjimo (LCF) bandymus ir baigtinių elementų (BE) modeliavimą. Metodologija leis patikimai nustatyti ciklinio grūdinimo / minkštėjimo būseną ir suteiks patvirtintą LCF charakteristikų prognozavimo galimybę, tiesiogiai palyginant skaitmeninius modeliavimus su eksperimentiniais rezultatais. Siekiant šio tikslo buvo išskelti šie uždaviniai:

1. sukurti išsamią eksperimentinę matricą, skirtą atlikti mažo ciklo degradacijos (LCF) bandymus su AISI 316L austenitiniu nerūdijančiu plienu esant deformacijos ir įtempio kontroliuojamam režimui, veikiant pastovios ir kintamos amplitudės apkrovai, siekiant gauti aukštos kokybės ciklinio įtempio ir deformacijos atsako bei nuovargio trukmės duomenis, kad būtų galima sukurti ir patvirtinti skaitmeninį modeliavimą;
2. sukurti baigtinių elementų modelį, gebantį užfiksuoti austenitinio nerūdijančio plieno ciklinį elastoplastinį ir kietėjimo / minkštėjimo būvį, laikantis kinematinio grūdinimo taisyklių ir kalibruojant modelio parametrus eksperimentiniais duomenimis;
3. sukurti supaprastintą ir atkartojamą AISI 316L nerūdijančio plieno grūdinimo ir minkštėjimo parametrų nustatymo metodiką siekiant sumažinti eksperimentinių rezultatų poreikį, kartu išlaikant apskaičiuotų parametrų tikslumą ir patikimumą;
4. atlikti mažo ciklo susidėvėjimo skaitmeninius modeliavimus ir patvirtinti sukurtų modelių rezultatus, palyginant modeliavimo rezultatus su atitinkamais eksperimentiniais rezultatais.

## Tyrimo metodai

Disertacijoje taikyti eksperimentiniai ir skaitinio modeliavimo tyrimų metodai. Eksperimentinių tyrimų rezultatai buvo naudojami modeliavimui siekiant nustatyti medžiagų parametrus mažo ciklo degradacijai įvertinti. Skaitmeniniam modeliavimui buvo naudojama programinė įranga „Ansys Workbench“, „LS-DYNA“, o 3D modeliavimui – „SolidWorks“. Eksperimentiniams darbams buvo naudojama bandymų mašina „Instron ElectroPlus E10000“ dinaminių-statinių bandymų tempimo-sukimo mašina (+/- 10KN tempimo galia, +/- 100 Nm sukimo galia, bandymų temperatūra -70– 350 °C). Teoriniai modeliavimo rezultatai buvo patikrinti eksperimentinių tyrimų rezultatais, atliktais Kauno technologijos universiteto Mechanikos inžinerijos katedroje, Lietuvos energetikos institute, „Electricity de France“ (EDF, Prancūzija) laboratorijose.

## **Mokslinis naujumas**

1. Pasiūlyta supaprastinta ir atkartojama AISI 316/316L austenitinio nerūdijančiojo plieno kinematinio grūdinimo parametrų nustatymo metodika, kurioje atsižvelgiama į darbinės temperatūros ir deformacijos amplitudės įtaką šiems parametrams ir sumažinamas eksperimentinių rezultatų reikalavimas, išlaikant modelio tikslumą.
2. Siūloma kinematinio grūdinimo parametrų nustatymo metodika pašalina poreikį papildomai kalibruoti šiuos parametrus pagal eksperimentinius rezultatus, siekiant užfiksuoti plieno elastoplastinį būvį, mažo ciklo degradaciją (LCF) modeliavimo metu, nes ši metodika leidžia patikimai prognozuoti kinematinio grūdinimo parametrus naudojant tik deformacijos amplitudės ir darbinės temperatūros duomenis.

## **Ginamieji teiginiai**

1. Tikslus austenitinių nerūdijančiojo plieno tampriųjų-plastinių ir ciklinių savybių prognozavimas skaitmeniniuose modeliuose iš esmės priklauso nuo tiksliai įvertintų izotropinių ir kinematinų grūdinimo parametrų. Šie parametrai lemia histerezės kilpos formą, vidutinio įtempio evoliuciją ir todėl daro įtaką mažo ciklo degradacijos / irimo trukmės prognozėms.
2. Kinematinio grūdinimo parametrų nustatymas naudojant įprastus metodus dažnai yra sudėtingas, daug laiko reikalaujantis ir labai priklausomas nuo išsamių eksperimentinių duomenų. Todėl reikia sukurti supaprastintą, greitą ir patikimą šių parametrų įvertinimo procedūrą, kartu sumažinant metodo priklausomybę nuo eksperimentinių rezultatų.
3. Baigtinių elementų analizė, naudojant kinematinis grūdinimo modelius, suteikia veiksmingą, efektyvią ir ekonomišką alternatyvą eksperimentiniams bandymams tiriant plieno mažo ciklo susidėvėjimo būseną.

## **Praktinė reikšmė**

1. Austenitinio nerūdijančiojo plieno mažo ciklo degradacijos būvį galima įvertinti naudojant siūlomą skaitmeninio modeliavimo metodiką, nereikalaujant eksperimentinių bandymų duomenų medžiagos parametrams įvertinti ir kalibruoti.
2. Kinematiniai grūdinimo parametrai, įvertinti naudojant suformuluotus ryšius tarp deformacijos amplitudės ir darbinės temperatūros, efektyviai atspindi plieno elastoplastinę būseną mažo ciklo susidėvėjimo metu, užtikrindama realų medžiagos atsaką skaitmeniniuose modeliavimuose.
3. Siūlomi kinematinų grūdinimo parametrų įvertinimo ryšiai supaprastina šių parametrų nustatymo procesą mažo ciklo susidėvėjimo metu, sumažina reikiamą bandymų skaičių ir kartu tyrimo laiką. Be to, taip pat sumažina poreikį atlikti

papildomą parametrų kalibravimą po jų nustatymo, todėl modeliavimo procesas tampa efektyvesnis ir tinkamesnis inžinerinėms reikmėms.

## **Tyrimo aprobavimas**

Tyrimo rezultatai buvo paskelbti 3 straipsniuose, išspausdintuose tarptautiniuose žurnaluose ir turinčiuose citavimo rodiklį (angl. *Impact Factor*) bei įtrauktuose į „Web of Science“ duomenų bazes.

Rezultatai taip pat buvo pristatyti 4 tarptautinėse konferencijose, 3 straipsniai publikuoti recenzuotuose konferencijų leidiniuose, įtrauktuose į „Web of Science“ duomenų bazes, o vieno pranešimo santrauka išspausdinta tarptautinės konferencijos tezėse.

## **Disertacijos struktūra**

Daktaro disertaciją sudaro įvadas, 5 skyriai ir bendrosios išvados. 1 skyriuje apžvelgiama mokslinė literatūra apie mažo ciklo degradaciją / irimą. Pateikta literatūros apžvalga apie degradacijos reiškinių, mažaciklio susidėvėjimo ypatumus, apžvelgiami tyrimai apie eksperimentinę mažo ciklo degradaciją ir skaitinį modeliavimą. 2 ir 3 skyriuose pateiktos eksperimentinio ir skaitinio modeliavimo metodologijos, kurios apima eksperimentinės matricos parengimą, baigtinių elementų modelio ir medžiagos modelio parengimą skaitiniui prognozuoti. 4 ir 5 skyriuose pateikiami eksperimentinių ir skaitinių modeliavimų rezultatai bei skaitinio prognozavimo rezultatų patvirtinimas eksperimentiniais rezultatais. Išvadose pateikiami eksperimentinių tyrimų ir skaitinio prognozavimo rezultatai. Pateiktas literatūros šaltinių sąrašas su 143 nuorodomis ir autoriaus mokslinių publikacijų sąrašu. Šią daktaro disertaciją sudaro 148 puslapiai, 119 paveikslai ir 26 lentelių.

## 1. LITERATŪROS APŽVALGA

Konstruktijos, eksploatuojamos aplinkai pavojingomis sąlygomis ir veikiant pasikartojančioms apkrovoms, patiria nuolatinį susidėvėjimą / irimą. Irimas – tai laipsniškas pažaidų kaupimasis elemente arba medžiagos bandinyje, kai jį veikia cikliška kintami įtempiai. Dėl cikliško įtempių kitimo elementuose, bandinio paviršiuje atsiranda plyšys, kuriam pasiekus kritinį didumą, konstrukcijos elementas staigiai lūžta. Irimą galima apibrėžti kaip apkrovos ciklų skaičių, kuriam esant pasiekiamas ribinis kriterijus. Priklausomai nuo ciklų skaičiaus, reikalingo komponentui suirti, įtakos tam turi ir pažaidų kaupimosi mechanizmas. Jei ciklų mažiau nei  $10^5$ , irimas vadinamas mažacikliu, o medžiagos savybė jam priešintis – mažacikliu stiprumu. Jei ciklų skaičius didesnis nei  $10^5$  – irimas daugiacykliškas. Irimas klasifikuojamas į daugiacykliškus, kai jis atsiranda dėl palyginti mažesnių įtempių lygių, taikomų per didelį ciklų skaičių (daugiau nei  $10^5$  ciklų iki suirimo) [2]. Konstrukcijos elemento arba bandinio savybė priešintis degradacijai vadinama patvarumu, kurio svarbiausias parametras – irimo riba. Tai įtempių ciklo, kurį konstrukcijos elementas arba bandinys nesuirdamas atlaiko neribotai daug kartų, didžiausias įtempis.

### 1.1. Mažo ciklo degradacija / irimas

Mažo ciklo degradacija / irimas (MCN) apibrėžiamas didele įtempių amplitude ir žemu dažniu [9, 10]. Mažacykliškas irimas yra susijęs su padidėjusiais įtempiais, viršijančiais takumo ribą ir didelėmis deformacijų amplitudėmis, dėl kurių kiekviename apkrovos cikle susidaro plastiškos deformacijos [9, 10]. Jei konstrukcijos elementas suyra dėl įtempių, viršijančių takumą ir plastinių deformacijų, esant ciklų skaičiui mažiau nei  $10^5$ , toks susidėvėjimas / irimas vadinamas mažacikliu, o medžiagos savybė jam priešintis – mažacikliu stiprumu. Disertacijos metu buvo atliekami mažacykliško irimo ( angl. *Low Cycle Fatigue*, LCF) bandymai, įvertinant branduolinės elektrinės eksploatacijos sąlygas bei užtikrinant realią bandymų trukmę. Lygiagrečiai eksperimentiniams tyrimams buvo atliekamas ir mažacykliško irimo prognozavimas panaudojant baigtinių elementų metodiką.

### 1.2. Austenitinis nerūdijantis plienas

Komponentai, kurie yra veikiami pasikartojančių apkrovų ir eksploatuojami pavojingomis sąlygomis aplinkoje, pavyzdžiui, esant aukštai temperatūrai ir slėgiui, yra gaminami iš austenitinio nerūdijančio plieno. Austenitinis nerūdijantis plienas yra plačiai naudojamas atominėse elektrinėse dėl išskirtinių mechaninių savybių, tokių kaip tįsumas, atsparumas aukštoje temperatūroje, todėl šias medžiagas palanku naudoti komponentams, veikiamiems aukštų temperatūrų. Austenitiniai nerūdijantys plienai 304L ir 316L pasižymi dideliu atsparumu korozijai, oksidacijai, taškinei korozijai ir pan. Todėl šie plienai plačiai naudojami komponentams, eksploatuojamiems pavojingomis aplinkos sąlygomis, pavyzdžiui, atominių elektrinių pirminiuose aušinimo kontūruose, kuriuose yra didelis slėgis ir aukšta temperatūra. Austenitinis AISI 316L plienas pasižymi stabiliomis savybėmis neutronų



modelių, galinčių atlikti anksčiau aptartus reiškinius, kūrimas ir efektyvi šių modelių integracija į plačiai naudojamus baigtinių elementų kodus, tokius kaip „ABAQUS“, „ANSYS“ ir „LS-DYNA“, yra būtini norint tiksliau įvertinti reaktorių ir kitų saugai svarbių komponentų struktūrinį vientisumą [38]. Dėl didelės ciklinės plastinės deformacijos veikiant ciklinėms apkrovoms, taip pat būvio sudėtingumo naudojant dabartinius skaitinius modelius yra sudėtinga tiksliai atvaizduoti eksperimentuose stebimą ciklinį plastiškumą. Metalų ciklinis plastiškumas yra labai sudėtingas, todėl reikia atlikti daug skaičiavimų norint atlikti eksperimentinius bandymus, kad būtų galima nuodugniai ištirti kaip ciklinis medžiagos kietėjimas ar minkštėjimas, taip pat progresyvi deformacija (didėjanti netamprioji deformacija) atsiranda dėl kiekviename cikle vykstančios plastinės deformacijos.

#### 1.4. Mažaciklio irimo tyrimų apžvalga

Meng'o ir kt. [40] tyrime buvo nagrinėjama kaip temperatūra ir deformacijos greitis veikia austenitinio nerūdijančio plieno mažo ciklo patį irimo procesą. Facheris ir Janssens'as [41] atliko nerūdijančio plieno 316 bandymų esant kambario ir 200 °C temperatūroms, kad nustatytų, kaip deformacijos amplitudė ir temperatūra veikia mažo ciklo irimą. Chen'as ir kt. [42] atliko modifikuoto 9Cr-1Mo plieno su 0,38 % ir 1,2 % silicio mažaciklio irimo tyrimus esant 450 °C temperatūrai [43].

Savo tyrime Yang'as, H. ir kt. [60] atliko mažaciklės degradacijos / irimo bandymus kontroliuodami apkrovą pagal deformaciją ir esant vienodai amplitudei, kad sukalibruotų plieno *Chaboche* kinematinio grūdinimo parametrus. Zhang'as ir kt. [61] atliko eksperimentinį plieno P92 mažo ciklo irimo charakteristikų tyrimą kambario temperatūroje ir lygiagrečiai naudojo skaitinį modeliavimą, kurio metu buvo įvertinti ir sukalibruoti izotropiniai ir kinematiniai grūdinimo parametrai. Han, J. ir kt. [62] atliko skaitinį *Chaboche* kinematinio grūdinimo modelio įgyvendinimą naudodami vartotojo apibrėžtą medžiagos modelį. Shiva ir kt. [66] atliko modifikuotos P91 plieno plokštės ant plokštės kontakto eksperimentinius ir skaitininio modeliavimo tyrimus, taikydami maksimalius 450 MPa, 500 MPa ir 550 MPa ciklinius įtempimus, o įtempių santykis buvo 0,3.

Zhu P ir kt. [69] pasiūlė kietėjimo funkciją ir ištyrė veiksnius, turinčius įtakos kietėjimo procesui. H. Mahbadi ir MR Eslami [70] panaudojo *Pragerio* ir *Armstrong-Frederick* kinematinius kietėjimo modelius, kad ištirtų ciklinio apkrovimo poveikį. Li-Yan ir kt. [71] atliko BLY160 plieno eksperimentinius ir skaitinio modeliavimo tyrimus, siekdami ištirti plieno ciklinį minkštėjimą ir kietėjimą. Jie suformulavo tampriai plastinį konstitutyvų modelį, pagrįstą kombinuotais izotropiniais ir kinematiniais kietėjimo modeliais. Suformuluotas konstitutyvusis modelis buvo išbandytas naudojant jį skaitiniam modeliavimui, kartu lyginant prognozavimo rezultatus su eksperimentiniais. Moeini G ir kt. [73] atliko eksperimentinius ir skaitinius dvifazio plieno mažaciklės degeneracijos tyrimus. Stabilizuota histerezės kilpa buvo modeliuojama naudojant mikromechaninio modeliavimo metodus.

Z. Wang'as ir kt. [74] parengė baigtinį elementą / modelį irimo įtrūkimų didėjimui prognozuoti, remdamiesi Gauso teorijos teoriniais pagrindais, patvirtintais SCM435 medžiagos eksperimentiniais rezultatais. M. A. Meggiolaro ir J. T. P. Castro

[75] atliko plieno 724 eksperimentinius tyrimus, skirtus Coffin-Manson'o modeliui įvertinti. L. Gardner'is ir D. Nethercot'as [76] pateikė tuščiavidurių bandinių nerūdijančio plieno skaitinio modeliavimo tyrimą konstrukcijos atsako ciklinėms apkrovoms nustatyti. G. Dundulis ir kt. [4] pateikė P91 plieno mažaciklės degeneracijos veiksmų prognozavimo skaitiniui, naudojant baigtinių elementų modelį, tyrimus. Baigtinių elementų modelio validavimui ir medžiagos parametru kalibravimui buvo atlikti mažo ciklo degradacijos, apkrovą kontroliuojant pagal deformacijas, bandymai 550 °C temperatūroje. A. Dutta ir kt. [82] pateikė AISI316L nerūdijančio plieno mažaciklio susidėvėjimo / irimo prognozes panaudodamas baigtinių elementų metodiką (kompiuterinė programa *ABAQUS*). Reikalingi parametrai buvo įvertinti pagal mažaciklio susidėvėjimo / irimo eksperimentinius duomenis kambario temperatūroje. R. Janulionis ir G. Dundulis [83] tyrė 9Cr-1Mo plieno suvirintų bandinių mažaciklę degeneraciją esant 550 °C temperatūrai. Pateikti eksperimentiniai ir skaitmeniniai tyrimų rezultatai. Visuose pateiktuose straipsniuose naudotas medžiagų kinematinio kietėjimo *Chaboche* modelis.

Atlikus mažaciklio susidėvėjimo / irimo tyrimų apžvalgą nustatyta, kad degeneracijos prognozavimo patikimumas priklauso nuo medžiagų parametru, įvertinančių medžiagų kinematinį ir izotropinį kietėjimą ciklinio apkrovimo metu. Medžiagų parametru įvertinimo procesas priklauso nuo parametru kalibravimo naudojant eksperimentinius duomenis. Todėl reikia didelį dėmesį skirti kinematinų ir izotropinių kietėjimo parametru įvertinimo procedūroms, kad būtų galima sumažinti šių parametru įvertinimo ir kalibravimo sudėtingumą ir trukmę. Tokie darbai yra būtini norint išspręsti iššūkius, su kuriais susiduriama taikant įvertintus kietėjimo parametrus baigtinių elementų modeliavimo programose ir patikimai prognozuoti bandinius pradinių ciklu metu.

## 2. EKSPERIMENTINĖ METODOLOGIJA

Eksperimentiniai austenitinio nerūdijančio plieno mažaciklės degradacijos tyrimai yra aktualūs nustatant medžiagų irimą / susidėvimą realiomis darbo sąlygomis ciklinio apkrovimo metu. Eksperimentiniai tyrimai svarbūs nustatant konstrukcijų saugią eksploataciją ir ilgaamžiškumą, tai taip pat svarbu ir taikant skaitmenio prognozavimo modelius.

Mažaciklės degradacijos eksperimentai atlikti AISI316L austenitinio nerūdijančio plieno, kuris naudojamas atominėse elektrinėse. Patikimas konstrukcijos ir komponentų valdymas yra labai svarbus saugiam šių konstrukcijų eksploatavimui. Eksperimentiniai šių konstrukcijų bandymai saugiam jų eksploatavimui yra labai svarbūs. Tačiau kai kuriais atvejais eksperimentinių bandymų atlikimas realiomis eksploataavimo sąlygomis yra labai sudėtingas ir brangus. Reikia paminėti, kad susidėvėjimo kreivių nustatymas yra brangus, užima daug laiko ir yra sunkiai įgyvendinamas eksperimente, ypač reaktoriaus aplinkoje (aukšta arba žema temperatūra, rūgštinė arba šarminė aplinka ir kt.). Paprastai laboratorinių degradacijos bandymų metu gauti duomenys netiksliai atspindi gamykloje atliktus stebėjimus. Skaitinio modeliavimo metodai yra naudojami konstrukcijų stiprumui įvertinti esant skirtingoms apkrovoms. Todėl lygiagrečiai bandymus atliekant ore, vienam bandymui buvo pasirinkta PWR (slėginio vandens reaktoriaus) aplinka. Šis eksperimentas buvo atliktas EDF (pranc. *Électricité de France*) įrenginyje [7]. Šiame darbe taip pat analizuojami AISI 304L ir AISI 316L nerūdijantys plienai, tačiau AISI 304L plienas tik oro sąlygomis.

Šiame skyriuje pateikti standartai, taikyti šios disertacijos tema susijusiems eksperimentiniams tyrimams, bandiniams paruošti ir bandymų įrangai kalibruoti. Šiame skyriuje taip pat aprašomas bandinio projektas ir eksperimento matrica. Eksperimentai atlikti remiantis *ASTM E 606/ E606M standartu* ir *ASTM E 1012*.

### 2.1. Eksperimentinių tyrimų standartai

Norint tinkamai įvertinti susidėvimą / irimą eksperimentiniu metodu, svarbu remtis šiam tikslui paskelbtais standartais. Yra keletas standartų, skirtų skirtingiems susidėvėjimams / irimui vertinti. Standartais remiamasi siekiant pašalinti eksperimento proceso klaidas ir surinkti eksperimento rezultatus. Šiame tyrime eksperimentams planuoti naudojami *ASTM E 606/ E606M* [29] ir *ASTM E 1012* [30] standartai.

### 2.2. Austenitinis plienas

Austenitinis nerūdijantis plienas pasižymi geromis savybėmis, susijusiomis su deformaciniu kietėjimu, tūsumu ir konstrukciniu stiprumu [86]. Nerūdijantis plienas plačiai taikomas įvairiuose pramonės komponentuose – nuo energetikos sektoriaus iki biomedicinos. Labai svarbu suprasti medžiagos ciklinio plastiškumo būvį, ypač esant mažaciklei deformacijos apkrovai (LCF) [95].

**15 lentelė.** AISI 304L ir AISI 316L nerūdijančio plieno cheminė sudėtis (wt %) [103]

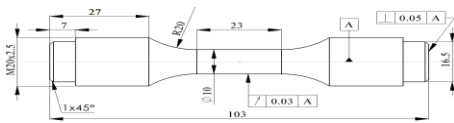
	C	Si	Mn	P	S	N	Cr	Mo	Cu	Ni	Fe
AISI 304L	0,029	0,75	1,86	0,045	0,03	0,1	18	0,04	0,02	10	69,126
AISI 316L	0,026	0,42	1,81	0,033	0,004	0,05	16,96	2,43	0,03	12	66,237

316 austenitinis nerūdijantis plienas plačiai naudojamas įvairių tipų branduoliniuose reaktoriuose, įskaitant esamas branduolines elektrines ir naujos kartos pažangias reaktorių koncepcijas, tokias kaip natriu aušinami greitieji reaktoriai, išlydytos druskos reaktoriai ir dujomis aušinami aukštos temperatūros reaktoriai. 304L ir AISI 316L nerūdijančio plieno cheminė sudėtis pateikta 15 lentelėje.

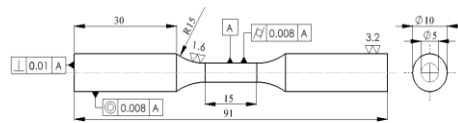
### 2.3. Bandinių konstrukcija

Mažaciklio susidėvėjimo bandiniai buvo suprojektuoti pagal ASTM E606 / E606M [90] reikalavimus ir rekomendacijas. Kiekvienai eksperimento schemai buvo paruošta keletas bandinių. Eksperimentai buvo atlikti su pilnaviduriais bandiniais, tuščiaviduriais bandiniais ir bandiniais su įpjovomis.

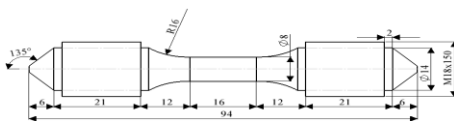
Nerūdijančio plieno AISI 304L ir 316L cilindriniai pilnaviduriai bandiniai, skirti mažo ciklo susidėvėjimo eksperimentams atlikti, buvo suprojektuoti remiantis standarto [90] reikalavimais. Išsamios visų atliktų eksperimentų bandinių geometrijos pateiktos 66–70 paveiksluose.



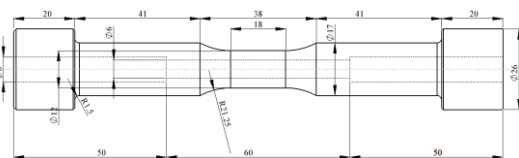
**66 pav.** AISI 304L plieno pilnaviduris bandinys, naudotas 0,3 ir 0,6 % deformacijos amplitudei



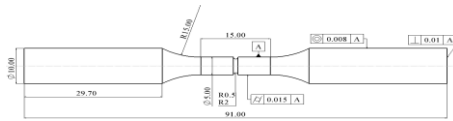
**67 pav.** AISI316L plieno pilnaviduris bandinys, naudotas 0,18 % ir 0,6 % deformacijos amplitudei



**68 pav.** AISI 316L plieno bandinys, pilnaviduris bandinys, naudotas 0,5 ir 1 % deformacijos amplitudei



**69 pav.** AISI 316L plieno tuščiaviduris bandinys, naudotas 0,3 % deformacijos amplitudės bandymui PWR aplinkoje 300 °C temperatūroje



**70 pav.** AISI 316L plieno bandinys su įpjova, kurio įpjovos spindulys yra 0,5 ir 2 mm, 300 °C temperatūroje, kontroliuojant pagal įtempius

66 pav. parodytas bandinio brėžinys, naudotas atliekant mažaciklės degradacijos bandymą 300 °C temperatūroje, kai deformacijos amplitudės yra 0,3 % ir 0,6 %. Bandinys pagamintas iš AISI 304L nerūdijančio plieno plokštės.

Dar du eksperimentai atlikti su pilnaviduriais bandiniais, pagamintais iš AISI316L nerūdijančio plieno. Eksperimentai atlikti esant 0,18 % deformacijų amplitudei 20 °C temperatūros aplinkoje ir 0,6 % esant 300 °C temperatūrai. Kieto AISI316L nerūdijančio plieno pilnavidurio bandinio brėžinys pateiktas 67 pav.

Keturi eksperimentai, kuriuose buvo tiriama AISI 316L nerūdijančio plieno mažaciklė deformacija naudojant pilnavidurius bandinius, buvo atlikti oro aplinkoje, esant 20 °C ir 300 °C temperatūroms, o apkrovos buvo kontroliuojamos pagal deformaciją. Be pilnavidurių bandinių, mažaciklio susidėvėjimo bandymai taip pat buvo atlikti naudojant AISI 316L nerūdijančio plieno tuščiavidurius bandinius PWR aplinkoje. 68 ir 69 paveiksluose pateikti šiems bandymams naudoti pilnavidurių ir tuščiavidurių bandinių brėžiniai.

Siekiant nustatyti įpjovos poveikį AISI316L nerūdijančio plieno mažo ciklo degradacijai, buvo atlikti mažaciklės degradacijos eksperimentai naudojant bandinius su įpjovomis. 70 paveiksle pateiktas naudoto bandinio su įpjovomis brėžinys.

#### **2.4. Eksperimentinės sąlygos**

Mažo ciklo degradacijos bandymai buvo atlikti su kelių tipų bandiniais: pilnaviduriais ir tuščiaviduriais poliruotais bandiniais ir pilnaviduriais bandiniais su įpjovomis. Eksperimentiniai tyrimai buvo atlikti oro sąlygomis esant kambario, 20 °C, reaktorių eksploatacijos ir 300 °C temperatūroms, apkrovos kontroliuojant pagal deformacijas ir pagal įtempius. Eksperimentiniai tyrimai buvo atlikti ir branduolinio reaktoriaus (slėginio vandens reaktoriaus (PWR) tipo) aplinkoje. Eksperimentiniams tyrimams reaktoriaus aplinkoje atlikti reikalinga specializuota įranga, kurios Lietuvoje nėra, todėl eksperimentiniai tyrimai šioje aplinkoje buvo atlikti Prancūzijoje, EDF laboratorijoje. Darbe buvo naudoti EDF laboratorijos eksperimentiniai rezultatai degradacijos modeliavimo, įvertinančio reaktoriaus aplinkos sąlygas, patvirtinimui.

Prieš atliekant eksperimentinius mažo ciklo degradacijos bandymus, bandinių fiksavimo ašiškumas buvo reguliuojamas pagal ASTM E1012 [96] reikalavimus. Reguliavimas buvo atliekamas atsižvelgiant į bandinio lenkimo deformacijos kriterijus, t. y. didžiausia leidžiama lenkimo deformacija neturėjo būti didesnė kaip 5 % [40].

**16 lentelė.** Eksperimentinio tyrimo matrica bandiniams be įpjovų

<b>Bandymo Nr.</b>	1	2	3	4	5	6	7	8	9 (EDF bandymas)
<b>Bandinio tipas</b>	pilnaviduris be įpjovos								Tuščiaaviduris
<b>Medžiaga</b>	AISI304L		AISI316L						
<b>Bandymo valdymas</b>	Kontroliuojama pagal deformacijas								
<b>Deformacijos amplitudė (%)</b>	0,3	0,6	0,18	0,6	0,5		1		0,3
<b>Temperatūra (°C)</b>	300		20	300	20	300	20	300	300
<b>Apkrovimo tipas</b>	Pastovios amplitudės kintamasis apkrovimas su nuline vidutine deformacija. $R = -1$								
<b>Aplinka</b>	Oras								PWR

Mažo ciklo degradacijos bandymas su vientisu nerūdijančio plieno AISI 304L bandiniu buvo atliktas naudojant „Instron 8801 servo“ hidraulinio bandymo mašiną su  $\pm 100$  kN dinaminio apkrovos elementu. LCF bandymui aukštoje temperatūroje atlikti buvo naudojami atvirkštinio įtempimo strypai. Bandiniui pritvirtinti buvo naudojamas srieginis bandinio adapteris. Bandinio koncentriškumas ir kompaktiškumas buvo sureguliuoti naudojant srieginę lygiavimo celą „AignPRO“. Ant bandinio buvo sumontuoti K tipo termoelementai temperatūrai matuoti. Viso eksperimento metu buvo palaikoma vienoda temperatūra, ne didesnės kaip numatyta 1–2 °C paklaidos. Eksperimentinio bandymo metu deformacijai matuoti buvo naudojamas „Instron 2632“ serijos aukštos temperatūros ekstensometras [38].

1–9 eksperimentiniai bandymai buvo atlikti apkrovas kontroliuojant pagal deformacijas. O 10–11 eksperimentai buvo atlikti apkrovas kontroliuojant pagal įtempius.

Eksperimentiniams bandymams buvo naudojama elektromechaninė tempimo-sukimo mašina *INSTRON E10000*, kurios maksimali tempimo jėga yra 10 kN, o sukimo galia – 100 Nm. Eksperimentiniams tyrimams naudoti bandiniai yra pateikti 2.3 skyriuje. Siekiant užtikrinti tinkamą bandinio centravimą, tempimo mašinos *INSTRON E10000* apatinio griebto fiksavimas buvo modifikuotas pritvirtinant centravimo flanšą ir naudojant keturis reguliavimo varžtus. Bandinio centriškumas reguliuojamas matuojant bandinio deformacijas, naudojant deformacijų daviklius, pritvirtintus prie tempiamo bandinio. Įtempimo daviklių signalai buvo prijungti prie kompiuterio per „National Instruments“ duomenų rinkimo sistemą *NI CDAQ-9188* ir apdoroti *MATLAB* programoje.

**17 lentelė.** Įpjovos bandinio eksperimento matrica

<b>Bandymo Nr.</b>	10	11
<b>Bandinio tipas</b>	Pilnaviduris su įpjova	
<b>Medžiaga</b>	AISI316L	
<b>Įpjovos spindulys (mm)</b>	0,5	2
<b>Bandymo valdymas</b>	Kontroliuojama pagal įtempius	
<b>Didžiausia taikoma jėga, (N)</b>	2447	8908
<b>Temperatūra (°C)</b>	300	
<b>Apkrovimo tipas</b>	Kintamos amplitudės (laipsniškas apkrovimas) apkrovimas su nuliniiais vidutiniais įtempiais, $R = -1$	Pastovios amplitudės kintamasis apkrovimas su nuliniiais vidutiniais įtempiais. $R = -1$
<b>Aplinka</b>	Oras	

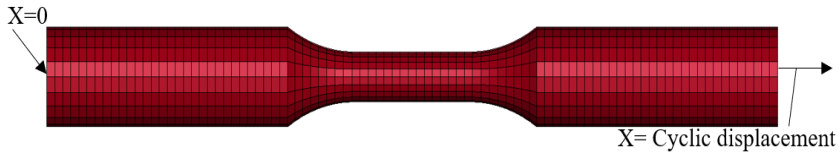
Terminėje kameroje bandymai buvo atliekami 300 °C temperatūroje. Bandinio deformacijos buvo matuojamos ant bandinio pritvirtintu aukštatemperatūriu „Epsilon“ gamintojo ekstensometru 7642-010M-025SM-TD. Atliekant eksperimentinius bandymus, bandinių su įpjovomis deformacijos pleišėjimui fiksuoti ir deformacijoms matuoti per terminės kameros langą buvo naudojama 3D skaitmeninio vaizdo koreliacijos (DIC) sistema su dviem „Basler acA4112-20µm“ kameromis „Correlated Solutions“ gamybos. DIC kameromis užfiksuoti bandinių vaizdai buvo apdoroti *VIC-3D* programoje.

### 3. SKAITMENINIO MODELIAVIMO METODOLOGIJA

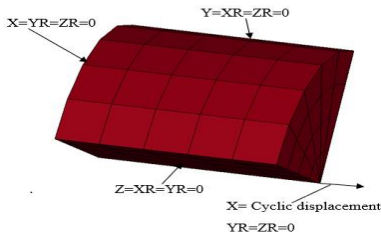
Dėl savo patikimumo, ekonomiškumo ir galimybės atlikti išsamią analizę įvertinant pavojingas eksploataavimo sąlygas, skaitmeninis modeliavimas pastaruoju metu tapo svarbiu metodu mažo ciklo degradacijai prognozuoti. Taip pat yra galimybė prognozuoti susidėvėjimo trukmę realiomis ir sudėtingomis eksploataavimo sąlygomis. Prognozuojant komponentų būseną, ją veikiant mažo ciklo degradacijos apkrovoms, modeliuojamas medžiagos ciklinis tampriai plastinis būvis iki stabilizavimosi, kuris paprastai įvyksta esant pusei ciklų iki suirimo [97]. Šiame tyrime atliekamas skaitmeninis mažo ciklo degradacijos modeliavimas siekiant ištirti austenitinio nerūdijančio plieno tampriai plastinę būseną. Šiame skyriuje paaiškinamas parengtas baigtinių elementų modelis mažo ciklo degradacijai prognozuoti, taikytos apkrovos sąlygos, ribinės sąlygos ir medžiagų modeliavimas.

### 3.1. Mažo ciklo degradacijos modeliavimo modelis

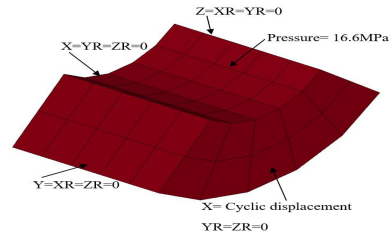
Mažo ciklo degradacijai modeliuoti naudota baigtinių elementų metodika. Modeliavimui paruošti baigtinių elementų modeliai pateikti 71–74 paveiksluose. Kaip minėta anksčiau 2.2 skyriuje, šiame tyrime buvo tiriami kelių tipų bandiniai, t. y. pilnaviduriai, tuščiaviduriai ir su įpjova. Skaitmeniniam modeliavimui buvo paruoštas bandinio baigtinių elementų modelis, kuris pateiktas 71 pav. Kadangi bandinys yra simetriškas, todėl mažo ciklo irimo prognozavimui buvo paruoštas 1/4 bandinio dalies baigtinių elementų modelis.



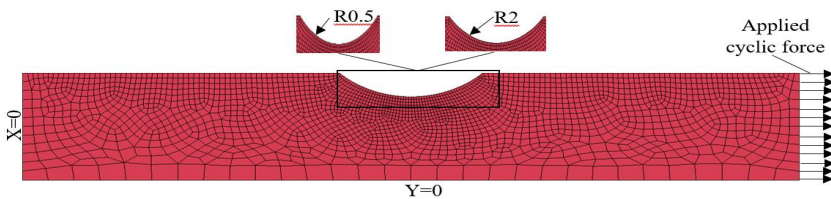
71 pav. Pilnas baigtinių elementų (BE) modelis su pritaikytomis ribinėmis sąlygomis



72 pav. Taikytos kraštinės sąlygos redukuotam baigtinių elementų modeliui



73 pav. Tuščiavidurio bandinio tinklinis baigtinių elementų modelis su pritaikytomis ribinėmis sąlygomis



74 pav. Tinklinis baigtinių elementų modelis su įpjautam bandiniui pritaikytomis ribinėmis sąlygomis

Mažo ciklo degradacijos bandymai buvo vykdomi apkrovą kontroliuojant pagal deformacijas. Modeliuojant bandinio būvį mažo ciklo degradacijos metu, bandinio modelio priekinio paviršiaus judesys buvo kontroliuojamas pagal deformacijas. Taikytos ribinės sąlygos parodytos 8 paveiksle.

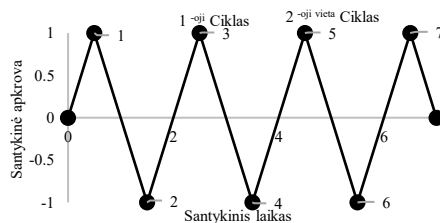
AISI 304L nerūdijančio plieno, kurio deformacijos amplitudė yra 0,3 % ir 0,6 %, mažo ciklo deformacijos modeliavimas atliktas naudojant „Ansys Workbench“. Bandinys buvo modeliuojamas naudojant „ANSYS\_SOLID185“ elementus – tai 8

mazgų elementas su trimis laipsniais kiekvienam mazgui. AISI 316L nerūdijančio plieno, kurio deformacijos amplitudė yra 0,18 %, 0,6 %, 0,5 % ir 1 %, modeliai buvo parengti naudojant „LS-DYNA“ programinę įrangą. Pilnaviduriams (72 pav.) ir tuščiaaviduriams bandiniams (73 pav.) modeliuoti buvo naudojami konstantinių įtempių 8 mazgų heksaedriniai elementai. Visais atvejais bandinių apkrovos buvo pridėtos prie priekinio paviršiaus kontroliuojant pagal deformacijas (72 ir 73 pav.). Tuščiaaviduriuose bandiniuose buvo įvertintas vidinis paviršius ir vidinis slėgis, susidarantis vamzdynuose reaktorių eksploatacijos metu (73 pav.).

Bandinių su įpjovomis baigtinių elementų modelis buvo parengtas naudojant 2D elementus. Naudojant abu šiuos modelius buvo atliktas pirmojo ciklo modeliavimas naudojant 0,3 % deformacijos amplitudės apkrovą, nes buvo siekiama išanalizuoti bandinio dydžio įtaką skaitmeninio modeliavimo rezultatams. Bandinys buvo sumodeliuotas naudojant 4 mazgų keturkampį apvalkalo elementą su „Belytschko-Tsay“ formuluote. Paveikslėlyje (74 pav.) pateiktas paruoštas baigtinių elementų modelis ir jam taikomos kraštinės sąlygos. Šiems modeliams buvo naudojamas smulkus tinklelis siekiant įvertinti įtempių koncentraciją, susidarantią įpjovoje. Taip pat, skirtingai nei kituose modeliuose, dėl simetriškumo buvo paruoštas 1/2 bandinio, viso ilgio modelis. Paruošti du skirtingi modeliai, kurių vienas su 0,5 mm įpjovos spinduliu, o kitas su 2 mm įpjovos spinduliu. Bandinių apkrovos buvo pridėtos prie priekinio paviršiaus kontroliuojant pagal įtempius (74 pav.).

### 3.2. Mažo ciklo degradacijos modeliavimui naudotos apkrovos

Mažo ciklo deformacijos eksperimentiniai bandymai pagal apkrovos pobūdį buvo dviejų tipų, t. y. apkrovas kontroliuojant pagal deformacijas ir pagal įtempius. Analogiškos apkrovos buvo naudojamos ir mažo ciklo deformacijoms modeliuoti. Skaitmeninio modeliavimo metu bandinio apkrovai buvo naudojamas poslinkis, kontroliuojant bandinio apkrovą pagal deformacijas. Poslinkio amplitudė buvo tokia pati kaip ir eksperimento deformacijos amplitudė.

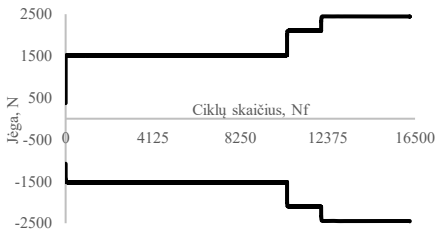


75 pav. Santykinė deformacija pritaikyta baigtinių elementų modeliui, kai schema valdoma deformacija

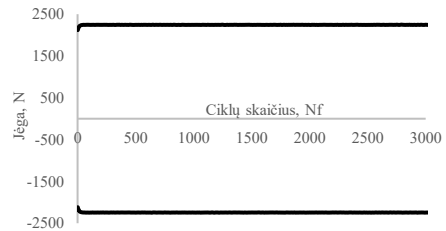
Bandiniai buvo apkrauti ašine kryptimi, pridėdant apkrovą prie vieno bandinio paviršiaus, o kito paviršiaus poslinkis buvo fiksuojamas pagal visas koordinacinių ašis. Santykinis bandinių apkrovimas pateiktas 75 pav. Pirmasis ciklas prasideda nuo 0 taško (75 pav.), kai bandinys yra ramybės būsenos. Pirmojo ciklo metu jis yra padalintas į tris dalis: pirmasis taškas (0–1) yra pusė tempimo dalies, po kurios vyksta

gnuždymo ciklas iki taško 2 (nuo 1 iki -1) ir vėl tempimo ciklas iki taško 3 (nuo -1 iki 1). Tai užbaigia pirmąjį ciklą, o antrasis ciklas vyksta nuo taško 3 iki taško 5 (1, -1, 1) ir taip toliau iki prognozuojamo bandinio menamo nutrūkimo.

Mažo ciklo degradacijos bandymo schemeje, kurioje apkrova kontroliuojama pagal deformacijas, deformacijos amplitudės buvo  $\pm 0,18\%$ ,  $\pm 0,3\%$ ,  $\pm 0,5\%$ ,  $\pm 0,6\%$  ir  $\pm 1\%$ . Todėl 1 ir -1 atitinkamai atitinka deformacijos amplitudę teigiama ir neigiama kryptimis. Norint modeliuoti apkrovas jas kontroliuojant pagal deformacijas kaip ir eksperimentų metu, bandiniai buvo apkraunami poslinkiu, atitinkančiu deformacijų amplitudes (pvz., kai deformacijos amplitudė yra  $\pm 1\%$ , o bandinio modelio ilgis – 10 mm, modeliui taikoma  $\pm 0,1$  mm poslinkio amplitudė).



**76 pav.** Apkrova, taikyta baigtinių elementų modeliui, kai bandinys su įpjova,  $r = 0,5$  mm



**77 pav.** Apkrova, taikyta baigtinių elementų modeliui, kai bandinys su įpjova,  $r = 2$  mm

Modeliuojant mažo ciklo deformacijos būvį, kai apkrova buvo kontroliuojama pagal įtempius, bandinių apkrovos buvo pridėdamos analogiškai, kaip ir kontroliuojant apkrovas pagal deformacijas (74 ir 75 pav.). Pagal įpjovos spindulį buvo du skirtingi bandiniai, t. y. 0,5 mm ir 2 mm. Bandinių su įpjova eksperimentiniai tyrimai atlikti apkrovą kontroliuojant pagal įtempius. Jėga buvo pridėta prie bandinio galinio paviršiaus (74 pav.). Jėgos dydis eksperimentiniams tyrimams buvo parinktas pagal tikslią deformaciją bandinio įpjovos gale. Bandiniui su 0,5 mm spindulio įpjova, mažo ciklo deformacijos eksperimentiniai tyrimai buvo atlikti pridėdamas jėgą trimis apkrovimo etapais, kad tiksli deformacija įpjovos gale būtų atitinkamai 0,2 %, 0,4 % ir 0,6 %. Bandinys su 2 mm spindulio įpjova buvo išbandytas esant pastovios amplitudės jėgai, kai tiksli deformacija įpjovos gale buvo 0,6 %. Kaip minėta anksčiau, bandiniui su 0,5 mm įpjovos spinduliu apkrova buvo taikoma trimis etapais (76 pav.), t. y. 1520 N jėga (atitinka 0,2 % deformaciją) apkraunama iki 10445 ciklų, tada apkrovos jėga didinama iki 2100 N (atitinka 0,4 % deformaciją) ir galiausiai po 12065 ciklų, apkrovos jėga padidinama iki 2445 N (atitinka 0,6 % deformaciją). Bandinys su 2 mm spindulio įpjova buvo apkraunamas vieno etapo metu 2245 N jėga (atitinka 0,6 % deformaciją) (77 pav.) iki prognozuojamo suirimo.

### 3.3. Medžiagų modeliai

Norint tinkamai įvertinti komponento mažo ciklo degradacijos trukmę, svarbu realistiškai modeliuoti medžiagos ciklinį plastiškumą. Plastinė deformacija yra negrįžtama deformacija, atsirandanti, kai įtempis pasiekia medžiagos takumo ribą [98–102]. Darant prielaidą, kad plastinės deformacijos atsiranda nepriklausomai nuo

laiko, egzistuoja įvairių teorijų, skirtų medžiagų reakcijoms įvertinti ciklinės deformacijos metu. Plastiškumo teorija išskiria tris pagrindinius komponentus: takumo kriterijų, takumo taisyklę ir medžiagos (kietėjimo) modelius [98–102]. Šiame tyrime kinematinis kietėjimas naudojamas kartu su izotropiniu grūdinimu, siekiant modeliuoti medžiagos būvį ciklinės deformacijos metu panaudojant baigtinių elementų metodiką.

**18 lentelė.** Austenitinio nerūdijančio plieno mechaninis savybės

Kiekis	Simbolis	Vienetai	Vertybės		
Medžiaga			AISI304L	AISI316L	
Temperatūra	$T$	°C	300	20	300
Tankis	$\rho$	kg/m <sup>3</sup>	7930	7980	
Youngo modulis	$E$	GPa	157	201	167
Takumo įtempis	$\sigma_y$	MPa	220	231	149
Didžiausias tempiamasis stipris	$\sigma_{uts}$	MPa	499	554	439
Pailgėjimas	EL	%	42	67	48
Puasono santykis	$\nu$	-	0,27	0,3	

**19 lentelė.** Austenitinio nerūdijančio plieno takumo riba, nustatyta pagal eksperimentinių tyrimų pirmąjį ciklą

Medžiaga	Mėginio tipas	Kiekis	Deformacijos amplitudė	Temperatūra	Takumo riba
		Simbolis	$\Delta\varepsilon$	$T$	$\sigma_{iys}$
		Vienetai	%	°C	MPa
AISI304L	Kietas	Vertybės	0,3	300	79
			0,6		65
0,18			20	133	
0,6			300	68	
0,5			20	105	
			300	94	
1			20	120	
			300	91	
Tuščiaviduris			0,3	300	133
Įpjauta, r = 0,5 mm			-		76
Įpjauta, r = 2 mm			-		37

Lentelėje (žr. 19 lentelę) pateiktos austenitinio nerūdijančio plieno takumo ribos esant skirtingoms apkrovimo deformacijoms ir temperatūroms. Takumo riba buvo

nustatyta pagal eksperimentinių tyrimų pirmojo ciklo įtempio-deformacijos kreivę. Taškas, kuriame įtempio-deformacijos kreivė nukrypsta nuo tiesinio tamprumo srities, buvo laikoma tiriamojo metalo takumo riba.

### 3.4. Kinematinis kietėjimas

Atliekant metalų tyrimus nustatyta, kad veikiant ciklinėms apkrovoms, takumo paviršiaus centras pasislenka plastinio takumo kryptimi, atskleidžiamas *Bauschingerio* efektą [102]. Kinematinis modelis efektyviai apibūdina aprašytą efektą, nes jame teigiama, kad progresuojant plastiškumui, plastiškumo paviršius pasislenka įtempių erdvėje, išlaikydamas pastovų dydį [98–102].

Dėl ciklinės plastinės deformacijos sudėtingumo daugelis esamų medžiagų modelių turi ribotas galimybes tiksliai atkurti eksperimentiniuose tyrimuose stebimą ciklinio plastiškumo būvį. Kadangi ciklinis metalų plastiškumas yra sudėtingas reiškinys, todėl reikia atlikti nemažai eksperimentų, kad būtų galima išsamiai ištirti tokius aspektus kaip ciklinis medžiagos kietėjimas ar minkštėjimas ir progresyvinės deformacijos (angl. *ratcheting*), atsirandančios dėl kiekvieno ciklo metu vykstančios plastinės deformacijos.

Chaboche ir kt. (1979) [109] ir Chaboche (1986) [105] pasiūlė naują kinematinio kietėjimo modelį. Modeliui aprašyti naudojama lygtis (37) :

$$d\alpha_i = \frac{2}{3}C_i d\varepsilon^p - Y_i \alpha_i dp; \quad (37)$$

čia  $C$ ,  $Y$  – atitinkamai yra kinematinio sukietėjimo modulis ir laipsnio rodiklis;  $dp$  – yra sukaupta plastinė deformacija.

$$dp = \left( \frac{2}{3} d\varepsilon^p : \frac{2}{3} d\varepsilon^p \right)^{1/2}. \quad (38)$$

Lygtis (39–42) gaunama matematiškai išsprendžiant lygtį (37) :

$$\alpha_{xp} = \left[ \frac{2}{3} \frac{C_i}{Y_i} + \left( \alpha_{ixn} - \frac{2}{3} \frac{C_i}{Y_i} \right) e^{(-Y_i \Delta \varepsilon_x^p)} \right], d\varepsilon_x^p \geq 0; \quad (39)$$

$$\alpha_{xp} = \left[ -\frac{2}{3} \frac{C_i}{Y_i} + \left( \alpha_{ixn} + \frac{2}{3} \frac{C_i}{Y_i} \right) e^{(Y_i \Delta \varepsilon_x^p)} \right], d\varepsilon_x^p < 0; \quad (40)$$

$$\alpha_{xp} = \frac{2}{3} (\sigma_x - \sigma_0), d\varepsilon_x^p \geq 0; \quad (41)$$

$$\alpha_{xn} = \frac{2}{3} (\sigma_x + \sigma_0), d\varepsilon_x^p < 0; \quad (42)$$

čia  $\alpha_{ip}$  – didžiausia atgalinio įtempio vertė, veikiant tempimo arba gniuždymo apkrovoms;

$\alpha_{in}$  – minimali atgalinio įtempio vertė, veikiant tempimo arba gniuždymo apkrovoms.

Medžiagų parametrai, naudoti modeliuojant AISI 304L nerūdijantį plieną, pateikti 19 ir 20 lentelėse (analizė atlikta naudojant kompiuterinę programą „Ansys Workbench“). Kinematiniai kietėjimo parametrai esant 0,3 % ir 0,6 % deformacijų amplitudėms 300 °C temperatūroje buvo įvertinti naudojant abiejų apkrovų

eksperimentinių tyrimų 1000-ojo ciklo (nustatyta, kad tai stabilizuotas ciklas) antros pusės rezultatus, 20 lentelėje pateikti kinematinųjų parametrų komponentai, gauti įvertinus eksperimentinių tyrimų rezultatus.

**20 lentelė.** AISI 304L nerūdijančio plieno *Chaboche* modelio parametrai (*Ansys* modeliui)

$\epsilon_r$ (%)	$C1$ (MPa)	$\gamma_1$	$C2$ (MPa)	$\gamma_2$	$C3$ (MPa)	$\gamma_3$
0,3	15482,86	2427,214	16950,62	2135,42	61446,98	268,889
0,6	15482,86	575,58	16950,62	1675,4	61446,98	679,35

Greta plačiai naudojamo *Chaboche* medžiagų modelio, mažo ciklo deformacijai modeliuoti buvo naudotas ir *Armstrongo-Fredericko* plastiškumo modelis, sukurtas įtraukiant dinaminį atsistatymo narį pagal *Pragerio* [110] nustatytą tiesinio sukietėjimo taisyklę. *Armstrong-Frederick* tipo modeliai vis plačiau naudojami dėl savo pranašumų įvertinant ir proporcingas, ir neproporcingas apkrovas [104, 111]. Paskutiniu metu *Armstrong-Frederick* koncepcija buvo išplėtota, kad būtų galima atsižvelgti į sudėtingesnius apkrovos scenarijus, padidinti modelio tikslumą ir veiksmingai įvertinti tokius reiškinius kaip progresinės deformacijos (angl. *ratcheting*) greičio mažėjimas [76, 112, 113].

*Armstrongo-Fredericko* medžiagos modelyje yra įtrauktas netiesinis kinematinio kietėjimo komponentas [114]. Dinaminio atsistatymo komponentas buvo įtrauktas į *Pragerio* linijinio kinematinio kietėjimo taisyklę [110], pripažintą kaip vieną iš paprasčiausių naudojamų medžiagų modelių. Šis komponentas turi įtaką atminties išlaikymo efektui, susijusiam su deformacijos trajektorija. Modelis parodė pervertintą progresinę (angl. *ratcheting*) deformaciją [115] ir įtraukė ribotą medžiagų konstantų rinkinį, kad būtų pagerintas progresinių deformacijų prognozių tikslumas [116].

Mažo ciklo deformacijos modeliavimas naudojant *Armstrongo-Fredericko* medžiagos modelį atliktas panaudojant kompiuterinę programą „LS-DYNA“. „LS-DYNA“ turi iš anksto apibrėžtą medžiagos modelį, kuris apjungia izotropinį ir kinematinį kietėjimą, pavadintą „MAT\_153\_DAMAGE\_3“. Šis medžiagos modelis parodo kinematinį kietėjimą, kuris apibrėžiamas naudojant *Armstrongo-Fredericko* kinematinį kietėjimo modelį:

$$\dot{\alpha}_j = \frac{2}{3} C_j \dot{\epsilon}^{pl} - \gamma_j \alpha_j \dot{\epsilon}^{pl} ; \quad (43)$$

čia  $C$  – kinematinio sukietėjimo koeficientas (MPa);

$\gamma$  – kinematinio kietėjimo rodiklis;

$\epsilon^{pl}$  – plastinė deformacija;

$\dot{\epsilon}^{pl}$  – sukaupta plastinė deformacija;

$\alpha_j$  – atgalinis įtempis.

*Armstrongo-Fredericko* kinematinio kietėjimo (KH) medžiagos modelis „MAT\_153\_DAMAGE\_3“ kompiuterinėje programoje „LS-DYNA“ aprašomas pagal 43 lygtį.

$$\alpha_{max} = \sum_{x=1}^3 \left[ \frac{2}{3} C_x \dot{\epsilon}^{pl} - \gamma_x \alpha_x \dot{\epsilon}^{pl} \right]; \quad (44)$$

čia  $\alpha_{max}$  – didžiausias ciklinis įtempis (MPa).

Kinematiniai kietėjimo parametrai buvo įvertinti naudojant eksperimentinių tyrimų rezultatus pagal 44 lygtį. KH parametrai buvo įvertinti pagal kiekvieno eksperimento stabilizuotus ciklus.

21 lentelėje pateikti AISI316L nerūdijančio plieno *Armstrongo-Fredericko* kinematinio kietėjimo modelio parametrai, kurie buvo naudoti mažaciklei degradacijai prognozuoti naudojant kompiuterinę programą „LS-DYNA“.

Atliekant mažo ciklo deformacijos skaitinio modeliavimo tyrimus taip pat buvo atliekami kinematinio kietėjimo parametrų nustatymo ir kalibravimo darbai. Tong’as ir Vermeulen’as [117] atliko eksperimentinius ir skaitmeninio modeliavimo plastiškumo tyrimus. Nikelio pagrindo superlydinio kinematinio kietėjimo parametrų klampos plastiškumas buvo įvertintas ir optimizuotas, siekiant geresnių skaitinio modeliavimo rezultatų. Tong’as ir kt. [118] savo išplėstiniame darbe remdamiesi metodika, pateikta [114], pristatė nuoseklią procedūrą kinematiniams kietėjimo parametrams nustatyti ir jiems kalibruoti naudojant netiesinį mažiausių kvadratų metodą. Zhan’as ir Tong’as [119], Moslemi ir kt. [120], Koo ir Kwon [121], Rahman’as ir kt. [122], Kacar’as [123], Mahmoudi ir kt. [124], Moslemi ir kt. [120], Kacar’as [123], Huachao [60], Shutong’as ir kt. [125] atliko kinematinio kietėjimo (KH) parametrų įvertinimo ir kalibravimo tyrimus, tačiau reikia paminėti, kad nebuvo nustatytos priklausomybės šių parametrų nuo deformacijos amplitudės ir aplinkos temperatūros.

**21 lentelė.** AISI316L nerūdijančio plieno *Armstrongo-Fredericko* kinematinio kietėjimo modelio parametrai

Deformacijos amplitudė	Temperatūra	C1	γ1	C2	γ2	C3	γ3
%	°C	MPa	-	MPa	-	MPa	-
0,18	20	150500	1680	450650	2530	10560	1360
0,6	300	5000	83,3	100000	825	1000	1530
0,5	20	1505	1680	15065	253	90500	1360
	300	4000	5	25500	550	100000	1887
1	20	150	1680	1000	253	40000	360

Nepaisant išsamių kinematinio kietėjimo parametrų įvertinimo ir kalibravimo tyrimų, tai vis dar yra sudėtingas ir daug laiko reikalaujantis procesas, nes dažniausiai

šiuos įvertintus kinematinio kietėjimo parametrus reikia kalibruoti modeliavimo metu, o tai yra papildomas ir sudėtingas bei daug laiko reikalaujantis procesas.

Siekiant sumažinti kinematinio kietėjimo parametrų įvertinimo ir kalibravimo proceso sudėtingumą, reikia sumažinti modeliavimo paklaidas ir sutrumpinti modeliavimo procesą. Kiekvienam kinematinio kietėjimo parametro komponentui išvestos priklausomybės, kuriose įvertinama deformacijos amplitudės ir darbinės temperatūros įtaką šiems komponentams. Priklausomybės suformuluotos remiantis 23 lentelėje pateiktais kinematinio kietėjimo parametrais, kurie naudojami AISI316L nerūdijančio plieno mažo ciklo deformacijai prognozuoti naudojant kompiuterinę programą „LS-DYNA“. Išvestose priklausomybėse (45–50 lygtys) yra įvertinama deformacijų ir temperatūrų įtaka:

$$C_1 = -0,0122\sigma_{YS} - 8,8551 \Delta\varepsilon^2 + 10,5727\Delta\varepsilon + 1,2496T; \quad (45)$$

$$\gamma_1 = -264,3294 \Delta\varepsilon^2 + 715,8896 \Delta\varepsilon + 48,1017T; \quad (46)$$

$$C_2 = 0,1158\sigma_{YS} + 0,0805 \Delta\varepsilon^2 - 26,2504\Delta\varepsilon + 1,4235T; \quad (47)$$

$$\gamma_2 = 9263,575 \Delta\varepsilon^2 + 695,3537\Delta\varepsilon + 21,2144T; \quad (48)$$

$$C_3 = 0,4333\sigma_{YS} + 12,3301 \Delta\varepsilon^2 + 10986,4059 \Delta\varepsilon + 3,2122T; \quad (49)$$

$$\gamma_3 = 10324634,68 \Delta\varepsilon^2 + 5012,0759\Delta\varepsilon + 37,6428T; \quad (50)$$

čia

$\sigma_{YS}$  – takumo riba (MPa);

$\Delta\varepsilon$  – deformacijos amplitudė (%);

$$T = \frac{\text{Operating Temperature } (^{\circ}\text{C})}{20 (^{\circ}\text{C})}.$$

Suformuluotos lygtys (45–50) buvo panaudotos kinematiniams kietėjimo parametrams įvertinti atliekant mažaciklį irimo / susidėvėjimo (apkrovos kontroliuojant pagal deformacijas) skaitinį prognozavimą. Nustatyti parametrai pagal šias lygtis pateikti 22 lentelėje. Šie apskaičiuoti parametrai naudoti skaitmeniniam prognozavimui naudojant kompiuterinę programą „LS-DYNA“.

**22 lentelė.** Kinematinio kietėjimo parametrai įvertinti naudojant 45–50 lygtis

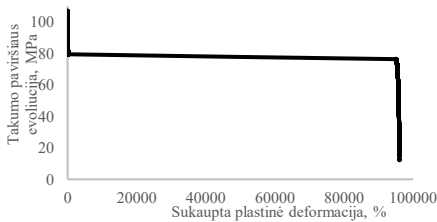
Mėginio tipas		Pilnaviduris	Tuščiaviduris
Deformacijos amplitudė	%	1	0.3
Temperatūra	°C	300	
C1	MPa	18640	19300
Y1	-	1173,09	912,5
C2	MPa	12440	30740
Y2	-	550	485,1
C3	MPa	49440	109640
Y3	-	842	1642,14

### 3.5. Izotropinis kietėjimas

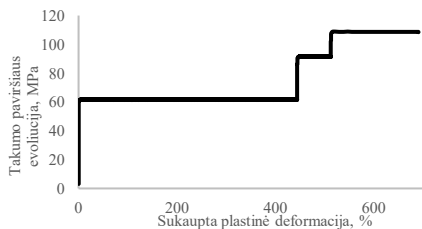
Siekiant aprašyti mažo ciklo deformacijos modeliavimą naudojamame izotropiniame modelyje yra įprasta, kad bet kurio apkrovimo etapo metu takumo paviršiaus centras nuosekliai yra pradžios taške, o paviršius plečiasi homogeniškai, progresuojant plastinei deformacijai. Dažnai naudojamas netiesinis izotropinis modelis, dar vadinamas *Voce* modeliu [111]. Šiame modelyje takumo paviršiaus kitimą apibūdina pasipriešinimo įtempio R kitimas [98–102].



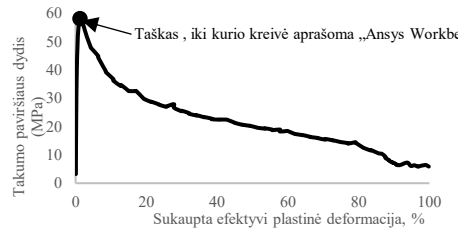
**78 pav.** AISI304L nerūdijančio plieno izotropinio kietėjimo kreivė, apskaičiuota esant 0,3 % deformacijos amplitudei 300 °C temperatūroje (naudojama *Ansys* modelyje)



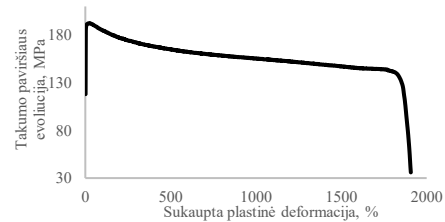
**80 pav.** AISI316L nerūdijančio plieno izotropinio kietėjimo kreivė, kurio deformacijos amplitudė yra 0,18 % 20 °C temperatūroje (naudojama *LS-DYNA* modelyje)



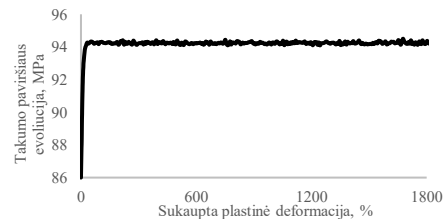
**82 pav.** Izotropinės kietėjimo kreivės, naudotos įpjauto bandinio skaitmeniniam modeliavimui, kai  $r = 0,5$  mm



**79 pav.** AISI 304L nerūdijančio plieno izotropinio kietėjimo kreivė, apskaičiuota esant 0,6 % deformacijos amplitudei 300 °C temperatūroje (naudojama *Ansys* modelyje)



**81 pav.** AISI316L nerūdijančio plieno izotropinio kietėjimo kreivė, naudojama *LS-DYNA* modelyje, AISI 316L plienas, esant 0,6 % deformacijos amplitudei 300 °C temperatūroje (naudojama *LS-DYNA* modelyje)



**83 pav.** Izotropinės kietėjimo kreivės, naudojamos įpjauto bandinio skaitmeniniam modeliavimui,  $r = 2$  mm

Paveiksluose (78,79 pav.) pavaizduotos izotropinio kietėjimo kreivės, gautos iš eksperimentinių tyrimų rezultatų, esant 0,3 % ir 0,6 % deformacijos amplitudėms 300

°C temperatūroje. Mažo ciklo deformacijos bandymo modeliavimai, esant 0,3 % ir 0,6 % deformacijos amplitudei, buvo atlikti naudojant kompiuterinę programą „Ansys Workbench“. Aprašant izotropinio kietėjimo kreivę „Ansys Workbench“ programoje, nebuvo nustatytos vertės, mažesnės už paskutinę įvestą sukauptos plastinės deformacijos vertę vertinant takumo plokštumą. Kompiuterinė programa „Ansys Workbench“ nesugebėjo generuoti takumo paviršiaus neigiamo nuolydžio, todėl buvo nuspręsta, kad maksimalus takumo paviršiaus dydis išlieka pastovus. Dėl šios priežasties buvo taikomos tik kylančios vertės. Kompiuterinėje programoje „Ansys Workbench“ izotropinio kietėjimo kreivei nustatyti buvo panaudoti tik apskaičiuotų kreivių segmentai iki raudonai paryškintų taškų [43] (78 ir 79 pav.).

Takumo paviršiaus pokytis buvo apskaičiuotas pagal 51 lygtį. O sukaupta plastinė deformacija apskaičiuojama pagal 52 lygtį, nes apkrovas kontroliuojant pagal deformacijas,  $\Delta \varepsilon_{pl}$  beveik nesikeičia:

$$\sigma = \sigma_{max,i} - \sigma_{y0}; \quad (51)$$

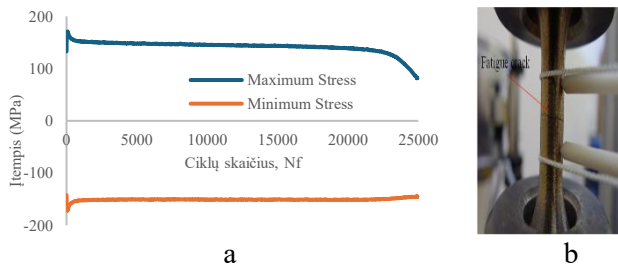
$$\dot{\varepsilon}^{pl} = 2N\Delta\varepsilon_{pl}. \quad (52)$$

Mažaciklio susidėvėjimo / irimo skaitmeniniam modeliavimui naudotos AISI316L nerūdijančio plieno medžiagos izotropinės kietėjimo kreivės buvo apskaičiuotos pagal 51 ir 52 lygtis. Modeliavimui naudotos AISI316L nerūdijančio plieno medžiagos izotropinės kietėjimo kreivės pateiktos 80–83 paveiksluose. Šių medžiagų mažaciklio irimo modeliavimas buvo atliktas naudojantis kompiuterinę programą „LS-DYNA“.

#### 4. EKSPERIMENTINIŲ TYRIMŲ REZULTATAI

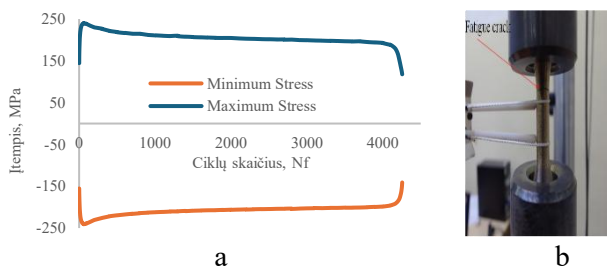
Norint suprasti komponentų medžiagų degradacijos eigą kontroliuojamomis, bazinėmis eksploatacijos sąlygomis yra svarbu atlikti mažo ciklo degradacijos (LCF) eksperimentinius bandymus. Eksperimentiniai bandymai oro sąlygomis nustato atskaitos tašką medžiagos degradacijos trukmei, nevertinant aplinkos poveikio mechaniniam irimo atsakui. Eksperimentiniai bandymai oro aplinkoje yra paprastesni ir ekonomiškесni nei aukšto slėgio / aukštos temperatūros aplinkoje, nes jiems nereikia sudėtingos infrastruktūros, vandens cheminės sudėties kontrolės ar saugos priemonių. Tarptautiniai degradacijos bandymų standartai (ASTM ir ISO) yra paruošti bandymams atlikti oro aplinkoje, todėl gautus tyrimų rezultatus galima tiesiogiai palyginti su jau nustatytais medžiagų duomenimis, kurie yra skirti medžiagoms klasifikuoti ir kurie naudojami projektuojant komponentus. Komponentų projektavimas ir atranka yra būtini renkantis pradines medžiagas. Paminėtina, kad ypač svarbu įvertinti prognozuojamų degradacijų charakteristikas prieš investuojant į brangesnius, konkrečiai aplinkai skirtus eksperimentinius bandymus.

Darbe atlikta 11 mažo ciklo degradacijos tyrimų, apkrovas kontroliuojant pagal deformacijas ir įtempius. Eksperimentinių tyrimų metu buvo tiriama įtempių priklausomybė nuo ciklų skaičiaus. Kaip tyrimų rezultatai, buvo pateiktos įtempių priklausomybės nuo ciklų skaičiaus kreivės. Eksperimentinių tyrimu metu manoma, kad bandinys suyra, kai įtempio lygis sumažėja 25 %, palyginti su maksimaliu įtempio mažėjimo lygiu.



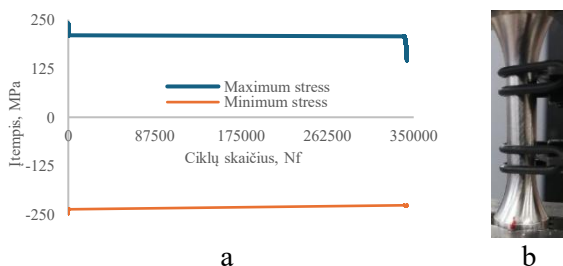
**84 pav.** AISI304L nerūdijančio plieno įtempių priklausomybė nuo ciklų skaičiaus, esant 0,3 % deformacijos amplitudei 300 °C temperatūroje

AISI 304L nerūdijančio plieno eksperimentinių tyrimų rezultatai, esant 0,3 % deformacijos amplitudei 300 °C temperatūroje, pateikti 84 paveiksle. Įtempių priklausomybė nuo ciklų skaičiaus parodyta paveiksle (84a pav.), o bandinio su degeneraciniu plyšiu nuotrauka pateikta kitame paveiksle (84b pav.). Plyšio formavimasis bandinyje nustatytas tarp ekstancionetro kojelių bandinio centre. Iš įtempių-ciklų kreivių matyti, kad per pirmuosius kelis ciklus įtempių amplitudė didėjo iki 61-ojo ciklo, o tada nustatytas didžiausio įtempio sumažėjimas, po kurio bandinys stabilizavimosi ir suiro 24923 - ajame cikle. Šie bandomieji tyrimai buvo atlikti Lietuvos energetikos institute (LEI).



**85 pav.** AISI304L nerūdijančio plieno įtempių priklausomybė nuo ciklų skaičiaus esant 0,6 % deformacijos amplitudei 300 °C temperatūroje

AISI304L nerūdijančio plieno eksperimentinių tyrimų rezultatai, esant 0,6 % deformacijos amplitudei 300 °C temperatūroje, pateikti 85 paveiksle. Medžiagos būseną, t. y. įtempių priklausomybę nuo ciklų skaičiaus (85a pav.), buvo panaši į būseną esant 0,3 % deformacijos amplitudei. Iš įtempių-ciklų kreivių skaičiaus matyti, kad per pirmuosius kelis ciklus įtempių amplitudė didėjo iki 61- ojo ciklo, o tada pastebėtas didžiausio įtempio sumažėjimas, po kurio viskas stabilizavimosi ir bandinys suiro 4256 - ajame cikle. Deformacijos plyšys pradėjo formotis už ekstanciometro kojelių viršutinėje bandinio pusėje (85b pav.). Tai gali būti susiję su lokalizuota įtempių koncentracija šalia ekstanciometro kojelės įdubos [42]. Šie eksperimentiniai tyrimai buvo atlikti LEI.

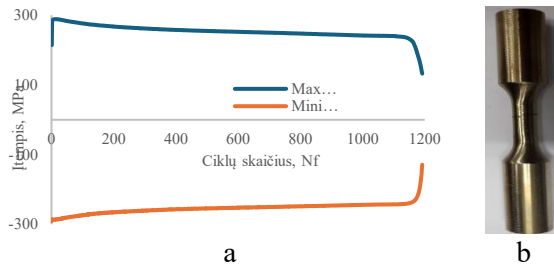


**86 pav.** AISI316L nerūdijančio plieno įtempių priklausomybė nuo ciklų skaičiaus esant 0,18 % deformacijos amplitudei 20 °C temperatūroje

AISI 316L nerūdijančio plieno eksperimentinių tyrimų rezultatai esant 0,18 % ir 0,6 % deformacijos amplitudėms 20 °C ir 300 °C temperatūrose pateikti 86 ir 87 paveiksle. Įtempių priklausomybės nuo ciklų skaičiaus parodytos 86a ir 87a paveiksluose [126], o 86b ir 87b paveiksluose pateiktos bandinio su deformacijos plyšiu nuotraukos. Plyšio formavimasis bandiniuose nustatytas tarp ekstanciometro kojelių bandinio centre.

Iš įtempių-ciklų skaičių kreivėse (86a pav.) matyti, kad per pirmuosius kelis ciklus įtempių amplitudė didėjo iki 6 - ojo ciklo esant 0,18 % deformacijos amplitudei 20 °C temperatūroje. Nuo septintojo ciklo didžiausias įtempis per ciklą mažėjo iki 1235 - ojo ciklo, po kurio viskas stabilizavosi ir įtempis svyravo nuo 210 MPa iki 214 MPa iki 326557- ojo ciklo. Po 326557- ojo ciklo didžiausias įtempis

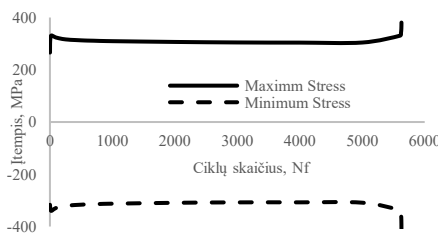
nuosekliai mažėjo per kelis ciklus ir tai sukėlė bandinio pleišėjimą, bandinys suiro esant 342 870 - ajam ciklui [126].



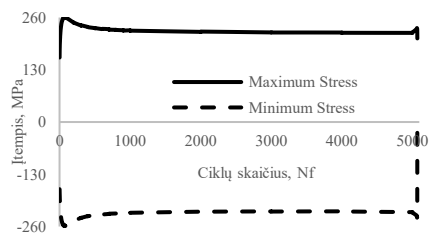
**87 pav.** AISI316L nerūdijančio plieno įtempių priklausomybė nuo ciklų skaičiaus esant 0,6 % deformacijos amplitudei 300 °C temperatūroje

AISI 316L nerūdijančio plieno eksperimentinių tyrimų rezultatai, esant 0,6 % deformacijos amplitudei 300 °C temperatūroje, buvo panašūs į rezultatus, esant 0,3 % deformacijos amplitudei. Iš įtempių-ciklų skaičių kreivės matyti, jog pirmuosius kelis ciklus įtempių amplitudė didėjo iki 10 - ojo ciklo. Nuo vienuoliktojo ciklo didžiausias įtempis mažėjo, kol suiro 1183 - iajame cikle. Šiame tyrime nebuvo nustatyta stabilizuotos srities. Tai rodo, kad AISI 316L nerūdijantis plienas pasižymi medžiagos minkštėjimo savybėmis, kai yra veikiamas ciklinio apkrovimo [126].

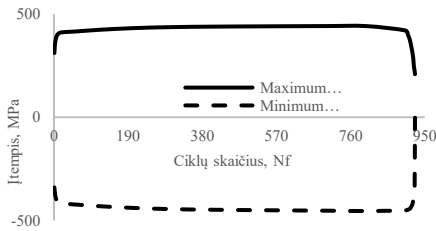
Eksperimentinių tyrimų, kurie yra atlikti Prancūzijoje, EDF laboratorijoje, rezultatai pateikti 88–92 paveiksluose. Šie eksperimentai buvo atlikti naudojant pilnavidurius ir tuščiavidurius bandinius oro ir reaktoriaus eksploatacijos aplinkoje. Naudojant pilnavidurius bandinius buvo atlikti keturi eksperimentai esant 0,5 % ir 1 % deformacijos amplitudei 20 °C ir 300 °C temperatūrose. Naudojant tuščiaviduri bandinį buvo atliktas eksperimentas esant 0,3 % deformacijos amplitudei 300 °C temperatūroje suslėgtojo vandens branduolinio reaktoriaus (PWR – suslėgtojo vandens reaktoriaus) aplinkoje.



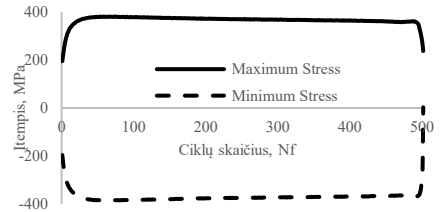
**88 pav.** AISI316L nerūdijančio plieno pilnavidurio bandinio įtempių priklausomybė nuo ciklų skaičiaus esant 0,5 % deformacijos amplitudei 20 °C temperatūroje (EDF laboratorijos eksperimentiniai rezultatai)



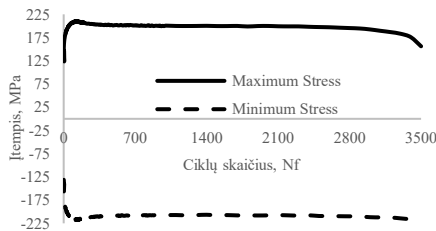
**89 pav.** AISI316L nerūdijančio plieno pilnavidurio bandinio įtempių priklausomybė nuo ciklų skaičiaus esant 0,5 % deformacijos amplitudei 300 °C temperatūroje (EDF laboratorijos eksperimentiniai rezultatai)



**90 pav. 1.** AISI316L nerūdijančio plieno pilnavidurio bandinio įtempių priklausomybė nuo ciklų skaičiaus esant 1 % deformacijos amplitudei 20 °C temperatūroje (EDF laboratorijos eksperimentiniai rezultatai)



**91 pav.** AISI316L nerūdijančio plieno pilnavidurio bandinio įtempių priklausomybė nuo ciklų skaičiaus esant 1 % deformacijos amplitudei 300 °C temperatūroje (EDF laboratorijos eksperimentiniai rezultatai)



**92 pav.** AISI316L nerūdijančio plieno tuščiavidurio bandinio įtempių priklausomybė esant 0,3 % deformacijai 300 °C temperatūroje (EDF laboratorijos eksperimentiniai rezultatai)

Iš įtempių-ciklų skaičiaus kreivės (88 pav.) matyti, kad per pirmuosius kelis ciklus įtempių amplitudė didėjo, o po to pradėjo mažėti. Bandinys suiro esant 5628 - ajam ciklui. Šio eksperimento atveju nustatyta, kad didžiausias įtempis gedimo ciklo metu didėjo, o tai galėjo atsirasti dėl to, kad įtrūkimas susidarė už ekstensometro kojelių ribų. 89 paveiksle pateikti eksperimentinių tyrimų rezultatai esant 0,5 % deformacijos amplitudei 300 °C temperatūroje. Esant tokioms tyrimo sąlygoms bandinio suirimas įvyko esant 5072 - ajam ciklui. Eksperimentinių tyrimų rezultatai esant 1 % deformacijos amplitudei 20 °C ir 300 °C temperatūrose pateikti 90 ir 91 paveiksluose. Šių eksperimentinių tyrimų metu bandiniai suiro esant 925 - ajam (90 pav.) ir 502 - ajam (91 pav.) ciklams.

Mažaciklo nuovargio (LCF) eksperimentinius tyrimus svarbu atlikti ne tik lauko sąlygomis, tačiau ir komponentų eksploatacijos sąlygomis. Tai ypač svarbu prognozuojant komponentų eksploatacijos ilgaamžiškumą. Šiame darbe yra pateikti eksperimentinių tyrimų rezultatai suslėgtojo vandens reaktoriaus (PWR) aplinkoje, siekiant įvertinti faktines branduolinio reaktoriaus komponentų, ypač pirminio kontūro vamzdynų, eksploataavimo sąlygas ir jų poveikį komponentų ilgaamžiškumui. Suslėgtojo vandens reaktoriaus (PWR) eksploatacijos temperatūra pirmojo kontūro vamzdynuose svyruoja nuo 280 °C iki 325 °C ir pasiekiamas 16,6 MPa slėgis. Šių aplinkos sąlygų veikiamą medžiagų degradacija vyksta dėl korozijos, pleišėjimo ir

priklauso nuo aplinkos sąlygų (angl. *EAC* – *environmentally assisted cracking*) ir aplinkos sukeltos degradacijos (angl. *EAF* – *environmental assisted fatigue*). Tyrimai ir eksploataavimo patirtis rodo, kad komponentų degradacijos laikas PWR aplinkoje gali būti gerokai trumpesnis nei oro sąlygomis dėl oksidacijos įtrūkio viršuje, deguonies ir vandenilio poveikio bei greitesnių plyšio didėjimo veiksmų. Tai paskatino sukurti aplinkos poveikio irimo korekcijos koeficientus. Mažo ciklo degradacijos tyrimas padeda užtikrinti atitiktį branduolinės energetikos reguliavimo institucijų pateiktuose dokumentuose, įskaitant aplinkos poveikį degradacijai. Jie taip pat padeda įvertinti medžiagų atsparumo ir susidėvėjimo tyrimus vertinant lydinių, tokių kaip 316 SS, *Inconel* ir mažai legiruoto plieno degradacijos būvį esant kombinuotai mechaninei ir aplinkos apkrovai.

Eksperimentiniai tyrimai buvo atlikti ir branduolinio reaktoriaus (suslėgto vandens reaktoriaus (PWR) tipo) aplinkoje. Eksperimentiniams tyrimams reaktoriaus aplinkoje atlikti reikalinga speciali įranga, kurios Lietuvoje nėra, todėl eksperimentiniai tyrimai buvo atlikti Prancūzijoje, EDF laboratorijoje. Darbe buvo naudoti EDF laboratorijos degradacijos modeliavimo tyrimo rezultatai, patvirtinantys reaktoriaus aplinkos sąlygas. 92 paveiksle pateikti tuščiavidurio bandinio eksperimentiniai rezultatai esant 0,3 % deformacijos amplitudei 300 °C temperatūroje suslėgto vandens reaktoriaus (PWR) aplinkoje. Esant tokioms tyrimo sąlygoms bandinio suirimas įvyko esant 3500 - ajam ciklui.

Visuose atliktuose eksperimentiniuose tyrimuose, kai apkrova kontroliuojama pagal deformacijas, buvo nustatyta panaši medžiagos būseną. Pirmųjų kelių ciklų metu maksimalūs įtempiai didėjo su kiekvienu iš eilės einančiu ciklu, po to įtempis maksimaliai mažėjo, vėliau stabilizavosi, o po to bandinys pradėjo pleišėti ir irti. Šis reiškinys vadinamas minkštėjimu / minkštėjimo procesu. Minkštėjimas susijęs su dinaminiu rekristalizavimu kambario temperatūroje ir kristalų pasisukimais aukštesnėje temperatūroje [127].

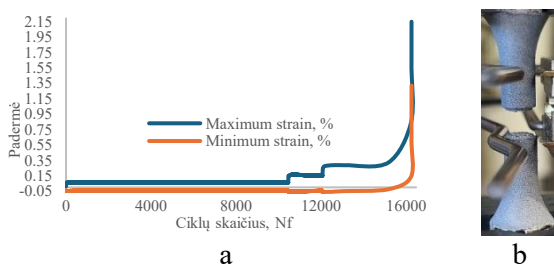
**23 lentelė.** AISI316L nerūdijančio plieno neįpjautų bandinių ciklų skaičius, kuriems esant bandinys suiro

Bandymų serijos Nr.	Deformacijos amplitudė	Temperatūra	Suirimo ciklų skaičius
	%		°C
1	0,18	20	343106
2	0,3	300	3500
3	0,5	20	5628
4		300	5072
5	0,6	300	1192
6	1	20	925
7		300	502

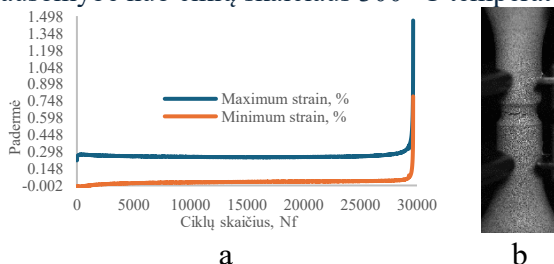
Remiantis eksperimentiniais rezultatais nustatyta, kad bandiniui suirti didelę įtaką darė deformacijos amplitudė. AISI316L nerūdijančio plieno neįpjautų

bandinių ciklų skaičius, kuriems esant bandinys suiro, pateiktas 23 lentelėje. Nustatyta, kad darbinė temperatūra taip pat turi didelę įtaką bandinio suirimui.

AISI 316L nerūdijantis plienas taip pat buvo išbandytas ir bandinio su įpjovomis. Mažo ciklo degradacijos (LCF) eksperimentiniai bandymai atliekami su įpjovos bandiniais siekiant ištirti komponentų degradacijos eigą su įtempių koncentratoriais. Įpjovos bandiniuose lemia plyšių formavimąsi įtempių atsiradimo vietose ir leidžia tirti trumpalaikį plyšių formavimosi procesą, o tai svarbu atliekant mažo ciklo degradacijos tyrimus. Buvo du eksperimentiniai bandinių tyrimai su skirtingais įpjovų spinduliais, atitinkamai 0,5 ir 2 mm esant 300 °C temperatūrai. Eksperimentiniai tyrimai bandinių su įpjovomis buvo stebimi / vertinami pagal įtempius, skirtingai nei bandiniai be įpjovų, kurie buvo stebimi / vertinami pagal deformacijas.



**93 pav.** AISI316L nerūdijančio plieno bandinio su  $r = 0,5$  mm įpjova įtempių priklausomybė nuo ciklų skaičiaus 300 °C temperatūroje



**94 pav.** AISI316L nerūdijančio plieno bandinio su  $r = 2,0$  mm įpjova įtempių priklausomybė nuo ciklų skaičiaus 300 °C temperatūroje

**24 lentelė.** AISI316L nerūdijančio plieno bandinių su įpjovomis ciklų skaičius, kuriems esant bandinys suiro

Nr.	Įpjovos spindulys	Temperatūra	Pakrovimo tipas	Ciklo numeris
	mm			°C
1	0,5	300	Laiptinis	16251
2	2		Pastovi amplitudė	29660

Mažo ciklo degradacijos eksperimentiniai tyrimai AISI316L nerūdijančio plieno bandinių su įpjovomis buvo atlikti apkrovas kontroliuojant pagal įtempius, siekiant, kad apkrovos būtų atitinkančios apkrovas, kurios buvo naudotos eksperimentams kontroliuojant jas deformavimo metu. Jėgos dydis eksperimentiniams tyrimams buvo parinktas pagal tikslinę deformaciją bandinio įpjovos gale. Bandiniui, su 0,5 mm spindulio įpjova mažo ciklo degradacijai išsiaiškinti, buvo pridedama jėgos trijų apkrovimo etapų metu, kad tikslinė deformacija įpjovos gale būtų atitinkamai 0,2 %, 0,4 % ir 0,6 %. Bandinys su 2 mm spindulio įpjova buvo išbandytas esant vienodai amplitudės jėgai, kad tikslinė deformacija įpjovos gale būtų 0,6 %.

93 ir 94 paveiksluose pateikti bandinių su įpjovomis oro sąlygomis tyrimo rezultatai 300 °C temperatūroje. Bandinio su 0,5 mm spindulio įpjova suirimas įvyko esant 16251 - ajam ciklui (žr. 24 lentelę). Bandinio su 2,0 mm spindulio įpjova suirimas įvyko esant 29660 - ajam ciklui (žr. 24 lentelę). Paveiksluose (93b ir 94b pav.) parodyti suirę bandiniai po eksperimentinio tyrimo. Bandinių suirimas įvyko įpjovose.

## 5. SKAITMENINIO MODELIAVIMO TYRIMO REZULTATAI IR PATVIRTINIMAS

Austenitinio nerūdijančio plieno skaitmeninis mažo ciklo degradacijos tyrimas naudojant baigtinių elementų metodiką, atliktas siekiant prognozuoti nagrinėtų metalų ilgaamžiškumą veikiant mažo ciklo degradacijos apkrovoms. Šiame skyriuje paaiškinami skaitinio modeliavimo tyrimų rezultatai ir pateikti naudotų modelių ir metodikų patvirtinimai, padaryti remiantis eksperimentinių tyrimų rezultatais.

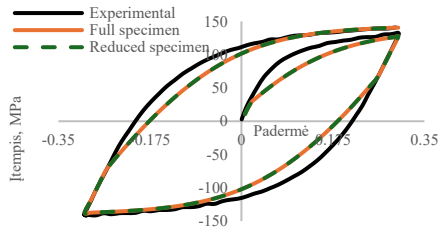
Austenitinio nerūdijančio plieno skaitmeninis mažo ciklo degradacijos modeliavimas buvo atliktas panaudojant eksperimentiniams tyrimams naudoto bandinio geometriją (71 pav.), t. y. sumažinti geometrijos bandiniai, kurie buvo apkrauti 0,3 % deformacijos amplitude, kad būtų patikrinta bandinio dydžio reikšmė modeliavimo rezultatams. Bandinio dydžio įtakos modeliavimo rezultatams nenustatytos (95 pav.). Abiejų bandinių rezultatai buvo identiški, todėl galima teigti, kad bandinio geometrijos dydis neturi įtakos skaitmeninio modeliavimo rezultatams. Svarbu, kad bandinio modeliui būtų taikomos tinkamos ribinės sąlygos ir apkrovos, o modeliuojant bandinio geometriją, galima naudoti ir trumpą bandinį, tik svarbu, kad jo skerspjūvis būtų analogiškas bandiniui. Reikia paminėti, kad viso bandinio skaičiavimas užtruko daugiau nei 1 valandą, o sumažinto bandinio – vos kelias sekundes (žr. 25 lentelę). Siekiant sutrumpinti modelio skaičiavimo laiką, visi baigtiniai elementai buvo paruošti sumažintam bandiniui (1/4 bandinio gabaritinio ilgio dalis, modelio skersmuo lygus bandinio skersmeniui).

### 25 lentelė. Pirmojo ciklo skaičiavimams reikalingas laikas

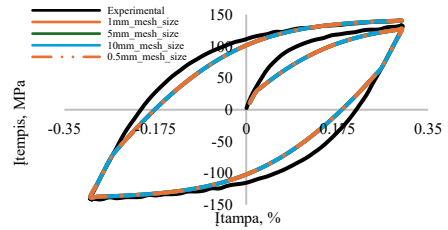
Modelio tipas	Skaičiavimams reikalingas laikas
Pilnos geometrijos bandinys	1 val. 20 m
Sumažintas bandinys	15 sek.

Priėmus sprendimą dėl modeliuojamo bandinio dydžio, baigtinių elementų modelis buvo patikrintas dėl skaitmeninio modeliavimo jautrumo modelio tinklėlio dydžiui. Paruošiant baigtinių elementų modelį skaitiniams tyrimams, yra svarbu tinkamai parinkti tinklėlio dydį. Tinklėlio jautrumas yra labai svarbus atliekant skaitmeninį mažo ciklo degradacijos modeliavimą, siekiant užtikrinti rezultatų tikslumą ir patikimumą, ypač įtempių, deformacijos koncentracijų zonose ir vertinant bandinio degradacijos ilgaamžiškumą.

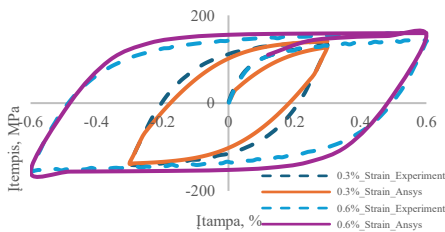
Tinklėlio jautrumo analizei buvo paruošti 4 baigtinių elementų modeliai, kurių elementų dydis buvo 0,5 mm, 1 mm, 5 mm ir 10 mm. Visi šie modeliai buvo paruošti AISI 304L austenitinio nerūdijančio plieno eksperimentiniams tyrimams esant 0,3 % deformacijos amplitudei ir 30 °C temperatūrai. Tinklėlio dydžio įtaka modeliavimo rezultatams nenustatyta (96 pav.) dėl modelio paprastumo. Siekiant skaitmeninio modeliavimo rezultatų patikimumo ir skaičiavimo efektyvumo laiko atžvilgiu, baigtinių elementų modeliams, skirtiems mažo ciklo degradacijai modeliuoti, kai apkrovos kontroliuojamos pagal deformacijas, parinktas 1 mm tinklėlio dydis.



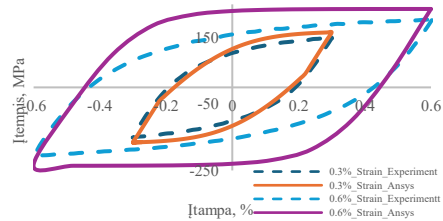
**95 pav.** Pilno ir sumažinto bandinių modeliavimo rezultatų palyginimas



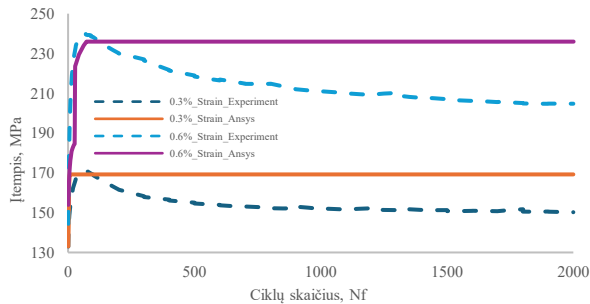
**96 pav.** Tinklelio jautrumo patikrinimas



**97 pav.** Pirmasis AISI304L nerūdijančio plieno ciklas 300 °C temperatūroje



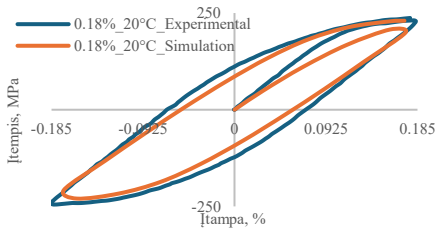
**98 pav.** 2000 - asis ciklas nerūdijančiam plienui AISI304L 300 °C temperatūroje



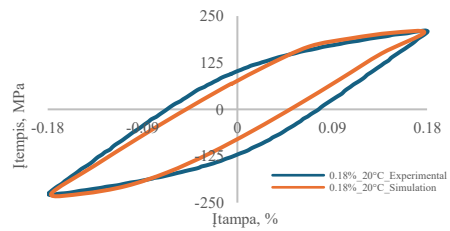
**99 pav.** AISI304L nerūdijančiam plienui įtempimų priklausomybė nuo ciklų skaičiaus esant 0,3 % ir 0,6 % deformacijos amplitudėms 300 °C temperatūroje

99 paveiksle pateikta AISI304L austenitinio nerūdijančio plieno įtempimų priklausomybė nuo ciklų skaičiaus esant 0,3 % ir 0,6 % deformacijos amplitudėms 300 °C temperatūrose. Šiame paveiksle pateikti eksperimentinių ir skaitinio modeliavimo tyrimų rezultatai, gauti esant abiem deformacijos amplitudėms. Skaitinio modeliavimo rezultatų, esant 0,3 % deformacijos amplitudėi, priimtinas sutapimas gautas tik pirmaisiais ciklais, tačiau po septintojo ciklo maksimalūs įtempiai liko nepakitę – didėjant ciklų skaičiui, įtempimų vertės 18,95 % nukrypo nuo eksperimentinių tyrimų rezultatų. Analogiškai skaitinio modeliavimo rezultatai gauti ir esant 0,6 % deformacijos amplitudėi. Skaitinio modeliavimo rezultatų, esant 0,6 % deformacijos amplitudėi, priimtinas sutapimas gautas tik pirmaisiais ciklais, tačiau po 75 - ojo ciklo maksimalūs įtempiai liko nepakitę didėjant ciklų skaičiui, įtempimų vertės

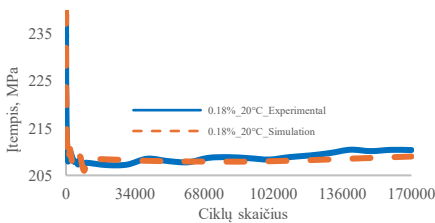
19,90 % nukrypo nuo eksperimentinių tyrimų rezultatų. Pastovios maksimalios įtempio vertės buvo gautos dėl izotropinės kreivės, naudojamos kompiuterio programoje „ANSYS“. Kompiuterio programoje „ANSYS“ negalima įvertinti medžiagų įtempių mažėjimo. Todėl nerekomenduojama naudoti kompiuterinę programą „ANSYS“ medžiagų mažo ciklo degradacijai prognozuoti. Tolimesniuose mažo ciklo degradacijos skaitinio modeliavimo tyrimuose buvo naudota kompiuterinė programa „LS-DYNA“.



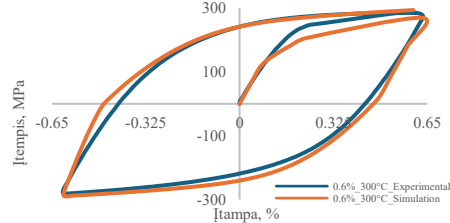
**100 pav.** AISI316L nerūdijančio plieno pirmasis ciklas, kai deformacijos amplitudė yra 0,18 % 20 °C temperatūroje



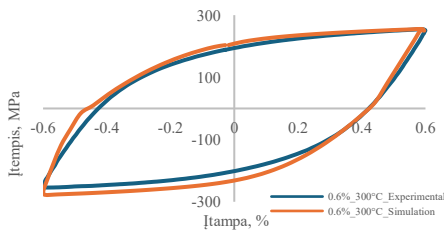
**101 pav.** AISI316L nerūdijančio plieno 2000 - asis ciklas, kai deformacijos amplitudė yra 0,18 % ir 20 °C temperatūroje



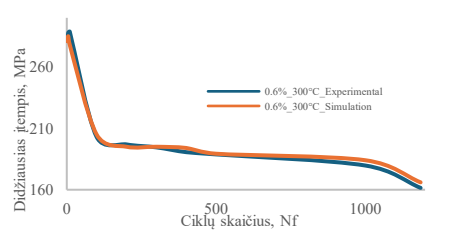
**102 pav.** AISI316L nerūdijančio plieno įtempių priklausomybė nuo ciklų skaičiaus, esant 0,18 % deformacijos amplitudei 20 °C temperatūroje



**103 pav.** AISI316L nerūdijančio plieno pirmasis ciklas, kai deformacijos amplitudė yra 0,6 % 300 °C temperatūroje



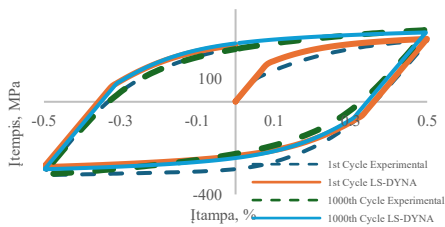
**104 pav.** AISI316L nerūdijančio plieno 500 - asis ciklas, esant 0,6 % deformacijos amplitudei 300 °C temperatūroje



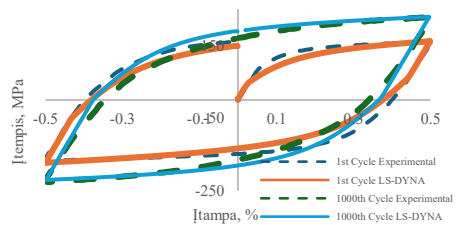
**105 pav.** AISI316L nerūdijančio plieno įtempių priklausomybė nuo ciklų skaičiaus, esant 0,6 % deformacijos amplitudei 300 °C temperatūroje

316L nerūdijančio plieno modeliavimas esant 0,18 % deformacijos amplitudei 20 °C temperatūroje ir 0,6 % deformacijos amplitudei 300 °C temperatūroje buvo atliktas naudojant „LS-DYNA FE“ programinę įrangą. Norint modeliuoti komponentų, veikiamų mažo ciklo apkrovoms ilgaamžiškumą reikiamu tikslumu, rekomenduojama įvertinti medžiagų būvį naudojant medžiagos charakteristikas, esant jau stabilizuotiems ciklams, kurie stebimi maždaug po 50 % ciklų nuo bendro ciklų skaičiaus, kai bandinys suyra [87, 121, 126]. Skaitinio mažo ciklo degeneracijos modeliavimo modeliai patvirtinami lyginant modeliavimo rezultatus su eksperimentiniais rezultatais, t. y. lyginant įtempių priklausomybes nuo ciklų skaičiaus, taip pat histerezės kilpas esant atitinkamiems ciklams.

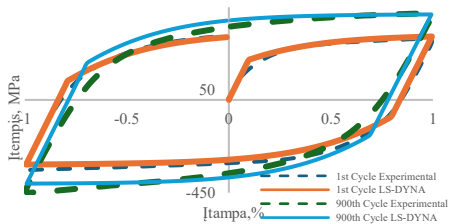
Lyginant įtempio ir deformacijos histerezės kilpas pastebimas nežymus nukrypimas skaitinio modeliavimo rezultatų nuo eksperimentinių tyrimų rezultatų. Įtempių amplitudės priklausomybės nuo ciklų skaičiaus modeliavimo rezultatai buvo labai artimi eksperimentiniams rezultatams.



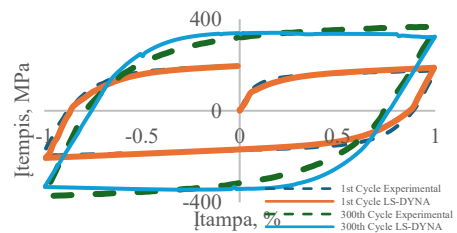
**106 pav.** Pilnavidurio bandinio pirmasis ir 1000 - asis ciklai esant 0,5 % deformacijos amplitudei 20 °C temperatūroje



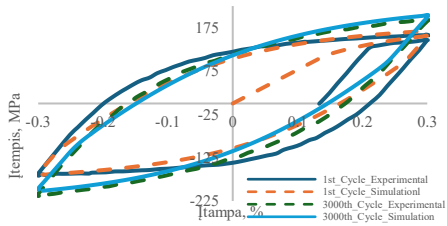
**107 pav.** Pilnavidurio bandinio pirmasis ir 1000 - asis ciklai esant 0,5 % deformacijos amplitudei 300 °C temperatūroje



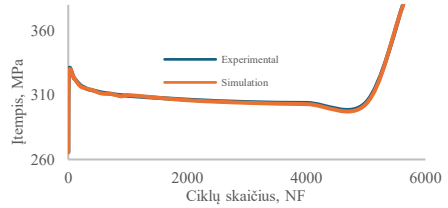
**108 pav.** Pilnavidurio bandinio pirmasis ir 900 - asis ciklai esant 1 % deformacijos amplitudei 20 °C temperatūroje



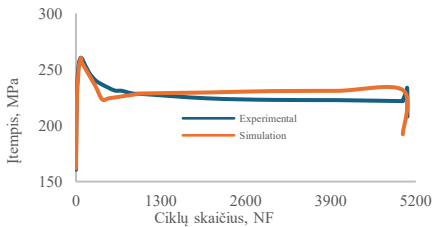
**109 pav.** Pilnavidurio bandinio pirmasis ir 300 - asis ciklai esant 1 % deformacijos amplitudei 300 °C temperatūroje



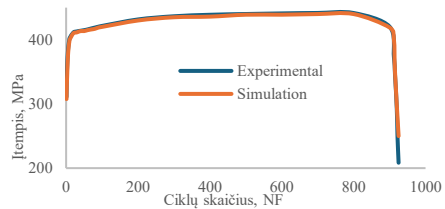
**110 pav.** Tuščiavidurio bandinio pirmasis ir 3000 - asis ciklai esant 0,3 % deformacijos amplitudei 300 °C temperatūroje



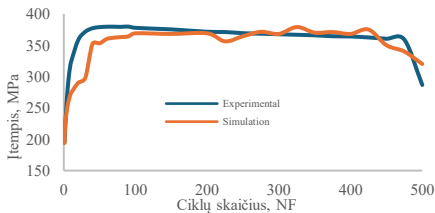
**111 pav.** Pilnavidurio bandinio įtempių priklausomybė nuo ciklų skaičiaus esant 0,5 %, deformacijos amplitudei 20 °C temperatūroje



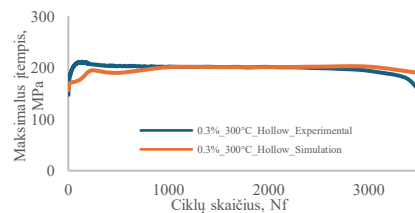
**112 pav.** Pilnavidurio bandinio įtempių priklausomybė nuo ciklų skaičiaus esant 0,5 % deformacijos amplitudei 300 °C temperatūroje



**113 pav.** Pilnavidurio bandinio įtempių priklausomybė nuo ciklų skaičiaus esant 1 % deformacijos amplitudei 20 °C temperatūroje



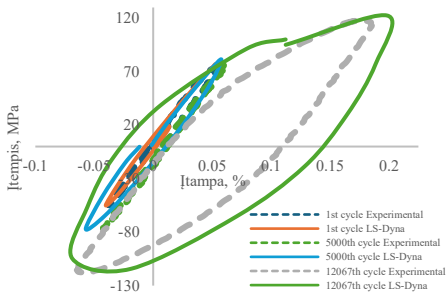
**114 pav.** Pilnavidurio bandinio įtempių priklausomybė nuo ciklų skaičiaus esant 1 % deformacijos amplitudei 300 °C temperatūroje



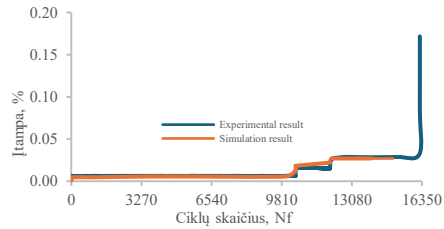
**115 pav.** Tuščiavidurio bandinio įtempių priklausomybė nuo ciklų skaičiaus esant 0,3 % deformacijos amplitudei 300 °C temperatūroje

Esant pradiniam ciklams prognozuojamos maksimalios įtempio vertės nukrypsta nuo eksperimentinių rezultatų, tačiau didėjant ciklų skaičiui, modeliavimo rezultatų nukrypimas nuo eksperimentinių rezultatų mažėja. Didžiausių įtempių per pirmuosius 100 ciklų modeliavimo nukrypimas nuo eksperimentinių siekia 1,58 %; tarp 101- ojo ir 170 000 - ojo ciklų įtempių vertės, esant 0,18 % deformacijos amplitudės modeliui, nukrypo 0,5 % [126], o esant 0,6 % deformacijos amplitudės modeliui, modeliavimo rezultatų nukrypimas nuo eksperimentų yra atitinkamai 3,7 % ir 1 % esant ciklams tarp 1–60 - ojo ciklo ir nuo 61 - ojo ciklo iki 1192 - ojo ciklo.

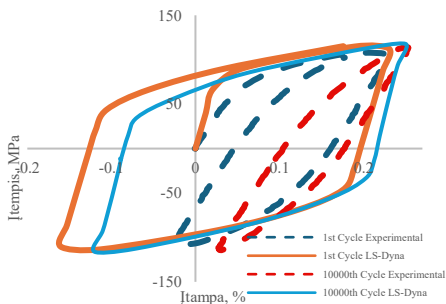
Pilnavidurio bandinio modeliavimo rezultatai, gauti esant 0,5 % ir 1 % deformacijos amplitudei 20 °C ir 300 °C temperatūrose, pateikti 106–109 ir 111–114 paveiksluose. 106–109 paveiksluose pateiktos pirmojo ciklo įtempio ir deformacijos histerezės kilpos esant 0,5 % deformacijos amplitudei 20 °C ir 300 °C temperatūrose bei 1 % deformacijos amplitudei 20 °C temperatūroje. Mažo ciklo degeneracijos modeliavimui, esant 0,5 % ir 1 % deformacijos amplitudėms, buvo atlikti naudojant kinematinio grūdinimo parametrus, taikant *Armstrongo-Fredricko* medžiagos kinematinio kietėjimo modelį.



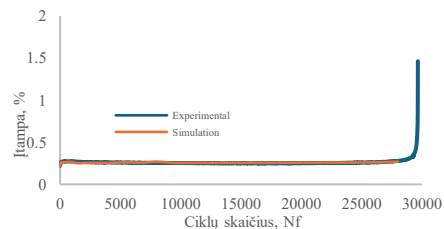
**116 pav.** Pirmasis, 900 - asis ir 12000 - asis ciklai, kai bandinio įpjova  $r = 0,5$  mm 300 °C temperatūroje



**117 pav.** Įtempių priklausomybė nuo ciklų skaičiaus, kai bandinio įpjova  $r = 0,5$  mm 300 °C temperatūroje



**118 pav.** Pirmasis ir 1000 - asis ciklai, kai bandinio įpjova  $r = 2$  mm 300 °C temperatūroje



**119 pav** Įtempių priklausomybė nuo ciklų skaičiaus, kai bandinio įpjova  $r = 2$  mm 300 °C temperatūroje

Pateiktos pirmajam ir 1000 - ajam ciklams įtempių ir deformacijos histerezės esant deformacijos amplitudei 20 °C ir 300 °C temperatūrose, pirmajam ir 900 - ajam ciklams esant 1 % deformacijos amplitudei abiejose temperatūrose. Palyginus modeliavimo rezultatus su eksperimentinių tyrimų rezultatais nustatyta, kad modeliavimo rezultatų nukrypimas nuo eksperimentinių yra mažas. Pateikti mažo ciklo degeneracijos rezultatai yra priimtini, paruoštą medžiagos modelį galima naudoti komponentų degradacijos ilgąamžiškumui prognozuoti.

Todėl atlikus kinematinio kietėjimo parametrų priklausomybės nuo deformacijų amplitudės ir temperatūros analizės, buvo suformuluoti visų kinematinio kietėjimo parametrų ryšiai, įvertinantys deformacijų amplitudės ir temperatūros įtaką.

Naudojant išvestas (45–50) lygtis, kinematinio kietėjimo parametrai buvo apskaičiuoti ir panaudoti pilnavidurio bandinio, esant 1 % deformacijos amplitudei abiejose temperatūrose ir tuščiavidurio bandinio, esant 0,3 % deformacijos amplitudei 300 °C temperatūroje, modeliavimams. Naudojant apskaičiuotus kinematinio kietėjimo parametrus gauti mažo ciklo degradacijos prognozavimo rezultatai pateikti 109–110 ir 114–115 paveiksluose.

Pilnavidurio bandinio modeliavimo rezultatai pirmojo ir 300 - ojo ciklą įtempių ir deformacijų histerezės, esant 1 % deformacijos amplitudei 300 °C temperatūroje, pateikti 109 paveiksle. Tuščiavidurio bandinio modeliavimo rezultatai pirmojo ir 3000 - ojo ciklą, esant 0,3 % deformacijos amplitudei 300 °C temperatūroje, pateikti 110 paveiksle. Kinematiniai kietėjimo parametrai buvo naudojami pagal 45–50 lygtis be papildomo apskaičiuotų parametru kalibravimo.

Mažo ciklo degradacijos skaitinio modeliavimo ir eksperimentinių tyrimų įtempių priklausomybės nuo ciklą skaičiaus pateiktos 111–115 paveiksluose. Palyginus modeliavimo rezultatus su eksperimentiniais rezultatais, modeliavimo rezultatų nukrypimas nuo eksperimentinių tyrimų rezultatų yra nedidelis. Modeliavimo rezultatų nukrypimas nuo eksperimentų ne didesnis kaip 0,6 % ir 8,1 % esant 0,5 % deformacijos amplitudei 20 °C ir 300 °C temperatūrose, ir 16 % esant 1 % deformacijos amplitudei 20 °C temperatūroje. Didesnis nuokrypis nustatytas esant 0,3 % ir 1 % deformacijos amplitudei 300 °C temperatūroje. Kaip minėta anksčiau, šiems modeliavimams naudojami kinematiniai kietėjimo parametrai buvo apskaičiuoti naudojant suformuluotas lygtis (45–50) ir nebuvo kalibruoti. 0,3 % (tuščiaviduris bandinys) ir 1 % (pilnaviduris bandinys) deformacijos amplitudės 300 °C temperatūroje atveju gautas modeliavimo rezultatų nuokrypis nuo eksperimentų ne didesnis kaip 10 % esant ciklams, per kuriuos įvyko bandinio suirimas. Didžiausias nuokrypis gautas pradinių ciklą metu ir nebuvo didesnis kaip 13 % ir 19 %. Mažo ciklo degradacijos modeliavimo rezultatų nuokrypiai nuo eksperimentinių tyrimų rezultatų pateikti 26 lentelėje.

Bandymo su įpjovomis mažo ciklo degradacijos skaitinio modeliavimo ir eksperimentinių tyrimų, apkrovą kontroliuojant pagal įtempius, rezultatai pateikti 116–119 paveiksluose. Skaitinis modeliavimas dėl skaičiavimo laiko buvo atliekamas maždaug iki 15 000 ciklą, esant 0,5 mm spindulio įpjovai ir 28 000 ciklą, esant 2 mm spindulio įpjovai.

Bandinių su 0,5 mm ir 2 mm spindulio įpjovomis prognozuojamos ir eksperimentinės įtempių priklausomybės nuo ciklą skaičiaus pateiktos 117 ir 119 paveiksluose. Abiejų maksimalių įtempių modelių: prognozuojamų ir eksperimentinių, gautas priimtinas sutapimas. Atitinkamai, minėtų bandinių modeliavimo ir eksperimentinių tyrimų įtempių ir deformacijų histerezės pateiktos 116 ir 118 paveiksluose. 116 paveiksle pateiktos bandinio su 0,5 mm spindulio įpjovomis pirmojo, 9000 - ojo ir 12000 - ojo ciklą histerezės. Esant dviem pirmiesiems apkrovos etapams, modeliavimo rezultatai buvo artimi eksperimentiniams rezultatams, tačiau, apkrovos ciklui pasiekus trečiąjį apkrovos etapą, kreivė šiek tiek nukrypo nuo eksperimentinės kreivės. Modeliavimo metu buvo užfiksuotas medžiagos deformacijos pobūdis, koks buvo matomas ir eksperimento metu.

**26 lentelė.** Mažo ciklo degradacijos modeliavimo rezultatų nuokrypis nuo eksperimentinių tyrimų rezultatų

<b>Bandymo Nr.</b>	1	2	3	4	5	6	7	8	9	10	11	
<b>Mėginio tipas</b>	Pilnaviduris								Tuščiaviduris	Išjautas		
<b>Medžiaga</b>	AISI304L			AISI316L								
<b>Temperatūra, (°C)</b>	300		20	300	20	300	20	300	300	300		
<b>Deformacijų amplitudė, (%)</b>	0,3	0,6	0,18	0,6	0,5			1	0,3		-	-
<b>Įvertinti kinematiniai kietėjimo parametrai</b>	Naudojant KH modelio lygtis (45–50).							Naudojant KH modelio lygtis (45–50)		Naudojant KH modelio lygtis (45–50)		
<b>Kompiuterinė programa</b>	ANSYS WB			LS-DYNA								
<b>Didžiausia paklaida (%)</b>	18,95	19,9	1,58	3,7	0,6	8,1	1,6	13	16	6,9	9,3	

118 paveiksle pateiktos bandinio su 2 mm spindulio įpjovomis pirmojo ir 10000 - ojo ciklų histerezės. Palyginus modeliavimo rezultatus su eksperimentiniais rezultatais nustatyta, kad modelio įtempio ir deformacijos histerizės buvo simetriškos, skirtingai nei eksperimentinės histerizės, nes modelis negalėjo užfiksuoti medžiagos minkštėjimo būsenos dėl kontroliuojamos apkrovos pagal jėgą, kaip buvo pastebėta eksperimentiniuose tyrimuose. Tačiau įtempių priklausomybės nuo ciklų skaičiaus ir modeliavimo rezultatų sutapimas su eksperimentiniais buvo gautas tinkamai (119 pav.).

### 5.1. Skyriaus išvada

Mažo ciklo degradacijos tyrimai, panaudojant skaitmeninio modeliavimo metodus ir lyginant juos su eksperimentiniais tyrimais, yra ekonomiškai, lengviau pritaikomi esant įvairioms sąlygoms ir kompleksiniams variantams. Nors skaitmeniniai metodai negali visiškai pakeisti eksperimentinių bandymų, tačiau galima teigti, kad gali gerokai pagerinti gebėjimą prognozuoti degradacijos būseną, patobulinti projektus ir sumažinti išsamių fizinių bandymų poreikį, ypač sudėtingose ar pavojingose aplinkose. Skaitmeniniai tyrimai buvo atlikti panaudojant baigtinių elementų kompiuterių programas „Ansys Workbench“ ir „LS-DYNA“. Medžiagos tamprumas ir plastiškumas buvo aprašytas panaudojant medžiagų modelius, kuriuose įvertinamas kinematinis ir izotropinis kietėjimas degradacijos metu. Nustatyta, kad

mažo ciklo degradacijai modeliuoti baigtinių elementų tinklelis neturi didelės įtakos. Skaitmeniniam modeliavimui paruošti modeliai patvirtinti eksperimentinių tyrimų rezultatais.

AISI 304L nerūdijančio plieno bandinio mažo ciklo degradacijai, esant deformacijos amplitudėms 0,3 ir 0,6 %, modeliuoti buvo panaudota kompiuterinė programa „Ansys Workbench“. Tyrimų rezultatai parodė prognozuojamų rezultatų reikšmingą nukrypimą nuo eksperimentinių rezultatų. Reikiami rezultatai buvo gauti tik esant pradiniam ciklam, kurių metu įtempių amplitudės didėjo. Kompiuterių programa „Ansys Workbench“ negalima įvertinti medžiagos įtempių mažėjimo, todėl negalima modeliuoti medžiagos minkštėjimo, kaip buvo matoma eksperimentiniuose tyrimuose.

AISI 316L nerūdijančio plieno mažo ciklo degradacijos skaitiniams modeliavimo tyrimams buvo naudota kompiuterinė programa „LS-DYNA“. Įvertinti medžiagos kinematinio kietėjimo parametrus buvo naudotas *Armstrong-Frederick* medžiagos kinematinio kietėjimo metodas, o šiems parametrms kalibruoti naudotas stabilizuotas ciklas. Mažo ciklo degradacijos skaitinio modeliavimo tyrimai atlikti apkrovas kontroliuojant pagal deformacijas ir esant 0,18 %, 0,5 %, 0,6 %, 1 % deformacijos amplitudėms, o bandinių su 0,5 mm, 2 mm spindulio įpjovomis modeliavimai atlikti apkrovas kontroliuojant pagal įtempius.

AISI 316L nerūdijančio plieno kinematinio kietėjimo parametrms nustatyti buvo išvestos lygtys, įvertinančios deformacijų ir temperatūros įtakas. Šios lygtys patvirtintos modeliuojant pilnavidurį bandinį, esant 1 % deformacijos amplitudei ir tuščiavidurį bandinį, esant 0,3 % deformacijos amplitudei. Mažo ciklo susidėvėjimo modeliavimas, naudojant kompiuterinę programą „LS-DYNA“, leido užfiksuoti ciklinį medžiagos kietėjimą ir minkštėjimą, o skaitinio modeliavimo rezultatai buvo labai artimi eksperimentiniams rezultatams.

Mažo ciklo degradacijos AISI 316L nerūdijančio plieno pilnavidurio bandinio, esant 1 % deformacijos amplitudei ir tuščiavidurio bandinio, esant 0,3 % deformacijos amplitudei, modeliavimo tyrimuose buvo naudoti kinematiniai kietėjimo parametrai, kurie buvo apskaičiuoti naudojant išvestas lygtis. Skaitinio modeliavimo tyrimų rezultatų nukrypimas nuo eksperimentinių tyrimų nebuvo didesnis kaip 16 %. Nustatyta, kad AISI 316L nerūdijančio plieno mažo ciklo kinematinis kietėjimo parametras galima naudoti be papildomo kalibravimo.

Atlikus AISI 316L nerūdijančio plieno bandinių su 0,5 mm ir 2 mm spindulio įpjovomis mažo ciklo degradacijos skaitinio modeliavimo ir eksperimentinius tyrimus, nustatytas priimtinas įtempių priklausomybių nuo ciklų skaičiaus sutapimas. Taip pat palyginus modeliavimo rezultatus su eksperimentiniais rezultatais nustatyta, kad bandinio su 2 mm spindulio įpjovomis įtempio ir deformacijos histerizės buvo simetriškos, skirtingai nei eksperimentinės histerizės, nes modelis negalėjo užfiksuoti medžiagos minkštėjimo būsenos dėl kontroliuojamos apkrovos pagal jėgą, kaip buvo matoma eksperimentiniuose tyrimuose.

## IŠVADOS

1. Šiame darbe atliktas eksperimentinis AISI 304L ir AISI 316L austenitinių nerūdijančiojo plieno mažo ciklo degradacijos tyrimas esant 20 °C ir 300 °C temperatūroms, deformacijai ir įtempių kontroliuojamai apkrovai. Buvo išbandyti vientisi, tuščiaviduriai ir įpjauti bandiniai. Eksperimentinė programa buvo parengta pagal ASTM E606/E606M ir ASTM E1012 reikalavimus. Eksperimentinio tyrimo metu buvo stebimas kinematinis grūdinimas per pirmuosius kelis ciklus, po kurių sekė ciklinis medžiagos minkštėjimas ir galiausiai bandinio lūžis. Bandinių mažo ciklo degradacijos trukmei didelę įtaką turėjo deformacijos amplitudė. Darbinė temperatūra taip pat turėjo tam tikros įtakos bandinio gedimo ciklui. AISI 316L nerūdijančiojo plieno atveju, padidėjus deformacijos amplitudei 277,78 % ir esant tokiai pačiai temperatūrai, gedimo ciklas sumažėjo 98,36 %, o padidinus temperatūrą nuo 20 °C iki 300 °C, gedimo ciklas sumažėjo 9,88 %. Eksperimentinių tyrimų metu, veikiant įtempio kontroliuojamai apkrovai, buvo nustatytas bandinių su 0,5 mm ir 2 mm spindulio įpjovomis medžiagos minkštėjimas (suspaudimas), dėl kurio įtempio ir deformacijos histerezė buvo asimetriška, nors apkrovos buvo simetriškos.
2. Baigtinių elementų metodas buvo naudojamas mažo ciklo degradacijai modeliuoti su pilnaviduriais, tuščiaviduriais ir 0,5 mm bei 2 mm spindulio įpjovomis bandiniais. Medžiagos kinematiniam grūdinimui apibūdinti buvo naudojama *Armstrongo-Fredericko* kinematinė grūdinimo taisyklė. Kinematiniai grūdinimo parametrai buvo įvertinti naudojant stabilizuotą ciklą. Medžiagos izotropinis grūdinimas buvo nustatytas naudojant netiesinį izotropinį grūdinimo modelį, vadinamą *Voce* modeliu. Izotropiniai ir kinematiniai grūdinimo parametrai buvo kalibruoti pagal eksperimentinius rezultatus. Deformacijos, veikiančios apkrovos modelio atveju, neturėjo reikšmės bandinio modeliavimo rezultatams, tačiau elemento dydis buvo įvertintas, todėl buvo naudojamas mažesnis bandinys. Bandiniui su įpjova buvo sumodeliuotas viso ilgio bandinys, o įpjovos zonai modeliuoti buvo naudojamas smulkus tinklelis, kad būtų užfiksuota įtempio koncentracija. Mažo ciklo degradacijai modeliuoti naudojami modeliai buvo patvirtinti eksperimentinių tyrimų rezultatais.
3. Kinematinis grūdinimas mažo ciklo degradacijos skaitmeninio modeliavimo metu buvo aprašytas naudojant *Armstrong-Frederick* kinematinio grūdinimo modelį. Darbinė temperatūra ir deformacijos amplitudė turėjo tam tikrą įtaką kinematinio grūdinimo parametrui. Iš jų deformacijos amplitudė buvo dominuojantis veiksnys, turintis įtakos K, H parametrui. Didėjant deformacijos amplitudei K, H parametrai mažėja. Kinematinio grūdinimo parametrų įvertinimas yra sudėtingas procesas, kuriam reikia papildomo žingsnio kalibruoti parametrus pagal eksperimentinius rezultatus, o tai yra sudėtingas ir daug laiko reikalaujantis procesas. Siekiant sumažinti kinematinio grūdinimo parametrų įvertinimo sudėtingumą ir laiką bei panaikinti kalibravimo procesą, išvedami ryšiai tarp kinematinio grūdinimo parametrų, deformacijos amplitudės ir darbinės temperatūros. Šie ryšiai buvo naudojami įvertinimui, todėl buvo išvestos lygtys, skirtos nustatyti AISI 316L nerūdijančiojo plieno kinematinio grūdinimo

parametrus, kurie parodo deformacijos ir temperatūros įtaką. Šios lygtys buvo patvirtintos naudojant eksperimentinių tyrimų rezultatus. Naudojant šias lygtis buvo apskaičiuoti kinematiniai grūdinimo parametrai, kurie buvo tiesiogiai naudojami mažo ciklo degradacijai modeliuoti be kalibravimo proceso, kuris sutrumpino vertinimo laiką išlaikydamas parametų tikslumą. Mažo ciklo degradacijos modeliavimas naudojant „LS-DYNA“ kompiuterinę programą leido užfiksuoti ciklinį medžiagos grūdinimą ir minkštėjimą, o skaitinio modeliavimo rezultatai buvo labai artimi eksperimentiniams rezultatams. Mažo ciklo degradacijos modeliavimo, naudojant apskaičiuotus kinematinis grūdinimo parametrus be kalibravimo, rezultatus patvirtino eksperimentinių tyrimų rezultatai.

4. Darbe atlikti AISI 304L ir AISI 316L austenitinių nerūdijančiojo plieno mažo ciklo degradacijos skaitinio modeliavimo tyrimai 20 °C ir 300 °C temperatūrose oro sąlygomis ir 300 °C temperatūroje reaktoriaus aplinkoje, kontroliuojant deformacijas ir kontroliuojant jėgą ant kietų, tuščiavidurių ir įpjautų bandinių. Kompiuterinė programa „ANSYS“ negali priimti mažėjančių įtempių verčių norint apibrėžti izotropinę grūdinimo kreivę, todėl buvo neįmanoma modeliuoti medžiagos minkštėjimo būsenos, kuri buvo atliekant eksperimentinius tyrimus. Dėl šios priežasties „Ansys Workbench“ programa davė gerų rezultatų pradiniam grūdinimo etape ir vėlesnėje nuolatinės įtempių amplitudės fazėje per visą modeliavimo laikotarpį, o nuokrypis nuo eksperimentinių rezultatų siekė 19,9 %. Todėl mažo ciklo degradacijai modeliuoti buvo naudojama kompiuterinė programa „LS-DYNA“. AISI 316L plienų mažo ciklo nuovargio skaitmeniniai modeliavimai buvo atlikti esant 0,18 %, 0,5 %, 0,6 % ir 1 % deformacijos amplitudėms kietiems bandiniams ir 0,3 % deformacijos amplitudei tuščiaviduriams bandiniams. Įtempio kontroliuojamo mažo ciklo degradacijos / irimo bandymai atlikti su 0,5 mm ir 2 mm spindulio įpjovomis. Medžiagos kinematiniais grūdinimo parametrams įvertinti buvo naudojamas *Armstrongo-Fredericko* medžiagų kinematinio grūdinimo metodas. Skaitmeninio modeliavimo tyrimų rezultatų nuokrypis nuo eksperimentinių tyrimų buvo ne didesnis kaip 16 %. Padidėjus deformacijos amplitudei nuo 0,5 % iki 1 % (t. y. 200 % padidėjus deformacijos amplitudei), rezultatų paklaida padidėja 60,49 %. Galima daryti išvadą, kad parengti modeliai gali būti naudojami mažo ciklo degradacijos ilgaamžiškumui prognozuoti esant deformacijos kontroliuojamai pastovios amplitudės apkrovai.

## PASIŪLYMAI

Pateikta mažo ciklo degradacijos skaitmeninio modeliavimo metodologija gali būti taikoma, kai apkrovos kontroliuojamos pagal deformacijas kontroliuojamai pastoviai amplitudei ir esant simetrinei apkrovai. Atliekant tolimesnius mažo ciklo degradacijos / irimo tyrimus reikia sukurti medžiagos kietėjimo modelį, kuris galėtų įvertinti medžiagos būseną nesimetrinių ir daugiaašių apkrovų atvejais.

Mažo ciklo degradacijos, kontroliuojant apkrovas pagal įtempius / jėgą, bandymo metu pastebimas medžiagos minkštėjimas (angl. *ratcheting*), todėl atsiranda

tempimo-gniuždymo asimetriškumas. Tolimesniuose tyrimuose reikia modifikuoti medžiagos kietėjimo modelį, kad būtų galima įvertinti medžiagos plastinės deformacijos tendencijas vienašio ir daugiaašio apkrovimo atvejais, kai apkrovos kontroliuojamos pagal įtempius.

## LIST OF REFERENCES

1. ADASOORIYA, N.D.; HEMMINGSEN, T. and PAVLOU, D. Fatigue strength degradation of metals in corrosive environments. *IOP Conference Series: Materials Science and Engineering*, 276, 2017, 012039.  
Available from: <https://doi.org/10.1088/1757-899x/276/1/012039>
2. LAKSHMI, S. and PRABHA, C. A review on low-cycle fatigue failure. *International Journal of Science Technology and Engineering*, 3, 2017, 11.  
Available from: <https://www.ijste.org/articles/IJSTEV3I11066.pdf>
3. BJORHEIM, F.; SIRIWARDANE, S.C. and PAVLOU, D. A review of fatigue damage detection and measurement techniques. *International Journal of Fatigue*, 154, 2022, 106556. ISSN: 0142-1123.  
Available from: <https://doi.org/10.1016/j.ijfatigue.2021.106556>
4. DUNDULIS, G.; JANULIONIS, R.; GRYBĖNAS, A.; MAKAREVIČIUS, V.; DUNDULIS, R. Numerical and experimental investigation of low-cycle fatigue behaviour in P91 steel. *Engineering Failure Analysis*, 79, 2017, p. 285–295.  
Available from: <https://doi.org/10.1016/j.engfailanal.2017.05.001>
5. BRUCHHAUSEN, M.; DUNDULIS, G.; MCLENNAN, A.; ARRIETA, S.; AUSTIN, T.; CICERO, R. et al. Characterization of austenitic stainless steels with regard to environmentally assisted fatigue in simulated light water reactor conditions. *Metals*, 11, 2021, 2, 307. ISSN 2075-4701.  
Available from: <https://doi.org/10.3390/met11020307>
6. BRUCHHAUSEN, M.; MCLENNAN, A.; CICERO, R.; HUOTILAINEN, C.; MOTTERSHEAD, K.; LE ROUX, J. and VANKEERBERGHEN, M. INCEFA-PLUS project: Review of the test programme. In: *Proceedings of the ASME 2020 Pressure Vessels and Piping Conference*. New York: ASME, 2020. ISBN: 978-0-7918-8381-5.  
Available from: <https://doi.org/10.1115/PVP2020-21377>
7. SPATIG, P.; LE ROUX, J.-C.; BRUCHHAUSEN, M. and MOTTERSHEAD, K. Mean stress effect on fatigue life of 304L steel in air and PWR environments. *Metals*, 11, 2021, 2, 221. ISSN: 2075-4701.  
Available from: <https://doi.org/10.3390/met11020221>
8. BEHRAVESH, S.B.; IBRAHIM, E. and JAHED, H. Fatigue failure analysis of welded structures. In: *Handbook of Materials Failure Analysis*. Oxford: Elsevier, 2016, p. 355–386. ISBN: 9780081001165.  
Available from: <https://doi.org/10.1016/b978-0-08-100116-5.00014-4>
9. ARRIETA, S.; CICERO, S.; MCLENNAN, A.; CICERO, R.; BESWICK, J.; COURTIN, S. and QUE, Z. Review of INCEFA-SCALE project advances. *Procedia Structural Integrity*, 72, 2025, p. 362–369. ISSN 2452-3216.  
Available from: <https://doi.org/10.1016/j.prostr.2025.08.115>
10. ARRIETA, S.; AUSTIN, T.; BRUCHHAUSEN, M.; CHITTY, W. J.; CICERO, R.; CICERO, S.; CUVILLIEZ, S.; DE BAGLION, L.; DUNDULIS, G.; et. al. INCEFA-PLUS findings on environmental fatigue. Zenodo, 2020.  
Available from: <https://doi.org/10.5281/zenodo.4243979>
11. Pate, S. B., Dundulis, G., Kilikevičius, S. and Grybenas, A. Experimental and numerical examination of low cycle fatigue behaviour on AISI304L steel. *Nuclear Engineering and Design*, Vol. 429 (2024), 113599. ISSN 0029-5493.  
Available from: <https://doi.org/10.1016/j.nucengdes.2024.113599>

12. PATE, S.B.; DUNDULIS, G.; GRIŠKEVIČIUS, P. Modelling of low-cycle fatigue behaviour of AISI 316L steel using Armstrong–Frederick hardening. *Materials*, 17, 2024, 14, 3395.  
Available from: <https://doi.org/10.3390/ma17143395>
13. KIM, Y.; HWANG, W. Fatigue and fracture behaviour of low-carbon steel and welded joints. *Materials*, 12, 2019, 24, 4111.  
Available from: <https://doi.org/10.3390/ma12244111>
14. FARHAT, H. Typical service-induced damages. In: *Operation, Maintenance, and Repair of Land-Based Gas Turbines*. Oxford: Elsevier, 2021, p. 107–130. ISBN 9780128218341.  
Available from: <https://doi.org/10.1016/B978-0-12-821834-1.00006-X>
15. ANTAKI, G. and GILADA, R. Design basis loads and qualification. In: *Nuclear Power Plant Safety and Mechanical Integrity*. Oxford: Elsevier, 2015, p. 27–102. ISBN 978-0-12-417248-7.  
Available from: <https://doi.org/10.1016/b978-0-12-417248-7.00002-3>
16. HATANAKA, K.; YAMADA, T. and HIROSE, Y. Effective plastic strain component for low-cycle fatigue. *Bulletin of the JSME*, 23, 1980, 180, p. 791–798.  
Available from: <https://doi.org/10.1299/jsme1958.23.791>
17. DAVIS, J.R. (ed.). *Stainless Steels*. Materials Park: ASM International, 1994.
18. ANNAN, C. and BEAUMONT, E. Low-cycle fatigue of stainless steel plates. *Journal of Building Engineering*, 29, 2019, 101160. ISSN 2352-7102.  
Available from: <https://doi.org/10.1016/j.jobe.2019.101160>
19. GORDON, B.M. Corrosion and corrosion control in light water reactors. *JOM*, 65, 2013, 8, p. 1043–1056.  
Available from: <https://doi.org/10.1007/s11837-013-0658-4>
20. ABARKAN, I.; SHAMASS, R.; ACHEGAF, Z. and KHAMLICHI, A. Numerical and analytical studies of low-cycle fatigue of 316LN steel. *Journal of Pressure Vessel Technology*, 144, 2022, 6, 061507.  
Available from: <https://doi.org/10.1115/1.4045897>
21. PEDERSEN, M. M. *Introduction to Metal Fatigue: Concepts and Engineering Approaches*. Technical Report ME-TR-11. Aarhus: Department of Engineering, Aarhus University, 2018. ISSN 2245-4594.  
Available from: <https://tidsskrift.dk/me/article/view/110952/160076>
22. COFFIN Jr., L. F. A study of the effects of cyclic thermal stresses on a ductile metal. *Transactions of the American Society of Mechanical Engineers*, 76, 1954, 6, p. 931–950.  
Available from: <https://doi.org/10.1115/1.4015020>
23. SCHIJVE, J. *Fatigue of Structures and Materials*. 2nd ed. Dordrecht: Springer, 2009.  
Available from: <https://doi.org/10.1007/978-1-4020-6808-9>
24. QIU, Z.; ZHANG, Z. and WANG, L. Numerical analysis methods of structural fatigue and fracture problems. In: DARJI, P.H. and DARJI, V.P. (eds.). *InTechOpen eBooks*. London: InTechOpen, 2018. ISBN 978-1-78923-159-5.  
Available from: <https://doi.org/10.5772/intechopen.72285>
25. MANSON, S. S. Behavior of materials under conditions of thermal stress. 1954.
26. MANSON, S. S. Fatigue: A complex subject—some simple approximations. *Experimental Mechanics*, 5, 1965, p. 193–226.
27. BASQUIN, O. H. The exponential law of endurance tests. *Proceedings of the American Society for Testing Materials*, 10, 1910, p. 625–630.
28. WANG, X.; ZHANG, W.; ZHANG, T.; GONG, J. and WAHAB, M. A. A new empirical life prediction model for 9–12%Cr steels under low-cycle fatigue and creep–fatigue interaction loadings. *Metals*, 9, 2019, 2.

- Available from: <https://doi.org/10.3390/met9020183>
29. MORROW, J. Fatigue design handbook. *Advances in Engineering*, 4, 1968, 3, p. 21–29.
  30. SMITH, K. N.; WATSON, P. and TOPPER, T. H. A stress–strain function for the fatigue of materials. *Journal of Materials*, 5, 1970, p. 767–778.
  31. BROWN, M. W. and MILLER, K. J. A theory for fatigue failure under multiaxial stress–strain conditions. *Proceedings of the Institution of Mechanical Engineers*, 187, 1973, 1, p. 745–755.  
Available from: [https://doi.org/10.1243/PIME\\_PROC\\_1973\\_187\\_161\\_02](https://doi.org/10.1243/PIME_PROC_1973_187_161_02)
  32. KANDIL, F. A.; BROWN, M. W. and MILLER, K. J. Biaxial low-cycle fatigue failure of 316 stainless steel at elevated temperatures. London: Metals Society, 1982. ISBN 0-904357-41-4.
  33. SHATIL, G. and SMITH, D. J. Life prediction and high-strain multiaxial fatigue of an engineering component. In: PINEAU, A.; CAILLETAUD, G.; LINDLEY, T.C. (eds.). *Multiaxial Fatigue and Design*. ESIS 21. London: Mechanical Engineering Publications, 1996, p. 499–511.
  34. DASSAULT SYSTEMES SIMULIA CORP. *Fatigue Theory Reference Manual*. Vol. 2. Providence: Safe Technology Ltd., 2014.
  35. VAITKUNAS, T.; GRISKEVICIUS, P.; DUNDULIS, G.; *et al.* Peridynamic numerical investigation of asymmetric strain-controlled fatigue behaviour using the kinetic theory of fracture. *Advanced Modeling and Simulation in Engineering Sciences*, 11, 2024, 12.  
Available from: <https://doi.org/10.1186/s40323-024-00264-4>
  36. ABEDI, R. and HABER, R. B. Spacetime simulation of dynamic fracture with crack closure and frictional sliding. *Advanced Modeling and Simulation in Engineering Sciences*, 2018.  
Available from: <https://doi.org/10.1186/s40323-018-0116-5>
  37. SILLING, S. Reformulation of elasticity theory for discontinuities and long-range forces. *Journal of the Mechanics and Physics of Solids*, 48, 2000, p. 175–209.  
Available from: [https://doi.org/10.1016/S0022-5096\(99\)00029-0](https://doi.org/10.1016/S0022-5096(99)00029-0)
  38. SILLING, S.; EPTON, M.; WECKNER, O.; XU, J. and ASKARI, E. Peridynamic states and constitutive modeling. *Journal of Elasticity*, 88, 2007, p. 151–184.  
Available from: <https://doi.org/10.1007/s10659-007-9125-1>
  39. BOBARU, F. and HU, W. The meaning, selection, and use of the peridynamic horizon and its relation to crack branching. *International Journal of Fracture*, 176, 2012, p. 215–222.  
Available from: <https://doi.org/10.1007/s10704-012-9725-z>
  40. MADENCI, E. and OTERKUS, S. Ordinary state-based peridynamics for plastic deformation according to von Mises yield criteria. *Journal of the Mechanics and Physics of Solids*, 86, 2016, p. 192–219.  
Available from: <https://doi.org/10.1016/j.jmps.2015.09.016>
  41. SILLING, S. A. and ASKARI, A. Peridynamic model for fatigue cracking. 2014.  
Available from: <https://doi.org/10.2172/1160289>
  42. PASHAZAD, H. and KHARAZI, M. Peridynamic plastic model with isotropic and kinematic hardening under cyclic loading. *International Journal of Mechanical Sciences*, 156, 2019, p. 182–204.  
Available from: <https://doi.org/10.1016/j.jimecsci.2019.03.033>
  43. FRISWELL, M. I. and MOTTERSHEAD, J. E. Finite element modelling. In: *Solid Mechanics and Its Applications*. Dordrecht: Springer, 1995, p. 7–35.  
Available now: [https://doi.org/10.1007/978-94-015-8508-8\\_2](https://doi.org/10.1007/978-94-015-8508-8_2)

44. ROY, S. C.; GOYAL, S.; SANDHYA, R. and RAY, S. Low-cycle fatigue life prediction of 316L(N) stainless steel. *Nuclear Engineering and Design*, 253, 2012, p. 219–225.  
Available from: <https://doi.org/10.1016/j.nucengdes.2012.08.024>
45. MENG, L.; SUN, J.; XING, H.; YU, W. and XUE, F. Study of low-cycle fatigue of AL6XN austenitic stainless steel. *Nuclear Engineering and Design*, 241, 2012, 8, p. 2839–2842.  
Available from: <https://doi.org/10.1016/j.nucengdes.2011.06.011>
46. FACHERIS, G. and JANSSENS, K.G.F. Cyclic mechanical behavior of 316L: Uniaxial LCF and strain-controlled ratcheting tests. *Nuclear Engineering and Design*, 257, 2013, p. 100-108. ISSN 0029-5493.  
Available from: <https://doi.org/10.1016/j.nucengdes.2013.01.010>
47. CHEN, G.; ZHANG, Z.; FENG, S.; JIANG, K.; YU, J.; WU, H.; SHI, S. and LIN, Q. Improvement of low-cycle fatigue behavior of modified 9Cr-1Mo steels at 450 °C in liquid LBE environment by the addition of Si element. *Nuclear Engineering and Design*, 413, 2023, 112570.  
Available from: <https://doi.org/10.1016/j.nucengdes.2023.112570>
48. CAO, Y.; MOUMNI, Z.; ZHU, J.; ZHANG, Y.; YOU, Y. and ZHANG, W. Comparative investigation of the fatigue limit of additive-manufactured and rolled 316 steel based on self-heating approach. *Engineering Fracture Mechanics*, 223, 2019ss, 106746.  
Available from: <https://doi.org/10.1016/j.engfracmech.2019.106746>
49. BRANCO, R.; COSTA, J.; BERTO, F.; RAZAVI, S.; FERREIRA, J.; CAPELA, C.; SANTOS, L. and ANTUNES, F. Low-Cycle fatigue behaviour of AISI 18Ni300 maraging steel produced by selective laser melting. *Metals*, 8, 2018, 1.  
Available from: <https://doi.org/10.3390/met8010032>
50. WANG, X.; ZHANG, W.; ZHANG, T.; GONG, J. and WAHAB, M. A. A New Empirical Life Prediction Model for 9–12%Cr Steels under Low Cycle Fatigue and Creep Fatigue Interaction Loadings. *Metals*, 9, 2019, 2.  
Available from: <https://doi.org/10.3390/met9020183>
51. KANG, G. and LIU, Y. Uniaxial ratcheting and low-cycle fatigue failure of the steel with cyclic stabilizing or softening feature. *Materials Science and Engineering A*, 472, 2008, p. 258–268.  
Available from: <https://doi.org/10.1016/j.msea.2007.03.045>
52. YANG, X. Low cycle fatigue and cyclic stress ratcheting failure behavior of carbon steel 45 under uniaxial cyclic loading. *International Journal of Fatigue*, 27, 2005, p. 1124–1132.  
Available from: <https://doi.org/10.1016/j.ijfatigue.2005.02.003>
53. ZHANG, X.; WANG, T.; GONG, Q.; LI, Y.; et al. Low cycle fatigue properties, damage mechanism, life prediction and microstructure of MarBN steel: Influence of temperature. *International Journal of Fatigue*, 144, 2021, 106070.  
Available from: <https://doi.org/10.1016/j.ijfatigue.2020.106070>
54. WANG, Q.; WANG, Q.; GONG, X.; WANG, T.; et al. A comparative study of low cycle fatigue behavior and microstructure of Cr-based steel at room and high temperatures. *Materials and Design*, 195, 2020, 109000.  
Available from: <https://doi.org/10.1016/j.matdes.2020.109000>
55. YOU, J. H. and MISKIEWICZ, M. Material parameters of copper and CuCrZr alloy for cyclic plasticity at elevated temperatures. *Journal of Nuclear Materials*, 373, 2008, 1–3, p. 269-274. ISSN 0022-3115.  
Available from: <https://doi.org/10.1016/j.jnucmat.2007.06.005>

56. ROESSLE, M. L. and FATEMI, A. Strain-controlled fatigue properties of steels and some simple approximations. *International Journal of Fatigue*, 22, 2000, p. 495–511.  
Available from: [https://doi.org/10.1016/S0142-1123\(00\)00037-2](https://doi.org/10.1016/S0142-1123(00)00037-2)
57. ABARKAN, I.; SHAMASS, R.; ACHEGAF, Z. and KHAMLI CHI, A. Numerical and Analytical Studies of Low Cycle Fatigue Behavior of 316 LN Austenitic Stainless Steel. *Journal of Pressure Vessel Technology*, 144, 2022, 6, 061507.  
Available from: <https://doi.org/10.1115/1.4045897>
58. DIERCKS, D. R. Development of Fatigue Design Curves for Pressure Vessel Alloys using a Modified Langer Equation. *Journal of Pressure Vessel Technology*, 101, 1979, 4, p. 292- 297.  
Available from: <https://doi.org/10.1115/1.3454104>
59. JASKE, C. E. and O'DONNELL, W. J. L. Fatigue design criteria for pressure vessel alloys. *Journal of Pressure Vessel Technology*, 99, 1977, 4, p. 584-592.  
Available from: <https://doi.org/10.1115/1.3454448>
60. CHOPRA, O. K. Development of a fatigue design curve for austenitic stainless steels in LWR environments: A review. In: *Proceedings of the ASME 2002 Pressure Vessels and Piping Conference. American Society of Mechanical Engineers*, 2002, p. 119–132.  
Available from: <https://doi.org/10.1115/PVP2002-1219>
61. TSUTSUMI, S.; BUERLIHAN, A. and FINCATO, R. Numerical study on fatigue notch sensitivity of high and middle strength carbon steels for welded structures. *Journal of the Japan Society of Civil Engineers, Series A2 (Applied Mechanics)*, 77, 2021, 2, p. I\_145–I\_153.  
Available from: [https://doi.org/10.2208/jscejam.77.2\\_I\\_145](https://doi.org/10.2208/jscejam.77.2_I_145)
62. TSUTSUMI, S. and FINCATO, R. Cyclic plasticity model for fatigue with softening behaviour below macroscopic yielding. *Materials and Design*, 165, 2019, 107573. ISSN 0264-1275.  
Available from: <https://doi.org/10.1016/j.matdes.2018.107573>
63. FINCATO, R.; YONEZAWA, T. and TSUTSUMI, S. Numerical modeling of cyclic softening/hardening behavior of carbon steels from low- to high-cycle fatigue regime. *Archives of civil and mechanical engineering*, 23, 2023, 164.  
Available from: <https://doi.org/10.1007/s43452-023-00698-4>
64. YANG, H. ; ZHANG, W. ; ZHUANG, X. and ZHAO, Z. Calibration of chaboche combined hardening model for large strain range. *Procedia Manufacturing*, 47, 2020, p. 867–872.  
Available from: <https://doi.org/10.1016/j.promfg.2020.04.272>
65. ZHANG, Z. ; TU, H. ; HU, Z. ; LI, Y. ; ZHANG, B. and WANG, Z. Experimental and numerical investigation of low-cycle fatigue behavior of 9Cr ferritic-martensitic steel at room temperature. *Material Design and Processing Communications*, 2, 2020, 2.  
Available from: <https://doi.org/10.1002/mdp2.130>
66. HAN, J.; MARIMUTHU, K. P.; KOO, S. and LEE, H. Numerical implementation of modified Chaboche kinematic hardening model for multiaxial ratcheting. *Computers and Structures*, 231, 2020, 106222.  
Available from: <https://doi.org/10.1016/j.compstruc.2020.106222>
67. HAI, L. ; WANG, Y. ; BAN, H. ; LI, G. and DU, X. A simplified prediction method on Chaboche isotropic/kinematic hardening model parameters of structural steels. *Journal of Building Engineering*, 68, 2023, 106151.  
Available from: <https://doi.org/10.1016/j.jobe.2023.106151>

68. MOHANTY, S.; SOPPET, W. K.; MAJUMDAR, S. and NATESAN, K. Chaboche-based cyclic material hardening models for 316 SS–316 SS weld under in-air and pressurized water reactor water conditions. *Nuclear Engineering and Design*, 305, 2016, p. 524–530.  
Available from: <https://doi.org/10.1016/j.nucengdes.2016.05.031>
69. SANTUS, C., GROSSI, T., ROMANELLI, L., PEDRANZ, M., and BENEDETTI, M. A computationally fast and accurate procedure for the identification of the Chaboche isotropic-kinematic hardening model parameters based on strain-controlled cycles and asymptotic ratcheting rate. *International Journal of Plasticity*, 160, 2022, 103503.  
Available from: <https://doi.org/10.1016/j.ijplas.2022.103503>
70. SHIVA, V.; CHRISTOPHER, J.; VEERABABU, J.; PARTHASARATHI, N.; KANNAN, R.; NAGESHA, A. and VASUDEVAN, M. Effect of maximum applied cyclic stress on fretting fatigue stress distribution of flat-on-flat modified 9Cr-1Mo steel contact: Finite element analysis. *Nuclear Engineering and Design*, 417, 2023, 112883.  
Available from: <https://doi.org/10.1016/j.nucengdes.2023.112883>
71. HORMOZI, R. ; BIGLARI, F. and NIKBIN, K. Experimental and numerical creep–fatigue study of Type 316 stainless steel failure under high temperature LCF loading condition with different hold time. *Engineering Fracture Mechanics*, 141, 2015.  
Available from: <https://doi.org/10.1016/j.engfracmech.2015.05.007>
72. SLAVIK, O.; VOJTEK, T.; POCZKLAN, L.; TINOCO, H. A.; KRUML, T.; HUTAR, P. and SMID, M. Improved description of low-cycle fatigue behaviour of 316L steel under axial, torsional and combined loading using plastic J-integral. *Theoretical and Applied Fracture Mechanics*, 118, 2021b, 103212.  
Available from: <https://doi.org/10.1016/j.tafmec.2021.103212>
73. ZHU, P.; GAO, J.; YUAN, Y.; WU, Z. and XU, R. An improved multiaxial Low-Cycle Fatigue Life Prediction model based on equivalent strain approach. *Metals*, 13, 2023, 3, 629.  
Available from: <https://doi.org/10.3390/met13030629>
74. MAHBADI, H. AND ESLAMI. Cyclic loading of thick vessels based on the Prager and Armstrong–Frederick kinematic hardening models. *International Journal of Pressure Vessels and Piping*, 83, 2006, 6, p. 409–419.  
Available from: <https://doi.org/10.1016/j.ijpvp.2006.02.031>
75. XU, L. Y.; FAN, J. S.; YANG, Y.; TAO, M. X.; and TANG, Z. Y. An improved elastoplastic constitutive model for the exquisite description of stress-strain hysteresis loops with cyclic hardening and softening effects. *Mechanics of Materials*, 150, 2020, 103590. ISSN 0167-6636.  
Available from: <https://doi.org/10.1016/j.mechmat.2020.103590>
76. WANG, C.; XU, L. Y. and FAN, J. S. Cyclic softening behavior of structural steel with strain range dependence. *Journal of Constructional Steel Research*, 181, 2021, 106658. ISSN 0143-974X.  
Available from: <https://doi.org/10.1016/j.jcsr.2021.106658>
77. MOEINI, G.; RAMAZANI, A.; MYSLICKI, S.; SUNDARARAGHAVAN, V. and KONKE, C. Low Cycle Fatigue Behaviour of DP Steels: Micromechanical Modelling vs. Validation. *Metals*, 7, 2017, 265.  
Available from: <https://doi.org/10.3390/met7070265>
78. WANG, H.; XIN, F.; LIU, G.; XIE, Y.; TIAN, X.; LENG, D. and MU, W. An Approach to Predicting Fatigue Crack Growth Under Mixed-Mode Loading Based on Improved Gaussian Process. *IEEE Access*, 9, 2021, p. 1–11.  
Available from: <https://doi.org/10.1109/ACCESS.2021.3050132>

79. MEGGIOLARO, M. A. and CASTRO, J. T. P. Statistical evaluation of strain-life fatigue crack initiation predictions. *International Journal of Fatigue*, 26, 2004, 5, p. 463- 476.  
Available from: <https://doi.org/10.1016/j.ijfatigue.2003.10.003>
80. GARDNER, L. and NETHERCOT, D. A. Stainless steel structural design: A new approach. *The Structural Engineer*, 82, 2004, 21, p. 21-28.  
Available from: <https://www.istructe.org/journal/volumes>
81. DAS, B. and SINGH, A. Understanding strain controlled low cycle fatigue response of P91 steel through experiment and cyclic plasticity modeling. *Fusion Engineering and Design*, 138, 2018, p. 125–137.  
Available from: <https://doi.org/10.1016/j.fusengdes.2018.11.007>
82. HYDE, C. ; SUN, W. ; HYDE, T. and SAAD, A. Thermo-mechanical fatigue testing and simulation using a viscoplasticity model for a P91 steel. *Computational Materials Science*, 56, 2012, p. 29–33.  
Available from: <https://doi.org/10.1016/j.commatsci.2012.01.006>
83. TANNER, D. ; SUN, W. and HYDE, T. FE analysis of a notched bar under thermomechanical fatigue using a unified viscoplasticity model. *Procedia Engineering*, 10, 2011, p. 1081–1086.  
Available from: <https://doi.org/10.1016/j.proeng.2011.04.178>
84. SAAD, A.; SUN, W.; HYDE, T. and TANNER, D. Cyclic softening behaviour of a P91 steel under low cycle fatigue at high temperature. *Procedia Engineering*, 10, 2011, p. 1103–1108.  
Available from: <https://doi.org/10.1016/j.proeng.2011.04.182>
85. SHAMSAEI, N. and MCKELVEY S.A. Multiaxial life predictions in absence of any fatigue properties. *International Journal of Fatigue*, 67, 2014, p. 62–72.  
Available from: <https://doi.org/10.1016/j.ijfatigue.2014.04.009>
86. DUTTA, A. ; DHAR, S. and ACHARYYA, S. K. Material characterization of SS 316 in low-cycle fatigue loading. *Journal of Materials Science*, 45, 2010, p. 1782–1789.  
Available from: <https://doi.org/10.1007/s10853-009-4155-7>
87. JANULIONIS, R. and DUNDULIS, G. Numerical simulation of low-cycle fatigue test of welded 9Cr-1Mo steel at 550 °C. *Engineering Structures*, 326, 2025, 119540. ISSN 0141-0296.  
Available from: <https://doi.org/10.1016/j.engstruct.2024.119540>
88. INTERNATIONAL ORGANIZATION FOR STANDARDIZATION (ISO). ISO 12106:2017, *Metallic materials — Fatigue testing — Axial-strain-controlled method*.
89. INTERNATIONAL ORGANIZATION FOR STANDARDIZATION (ISO). ISO 7500-1, *Metallic materials – Verification of static uniaxial testing machines – Part 1: Tension/compression testing machines – Verification and calibration of the force-measuring system*.
90. INTERNATIONAL ORGANIZATION FOR STANDARDIZATION (ISO). ISO 9513:2012, *Metallic materials – Calibration of extensometer systems used in uniaxial testing*.
91. INTERNATIONAL ORGANIZATION FOR STANDARDIZATION (ISO). ISO 23788:2013, *Metallic materials – Verification of the alignment of fatigue testing machines*.
92. INTERNATIONAL ORGANIZATION FOR STANDARDIZATION (ISO). ISO 1099:2017, *Metallic materials – Fatigue testing – Axial force-controlled method*.
93. INTERNATIONAL ORGANIZATION FOR STANDARDIZATION (ISO). ISO 4965-1:2012, *Metallic materials – Dynamic force calibration for uniaxial fatigue testing – Part 1: Testing systems*.

94. AMERICAN SOCIETY FOR TESTING AND MATERIALS (ASTM). ASTM E606/E606M-21, *Standard Test Method for Strain-Controlled Fatigue Testing*.
95. AMERICAN SOCIETY FOR TESTING AND MATERIALS (ASTM). ASTM E 1012-12, *Standard Practice for Verification of Specimen Alignment Under Tensile Loading*.
96. ASSOCIATION FRANCAISE DE NORMALISATION (AFNOR). AFNOR A 03-403:1990, *Metal products – Low-cycle fatigue test [In French]*.
97. BRITISH STANDARD (BS). BS 7270:2006, *Method for constant amplitude strain-controlled fatigue testing*.
98. JAPANESE INDUSTRIAL STANDARDS (JIS). JIS Z 2279:1992, *Method of high temperature low cycle fatigue testing for metallic materials [In Japanese]*.
99. ISO 11782-1:1998(E), *Corrosion of metals and alloys: Corrosion fatigue testing — Part 1: Cycles to failure testing*.  
Available from: <https://www.iso.org/standard/1865.htm>
100. EUROPEAN COMMITTEE FOR STANDARDIZATION (CEN). EN 10002-1:2001, *Metallic materials – Tensile testing – Part 1: Method of test at ambient temperature*.  
Available from: <https://doi.org/10.3403/01393667>
101. EUROPEAN COMMITTEE FOR STANDARDIZATION (CEN). EN 10002-5:2001, *Metallic materials – Tensile testing – Part 5: Method of testing at elevated temperature*.  
Available from: <https://doi.org/10.3403/01445072>
102. PELEGATTI, M. ; LANZUTTI, A. ; SALVATI, E. ; NOVAK, J. S. ; DE BONA, F. and BENASCIUTTI, D. Cyclic plasticity and low cycle fatigue of an AISI 316L stainless steel: Experimental evaluation of material parameters for durability design. *Materials*, 14, 2021, 13, 3588.  
Available from: <https://doi.org/10.3390/ma14133588>
103. ALHAZAA, A. and HANEKLAUS, N. Diffusion bonding and Transient Liquid phase (TLP) bonding of Type 304 and 316 Austenitic Stainless Steel – A review of similar and dissimilar material joints. *Metals*, 10, 2020, 5, 613.  
Available from: <https://doi.org/10.3390/met10050613>
104. AMERICAN SOCIETY FOR TESTING AND MATERIALS (ASTM). ASTM E1012, *Standard Practice for Verification of Testing Frame and Specimen Alignment Under Tensile and Compressive Axial Force Application*.
105. NOVAK, J. S. ; DE BONA, F. and BENASCIUTTI, D. Benchmarks for Accelerated Cyclic Plasticity Models with Finite Elements. *Metals*, 10, 2020, 6, 781.  
Available from: <https://doi.org/10.3390/met10060781>
106. DUNNE, F. and PETRINIC, N. Introduction to computational plasticity. *Oxford University Press*, 2005.  
Available from: <http://site.ebrary.com/id/10271453>
107. LEMAITRE, J. and CHABOCHE, J.L. *Mechanics of Solid Materials*. Cambridge University Press, 1990. ISBN 9780521328531.  
Available from: <https://doi.org/10.1017/CBO9781139167970>
108. CHABOCHE, J.L. A review of some plasticity and viscoplasticity constitutive theories. *International Journal of Plasticity*, 24, 2008, 10, p. 1642–1693.  
Available from: <https://doi.org/10.1016/j.ijplas.2008.03.009>
109. CHEN, W.F. and ZHANG, H. *Plasticity for Structural Engineers*. Springer-Verlag, 1988. ISBN 978-1-4612-3864-5.  
Available from: <https://doi.org/10.1007/978-1-4612-3864-5>
110. SIMO, J.C. and HUGHES, T.J.R. *Computational Inelasticity*. Springer, 1998.  
Available from: <https://doi.org/10.1007/b98904>

111. THYSSENKRUPP MATERIALS (UK), LTD. *Stainless Steel 304L (1.4307) Data Sheet* [dataset]. Retrieved September 2025.  
Available from: <https://www.thyssenkrupp-materials.co.uk/stainless-steel-304l>
112. AZOM. *Stainless Steel – Grade 316L – Properties, Fabrication and Applications* [dataset]. 2001.  
Available from: <https://www.azom.com/article.aspx?ArticleID=2382>
113. MAKEITFROM. *AISI 304L (S30403) Stainless Steel vs. AISI 316L (S31603) Stainless Steel* [dataset]. Retrieved September 2025, MakeItFrom.com, n.d.  
Available from: <https://www.makeitfrom.com/compare/AISI-304L-S30403>
114. EFUNDA. *AISI Type 316L: Material Properties* [dataset]. Retrieved September 2025, eFunda, n.d.  
Available from: [https://www.efunda.com/materials/alloys/stainless\\_steels](https://www.efunda.com/materials/alloys/stainless_steels)
115. MACSTEEL. *304/304L Stainless Steel Datasheet* [dataset]. 2021, Macsteel.  
Available from: <https://macsteel.co.za/wp-content/uploads/2022/12/304-304L>
116. BAGLION, L. and MENDEZ, J. Low cycle fatigue behavior of a type 304L austenitic stainless steel in air or in vacuum, at 20 °C or at 300 °C: Relative effect of strain rate and environment. *Procedia engineering*, 2, 2010, 1, p. 2171-2179.  
Available from: <https://doi.org/10.1016/j.proeng.2010.03.233>
117. SPACEMATDB. *AISI 316L Stainless Steel Material Properties* [dataset]. Retrieved September 2025, SpaceMatDB, n.d.  
Available from: <https://www.spacematdb.com>
118. WORLD AUTO STEEL AND WORLD STEEL ASSOCIATION. *Yield Strength – AHSS Guidelines* [dataset]. 2024, AHSS Insights.  
Available from: <https://ahssinsights.org/forming/mechanical-properties>
119. SHIT, J., DHAR, S.; ACHARYYA, S. and GOYAL, S. Modeling of uniaxial ratchetting behavior of SA333 carbon manganese steel. *International Journal of Pressure Vessels and Piping*, 92, 2011, p. 96–105.  
Available from: <https://doi.org/10.1016/j.ijpvp.2011.11.007>
120. JIANG, Y. and KURATH, P. Characteristics of the Armstrong-Frederick type plasticity models. *Integatesrational Journal of Plasticity*, 12, 1996, 3, p. 387-415.  
Available from: [https://doi.org/10.1016/S0749-6419\(96\)00013-7](https://doi.org/10.1016/S0749-6419(96)00013-7)
121. CHABOCHE, J. L. Time-independent constitutive theories for cyclic plasticity. *International Journal of Plasticity*, 2, 1986, 2, p. 149–188.  
Available from: [https://doi.org/10.1016/0749-6419\(86\)90010-0](https://doi.org/10.1016/0749-6419(86)90010-0)
122. CHABOCHE, J. L. On Some Modifications of Kinematic Hardening to Improve the Description of Ratchetting Effects. *International Journal of Plasticity*, 7, 1991, 7, p. 661–678.  
Available from: [https://doi.org/10.1016/0749-6419\(91\)90050-9](https://doi.org/10.1016/0749-6419(91)90050-9)
123. CHABOCHE, J.L. and ROUSSELIER, G. On the Plasticity and viscoplasticity Constitutive Equations – Part II: Application of Internal Variable Concepts to the 316 Stainless Steel. *Journal of Pressure Vessel Technology*, 105, 1983, p. 159-164.  
Available from: <https://doi.org/10.1115/1.3250023>
124. CHABOCHE, J.L. and ROUSSELIER, G. On the Plastic and Viscoplastic Constitutive Equations – Part I: Rules Developed with Internal Variable Concept. *Journal of Pressure Vessel Technology*, 105, 1983, p: 153–158.  
Available from: <https://doi.org/10.1115/1.3250022>
125. CHABOCHE, J.L.; DANG-VAN, K. and CORDIER, G. Modelization of the strain memory effect on the cyclic hardening of 316 stainless steel. In: *Proceedings of the 5th International Conference on SMiRT*, Berlin, Germany, 1979.

126. PRAGER, W. On the theory of flow and rupture of ductile solids. *Journal of Applied Physics*, 20, 1949, 3, p. 235–241.
127. JIANG, Y. Cyclic plasticity with an emphasis on ratchetting. PhD thesis, *University of Illinois at Urbana-Champaign*, 1994. eLibrary ID: 5732150.  
Available from: <https://www.ideals.illinois.edu/items/5732150>
128. CHABOCHE, J.L. Modeling of ratchetting: Evaluation of various approaches. *European Journal of Mechanics A/Solids*, 13, 1994, 4, p. 501–518.  
Available from: [https://doi.org/10.1016/0997-7538\(94\)90033-3](https://doi.org/10.1016/0997-7538(94)90033-3)
129. JUANG, Y. and SEHITOGLU, H. Comments on the Mroz multiple surface type plasticity models. *International Journal of Solids and Structures*, 33, 1996, 7, p. 1053–1068.  
Available from: [https://doi.org/10.1016/0020-7683\(95\)00193-9](https://doi.org/10.1016/0020-7683(95)00193-9)
130. ARMSTRONG, P.J., and FREDERICK, C.O. A Mathematical Representation of the Multiaxial Bauschinger Effect. CEB Report No: RD/B/N 731, *Central Electricity Generating Board*, 1996.
131. BARI, S. and HASSAN, T. Anatomy of coupled constitutive models for ratcheting simulation. *International Journal of Plasticity*, 16, 2000, p. 381–409.  
Available from: [https://doi.org/10.1016/S0749-6419\(99\)00059-5](https://doi.org/10.1016/S0749-6419(99)00059-5)
132. REZAIIEE-PAJAND, M. and SINAIE, S. On the calibration of the Chaboche hardening model and a modified hardening rule for uniaxial ratcheting prediction. *International Journal of Solids and Structures*, 46, 2009, 16, p. 3009–3017.  
Available from: <https://doi.org/10.1016/j.ijsolstr.2009.04.002>
133. TONG, J. and VERMEULEN, B. The description of cyclic plasticity and viscoplasticity of waspaloy using unified constitutive equations. *International Journal of Fatigue*, 25, 2003), 5, p. 413–420.  
Available from: [https://doi.org/10.1016/s0142-1123\(02\)00162-7](https://doi.org/10.1016/s0142-1123(02)00162-7)
134. TONG, J.; ZHAN, Z. and VERMEULEN, B. Modelling of cyclic plasticity and viscoplasticity of a nickel-based alloy using Chaboche constitutive equations. *International Journal of Fatigue*, 26, 2004, 8, p. 829–837.  
Available from: <https://doi.org/10.1016/j.ijfatigue.2004.01.002>
135. ZHAN, Z. and TONG, J. A study of cyclic plasticity and viscoplasticity in a new nickel-based superalloy using unified constitutive equations. Part II: Simulation of cyclic stress relaxation. *Mechanics of Materials*, 39, 2006, 1, p. 73–80.  
Available from: <https://doi.org/10.1016/j.mechmat.2006.01.006>
136. MOSLEMI, N.; ZARDIAN, M. G.; AYOB, A.; REDZUAN, N. and RHEE, S. Evaluation of sensitivity and calibration of the Chaboche Kinematic Hardening model parameters for numerical ratcheting simulation. *Applied Sciences*, 9, 2019, 12, 2578.  
Available from: <https://doi.org/10.3390/app9122578>
137. KOO, G. and KWON, J. Identification of inelastic material parameters for modified 9Cr–1Mo steel applicable to the plastic and viscoplastic constitutive equations. *International Journal of Pressure Vessels and Piping*, 88, 2010, 1, p. 26–33.  
Available from: <https://doi.org/10.1016/j.ijpvp.2010.11.004>
138. RAHMAN, S. M.; HASSAN, T. and CORONA, E. Evaluation of cyclic plasticity models in ratcheting simulation of straight pipes under cyclic bending and steady internal pressure. *International Journal of Plasticity*, 24, 2008, 10, p. 1756–1791.  
Available from: <https://doi.org/10.1016/j.ijplas.2008.02.010>
139. KACAR, I. Parameters Calibration of the Combined Hardening Rule through Inverse Analysis for Nylock Nut Folding Simulation. *Computer Modeling in Engineering and Sciences*, 128, 2021,1, p. 87–108.

- Available from: <https://doi.org/10.32604/cmcs.2021.015227>
140. MAHMOUDI, A.; PEZESHKI-NAJAFABADI, S. and BADNAVA, H. Parameter determination of Chaboche kinematic hardening model using a multi objective Genetic Algorithm. *Computational Materials Science*, 50, 2010, 3, p. 1114–1122.  
Available from: <https://doi.org/10.1016/j.commatsci.2010.11.010>
141. ZHANG, S. ; KORKOLIS, Y. P. ; RIFFEL, K. C. and RAMIREZ, A. J. Optimizing the combined Isotropic/Kinematic hardening parameters of pressure vessel materials and welds using the incremental Elastic-Limit approach. *International Journal of Pressure Vessels and Piping*, 124, 2024, 105407.  
Available from: <https://doi.org/10.1016/j.ijpvp.2024.105407>
142. ZHANG, X.; WANG, T.; GONG, X.; LI, Q.; LIU, Y.; WANG, Q.; ZHANG, H. and WANG, Q. Low cycle fatigue properties, damage mechanism, life prediction and microstructure of MarBN steel: Influence of temperature. *International Journal of Fatigue*, 144, 2020, 106070.  
Available from: <https://doi.org/10.1016/j.ijfatigue.2020.106070>
143. PATE, S. B. ; DUNDULIS, G. ; COURTIN, S. and LE ROUX, J-C. The effects of strain amplitude and temperature on kinematic hardening parameters for low cycle fatigue of AISI316L stainless steel. *Nuclear Engineering and Design*, 442, 2025, 114221.  
Available from: <https://doi.org/10.1016/j.nucengdes.2025.114221>

## **CURRICULUM VITAE AND DESCRIPTION OF CREATIVE ACTIVITIES (CV)**

**Sushant Bhalchandra Pate**

sushant.pate@ktu.lt

### **Education:**

[01/09/2021- present]: PhD. Mechanical Engineering.  
[Kaunas University of Technology, Kaunas, Lithuania]

[01/09/2019–30/06/2021]: M.Sc. Mechanical Engineering.  
[Kaunas University of Technology, Kaunas, Lithuania]

[08/08/2014 – 01/07/2018]: B.E. Mechanical Engineering.  
[SLRTCE, Mumbai University, Mumbai, India]

### **Professional experience:**

[01/07/2024 – present]: Mechanical Tool Shop Engineer.  
[Continental Autonomous Mobility, Kaunas, Lithuania]

[18/07/2022 – 30/06/2024]: Mechanical Tool Shop Engineer Intern.  
[Continental Autonomous Mobility, Kaunas, Lithuania]

[01/02/2021 – 30/04/2021]: Trainee. (Involved in project, ‘Numerical modelling of stress flow inside the complex textile structures and products.’)  
[Lodz University of Technology, Lodz, Poland]

[22/10/2018 – 20/08/2019]: Design Engineer.  
[Pollucon Enviro Engineers PVT. LTD., Mumbai]

[18/06/2018 – 21/10/2018]: Intern. Design Engineer.  
[Accurate Laser Tech, Mumbai]

[01/06/2017–30/07/2017]: Intern. In Designing Department.  
[Pollucon Enviro Engineers PVT. LTD., Mumbai]

### **Areas of research interest:**

Finite element modelling of material behaviour, investigation of low cycle fatigue behaviour, failure mechanics, fracture failure.

**Scientific papers other than topic of dissertation:**

1. PATE, S. B.; SOLOMON, I. S. M.; DUNDULIS, G. and GRISKEVICIUS, P. Applications of the FEM to pipe whip analysis using coupled modelling technique. *Nuclear Engineering and Design*, 418, 2024, p. 1–7.  
Available from: <https://doi.org/10.1016/j.nucengdes.2024.112941>
2. PATE, S. B. and KORYCKI, R. Numerical optimization of stress concentration in composite structures for different material arrangement. *Materials*, 14, 2021, 11, p. 1–14.  
Available from: <https://doi.org/10.3390/ma14112957>

## LIST OF SCIENTIFIC PAPERS AND SCIENTIFIC CONFERENCES

### ARTICLES IN PEER-REVIEWED SCIENTIFIC PUBLICATIONS

#### Indexed in the Web of Science with Impact Factor International (foreign) publishers

1. PATE, S. B.; DUNDULIS, G.; KILIKVIČIUS, S. and GRYBENAS, A. Experimental and numerical examination of low cycle fatigue behaviour on AISI 304L steel. *Nuclear Engineering and Design*, 2024, 429, 113599, p. 1–9. ISSN 0029-5493.  
Available from: <https://doi.org/10.1016/j.nucengdes.2024.113599>
2. PATE, S. B.; DUNDULIS, G. and GRISKEVIČIUS, P. Modeling of LCF behaviour on AISI 316L steel applying the Armstrong–Frederick kinematic hardening model. *Material*, 17, 2024, 14, 3395, p. 1–11. ISSN 1996-1944.  
Available from: <https://doi.org/10.3390/ma17143395>
3. PATE, S. B.; DUNDULIS, G.; COURTIN, S. and LE ROUX, J-C. The effects of strain amplitude and temperature on kinematic hardening parameters for low cycle fatigue of AISI 316L stainless steel. *Nuclear Engineering and Design*, 442, 2025, 114221. ISSN 0029-5493.  
Available from: <https://doi.org/10.1016/j.nucengdes.2025.114221>

## **Indexed in other Web of Science or Scopus publications**

### **International (foreign) publishers**

1. PATE, S. B.; DUNDULIS, G. and GRYBENAS, A. Application of finite element method for low cycle fatigue analysis for steel. In: *METAL 2023: 32nd International Conference on Metallurgy and Materials*. Brno, Czech Republic, 17–19 May 2023. Ostrava-Zábřeh: TANGER Ltd., 2023, pp. 289–295. Available from: <https://doi.org/10.37904/metal.2023.4647>

### **National (Lithuanian) publishers**

1. PATE, S. B.; DUNDULIS, G. and GRYBENAS, A. Numerical modelling of the low cycle fatigue in austenitic stainless steel. In: *MECHANIKA 2023: Proceedings of the 27th International Scientific Conference*. Kaunas, Lithuania, 26 May 2023. Kaunas: Kaunas University of Technology, 2023, pp. 279–283.

### **PRESENTATION OF RESEARCH RESULTS AT CONFERENCES Other conference abstracts and non-peer reviewed conference papers.**

- 1) PATE, S. B. and DUNDULIS, G. Investigation on the effects of the strain amplitude and operating temperature on the hardening parameters of AISI316L stainless steel. *43rd Solid Mechanics Conference: SolMech 2024, 16-18 September 2024*, Wroclaw, Poland.

## ACKNOWLEDGEMENT

The author would like to express his sincere gratitude to the INCEFA-SCALE and INCEFA-PLUS projects for their valuable support throughout the course of this work. Special thanks are extended to EDF (Électricité de France), LEI (Lithuanian Energy Institute), and KTU (Kaunas University of Technology) for their collaboration and for providing the experimental data that formed the foundation of this study. Their contributions have been instrumental in enabling the successful completion of the experimental investigation.

UDK: 669.15-194.56+620.178.3+539.37](043.3)

SL344. 2026-02-18, 18,5 leidyb. apsk. I. Tiražas 14 egz. Užsakymas 0033.  
Išleido Kauno technologijos universitetas, K. Donelaičio g. 73, 44249 Kaunas  
Spausdino leidyklos „Technologija“ spaustuvė, Studentų g. 54, 51424 Kaunas

